Supplemental Material for “A Time-Average Ocean: Thermal Wind and Flow Spirals”

Carl Wunsch*
Department of Earth and Planetary Sciences
Harvard University
Cambridge MA 02138
email: cwunsch@gmail.com

September 16, 2023

1 Other Averages

A large number of pictorial representations of a 20-year average from an earlier release (r4v3) are attahced below. These include properties additional to those shown here in the main text including e.g., surface elevation. . For fields common to both releases results are, visually, very similar to those displayed in the main text.

2 Flow Fields

What follows are the enlarged versions of the flow fields shown in Figs.1,2 of the main text.

3 Rossby Number

Vertical Density Derivatives

The vertical density derivative (positive downward) is shown for the mid-Pacific Ocean along 180°W. As with the figures in the main text, no obvious pycnocline depth describes the entire latitude range.

*Also, Dept. of Earth, Atmospheric and Planetary Sciences, MIT

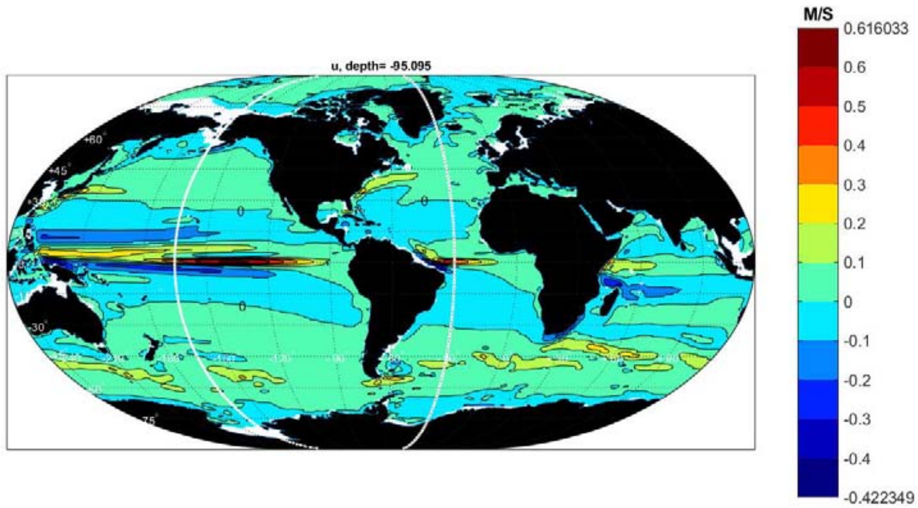

Figure 1: Twenty-six year time-averaged zonal flow, u, at 95m in the state estimate. A major feature is the strong zonality in the equatorial regions including an equatorial undercurrent in the Atlantic and Pacific Oceans and weakly in the Indian Ocean. White arcs are the position of meridional sections at 165°W and 30°W sometimes used below.

{zonalflow_95m

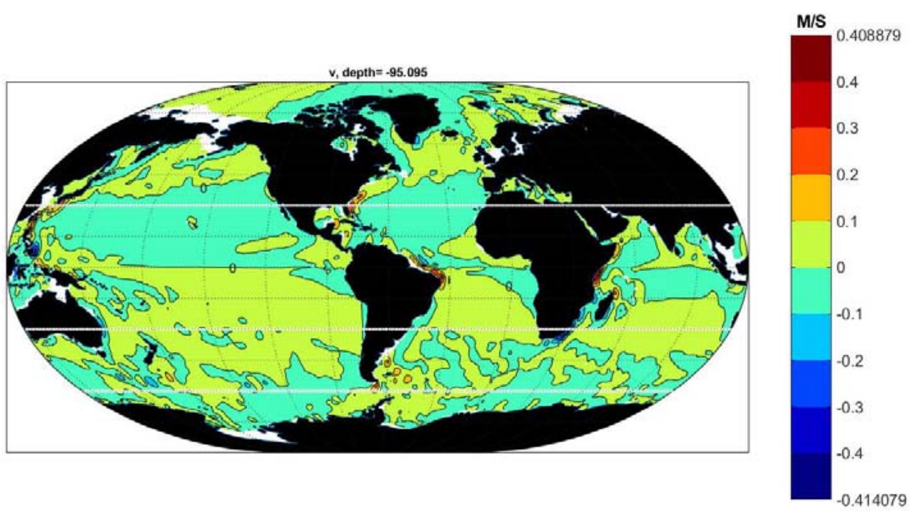

Figure 2: Same as Fig. 1, but for the meridional component of flow, v at 95m. The subtropical gyres and the western boundary currents are major features. Relative weakness of v compared to u in the Southern Ocean is visible. Three of the latitude bands, 60°S, 30°S, 30°N, used below are indicated as dotted white lines.

{meridflow_95m

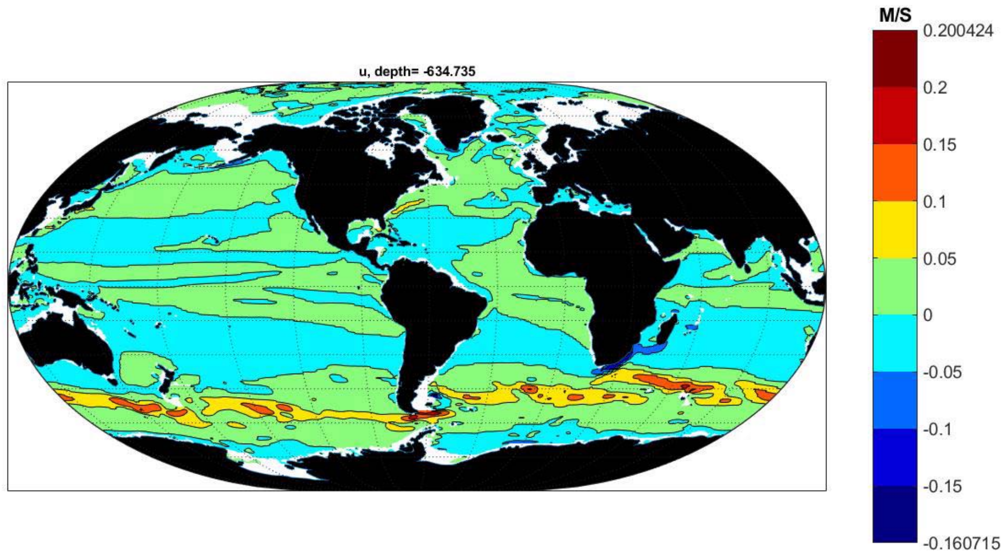

Figure 3: Zonal flow at 635m. Light green areas correspond to positive (eastward) u, and light blue to negative (westward) flow. Complex high wavenumber structures in the Southern Ocean are likely induced by the topographic structures and a tendency to barotropic (near-constant in z) flow in the vertical. {zonalflow_635

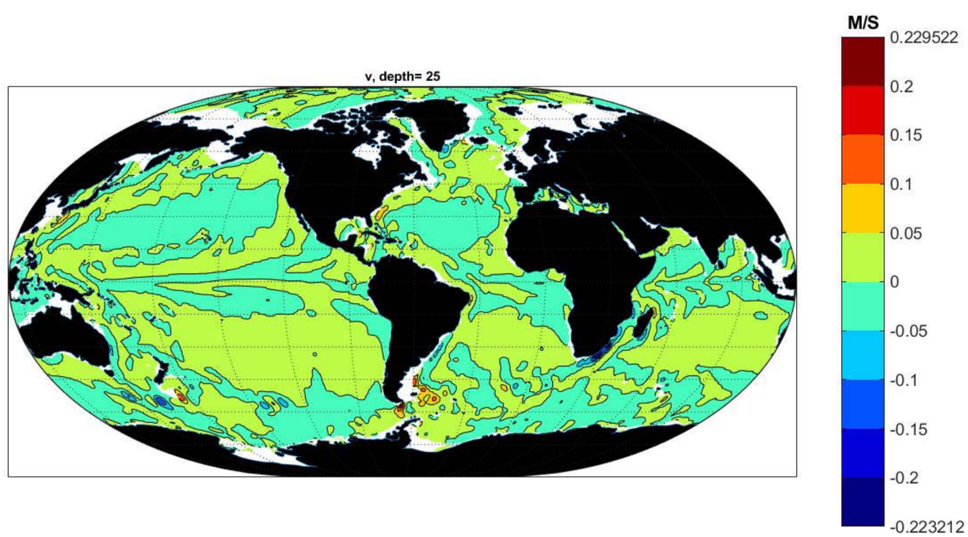

Figure 4: Meridional flow, v, at 635 m. Note the enhanced value in the Argentine Basin, and discussed briefly in the Appendix. {meridflow_635

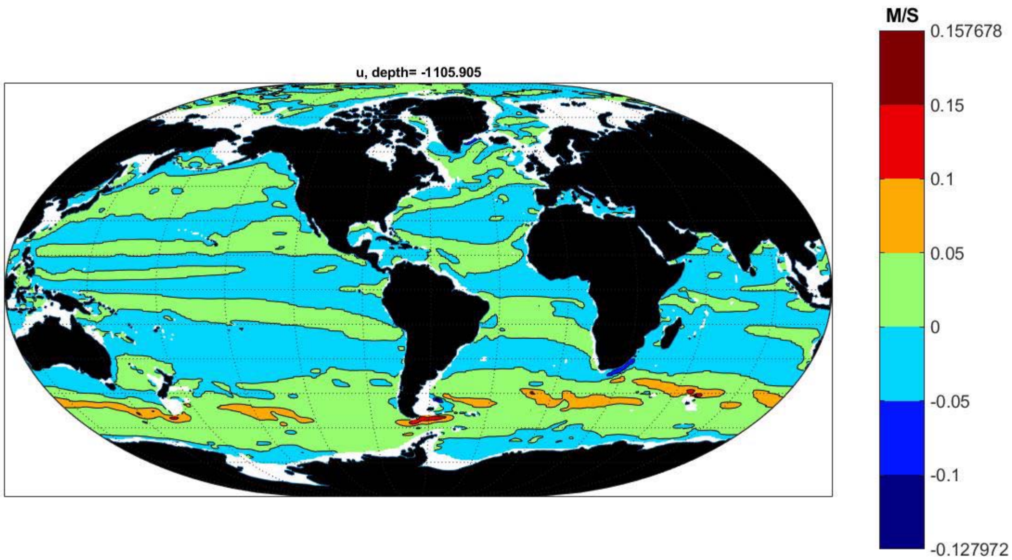

Figure 5: Zonal mean flow at 1100m, with a now-pronounced zonality and the appearance of maxima in the Southern Ocean. Compare e.g., to Hogg and Owens (1999). {zonalflow_110

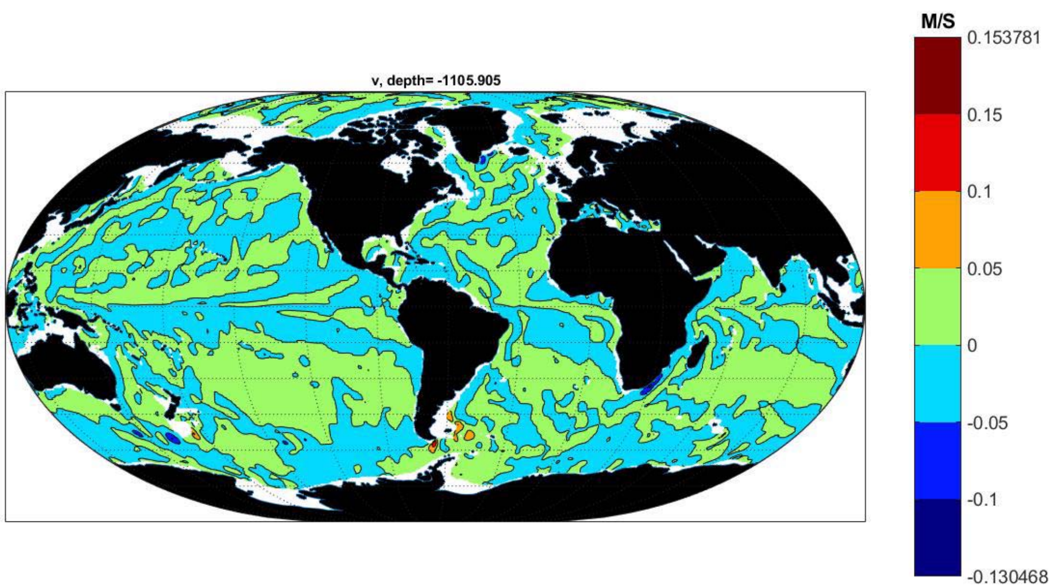

Figure 6: Meridional mean flow, v, at 1100m and showing far-more complex spatial structure as compared to the zonal component and which, through Eq. (**??**) implies a noisy vertical velocity (see Liang et al., 2017 or Fig. 3 of W23). {meridflow_110

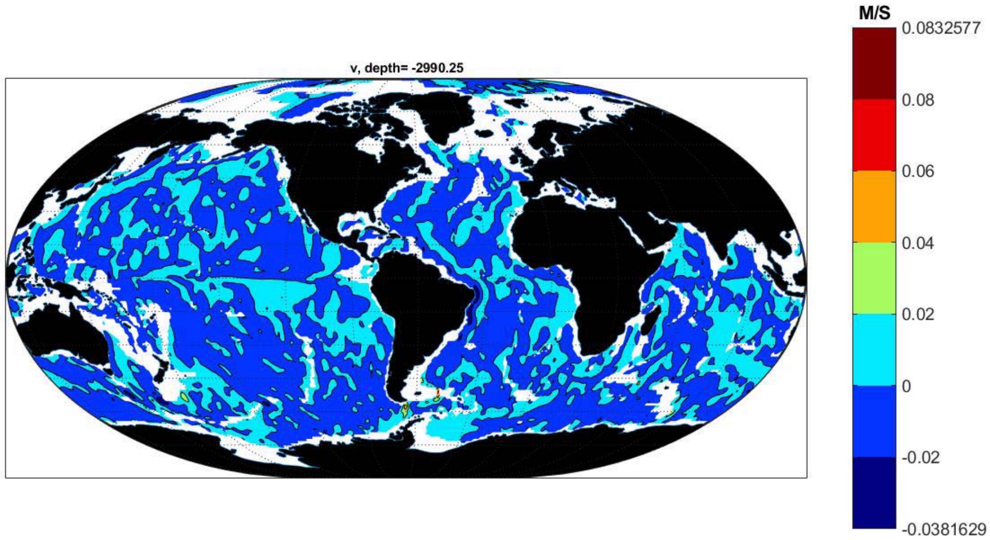

Figure 7: Meridional flow v at 3000m. {meridflow_300

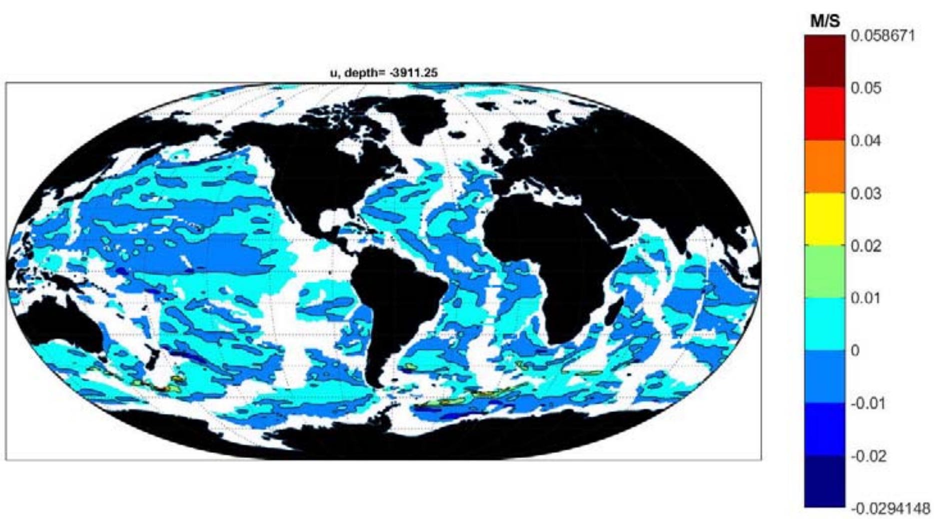

Figure 8: Zonal flow at 3900m. {zonaflow_3900

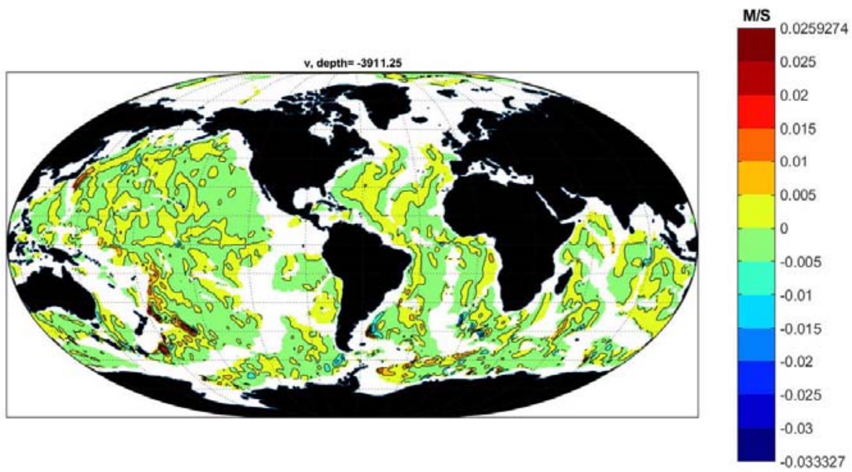

Figure 9: Meridional flow (m/s) at 3900m. Equatorial discontinuity is generally present. Open-ocean topography effects are now visible.

{meridflow_390

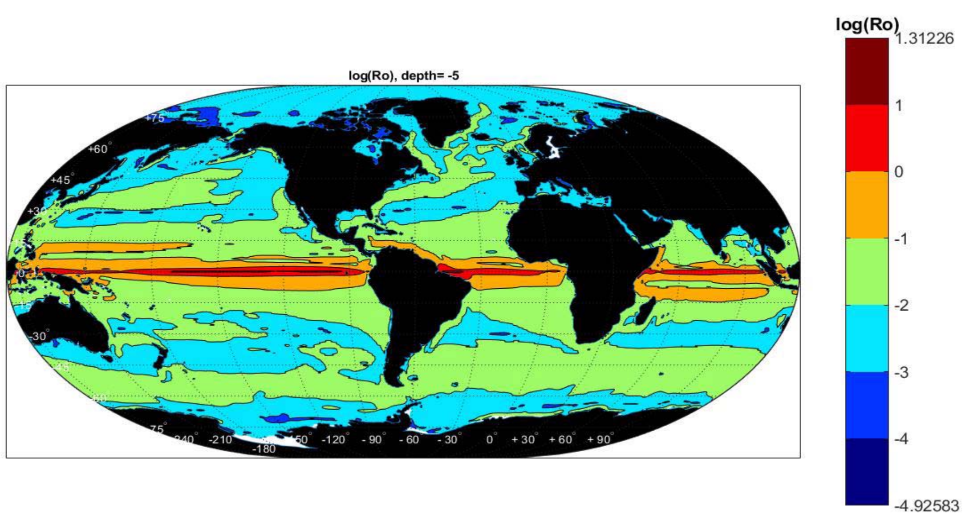

Figure 10: Log_{10} of the Rossby number, Ro, for the time-averaged flow speed at 5m based upon a 55km length scale in the ECCOv4r4 time-average. Gyre structures are apparent from their centers being marked by very small values, $Ro < 10^{-2}$.

{A4}

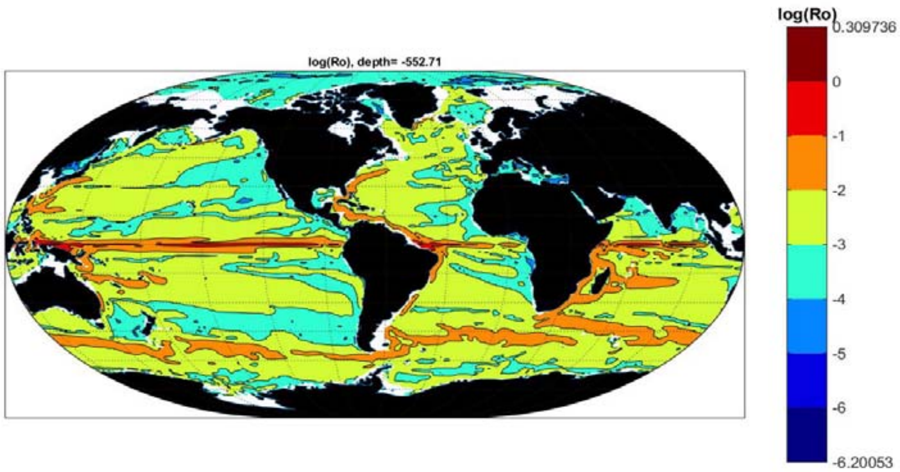

Figure 11: Base 10 logarithm of the Rossby number at 550m based upon a 55km length scale. A tendency to zonality can be seen, particularly in the Pacific Ocean. Southern Ocean now appears to have relatively large Rossby numbers.

{rossbynumber_

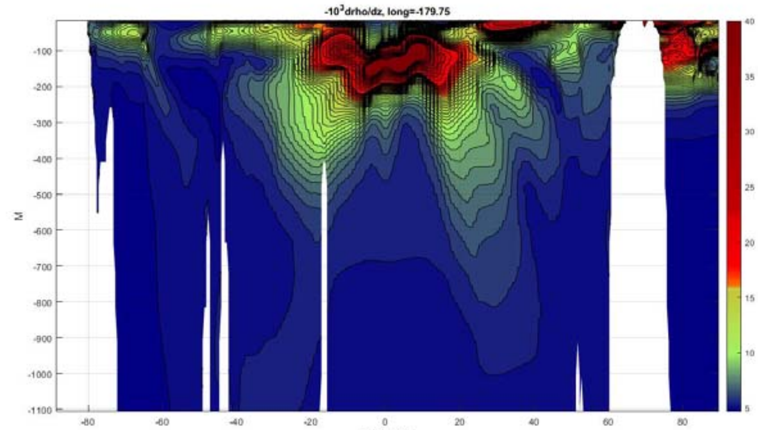

Figure 12: 10^3 times the vertical density derivative at 180°W. As with the charts in the main text, no simple depth definition of the thermocline is apparent.

4 Earlier Release Average

The two papers that follow from release 3 of version 4 can also be obtained directly from http://hdl.handle.net/1721.1/107613 and http://hdl.handle.net/1721.1/109847. A published discussion is by Fukumori, I. Heimbach, P.Ponte, R. M.Wunsch, C. 2018: A dynamically-consistent ocean climatology and its temporal variations. Bulletin Amer. Met. Soc., October, 2107-2127. A much wider description of the circulation and its variability can be found there.

5 References

ECCO Consortium, 2017a (ECCO2017a): A Twenty-Year Dynamical Oceanic Climatology: 1994-2013. Part 1: Active Scalar Fields: Temperature, Salinity, Dynamic Topography, Mixed-Layer Depth, Bottom Pressure. http://hdl.handle.net/1721.1/107613

———, 2017b (ECCO2017b): A Twenty-Year Dynamical Oceanic Climatology: 1994-2013. Part 2: Velocities and Property Transports. http://hdl.handle.net/1721.1/109847.

A Twenty-Year Dynamical Oceanic Climatology: 1994-2013. Part 1: Active Scalar Fields: Temperature, Salinity, Dynamic Topography, Mixed-Layer Depth, Bottom Pressure

The ECCO Consortium (M, Buckley[8], J.-M. Campin[3],A. Chaudhuri[1], I. Fenty[2], G. Forget[3],I. Fukumori[2], P. Heimbach[3,4], C. Hill[3], C.King[3], X. Liang[5], A. Nguyen[4] C. Piecuch[1], R. Ponte[1], K. Quinn[1], M. Sonnewald[3], D. Spiegel[3], N. Vinogradova[7], O. Wang[2], C. Wunsch[3,6])[†]

March 3, 2017

Abstract

The World Ocean Circulation Experiment (WOCE) was created to produce the first climatologically useful picture of the ocean circulation and its low-frequency variability. This goal is addressed here from the state estimate of the Estimating the Circulation and Climate of the Ocean (ECCO) consortium, which uses almost all of the data obtained during WOCE and its aftermath along with the much improved general circulation modeling capabilities. A dynamically and data-consistent, time-evolving, state estimate is available depicting the ocean and its ice-cover over a 23-year time-span, globally, from the sea surface to the sea floor. The resulting time-dependent 20-year long climatology includes temperature, salinity, surface elevation, bottom pressure, sea-ice, and three components of velocity. Accompanying the state estimate are modified estimates of meteorological forcing-fields, ocean interior mixing coefficients, and initial conditions. Much spatial structure persists through the two-decade averaging. Results here are primarily pictorial in nature, intended to give the wider community a sense of what is now available and useful and where more detailed analysis would be fruitful. An extended reference list is included.

[*]For corrections, additions, comments and criticisms please email carl.wunsch@gmail.com.

[†]1. AER, Inc., 2. Jet Propulsion Laboratory, 3. MIT, 4. U. Texas Austin, 5. U. South Florida, 6. Harvard U., 7. Cambridge Climate Institute, 8. George Mason U.

1 Introduction: The State Estimate

Purpose

One of the central goals of the World Ocean Circulation Experiment (WOCE) was to produce the first truly global time-varying estimate of the circulation over approximately a decade, an estimate that would be useful in defining the major climatologically important ocean elements. The Estimating the Circulation and Climate of the Ocean (ECCO) project was formed near the start of the WOCE field program so as to address this goal using both the conventional and newly-deploying WOCE observation system, along with the rapidly advancing general circulation modelling capability (Stammer et al., 2002). In this paper, and in subsequent Parts, this WOCE goal is addressed by defining a time-dependent climatology over the 20-year (bidecadal) interval 1994-2013. Little or no dynamical or kinematical interpretation is provided—that is left to other authors and times.

Various oceanic climatologies are in use by the oceanographic and climate dynamics communities. They serve as tests of models, as initial conditions, and as a basic descriptor of the ocean. Definitions of climatologies vary widely both in terms of how they were formed and the durations they represent. Here we describe a 20-year average modern climatology from a dynamically consistent model that also has a consistent fit to the majority of global data between 1992 and 2015 (Wunsch and Heimbach, 2013). The climatology is based upon the ECCO version 4 state estimate (Forget et al., 2015). It derives from a least-squares fit of the MITgcm (Marshall et all, 1997; Adcroft et al., 2004; Forget et al., 2015) to the numerous and diverse global observations. A summary would be that all of the Argo, altimetry, the CTD hydrography appearing in the WOCE Climatology and successors (Gouretski and Koltermann, 2004; Talley et al., 2016), all extant, bias error-corrected XBTs, the considerable elephant seal profile data (Roquet et al., 2013), GRACE mission mean and time-dependent geoids, satellite-measured sea surface temperature and salinity, and the ECMWF[1] ERA-interim reanalysis of the meteorological variables (Dee et al., 2014), have been included, with the fits inferred to be adequate relative to the estimated uncertainties of the data. (Atmospheric reanalyses should not be considered "data", however.)

Previous climatologies, e.g. Levitus et al. (1982) and its later incarnations as the NOAA World Ocean Atlas, or Gouretski and Koltermann (2004) have usually been based only upon temperature and salinity averages and over much longer time intervals than employed here. Other climatologies (e.g., AchutaRao et al., 2007) have focussed on the upper 700 or 1000m and relied heavily on XBT measurements. As such, all these suffer from the very great inhomogeneities

[1] European Centre for Medium Range Weather Forecasts

of data distribution prior to the WOCE period and a series of untestable statistical hypotheses (see e.g., Wunsch, 2016; Boyer et al., 2016). This present climatology differs from earlier ones most obviously in its production of the three-dimensional, time-varying, three components of velocity and of a self-consistent surface meteorology, as determined at the model time-step, $\Delta t \approx 1$ h. Use of *any* fluid climatology confronts one basic problem: that the resulting time or space-time average fields do not satisfy any simply derivable equations of motion—requiring a variety of turbulence closure schemes—and the relationships among the different variables can be complicated and poorly known. Here, time/space means of fluid quantities are based upon the uniform average of fields exactly satisfying the model equations at each model time-step (nominally 1 hour) and grid-point. Some authors have used ocean general circulation models fit to data in methods analogous to those in meteorology and commonly known as "reanalyses." These, unfortunately, are usually not property conserving (heat, salt, momentum, etc.) and thus unsuitable for global-scale climate calculations (see e.g., Wunsch and Heimbach, 2013; and Fig. 1 of Stammer et al., 2016).

A number of sketches of global scale analyses of earlier multi-decadal ECCO estimates has been published starting with Stammer et al. (2002). An earlier 16-year global time-average was described by Wunsch (2011), with a focus on the accuracy of Sverdrup balance, and Wunsch and Heimbach (2014) discussed the heat content changes. Liang et al. (2016a,b) describe the vertical redistribution of heat. In general, the present solution differs only subtly from those previously used, with the chief differences being ascribed to the inclusion of more data over a longer duration, inclusion of geothermal heating, improvements in the handling of sea ice, and where appropriate separate uncertainties for time-average and time-anomaly measurements. Solutions are generally robust, as the great volume of ocean in the model state vector is in near-geostrophic balance with the density field at all times longer than a few days.

By choosing the period following 1994, a much more nearly uniform global data coverage is obtained than was possible earlier. Chief among the remaining data inhomogeneities are the intensification of the Argo float profile data availability after about 2005.

Any temporally averaged state will be considerably smoother than states which are sampled more or less as "snapshots." Thus classical hydrographic sections (e.g., Fuglister, 1960 or the various WOCE Atlases) show many small-scale features which vanish on averaging. Suppressed features include internal waves, tides, and geostrophically balanced eddy motions. Meandering currents, such as the off-shore Gulf Stream, are broader and smoother than in any near-synoptic estimate. In addition, fluid regions that are only marginally or poorly resolved numerically (particularly boundary currents), will be smoother than even a true 20-year average would be.

No model with a nominal horizontal grid-spacing of 1° of longitude can resolve small-scale circulation features, which include the important boundary currents. Nonetheless, the near-geostrophy of the bulk of the ocean supports the conjecture that to the extent that a successful fit to the interior temperature, salinity, and altimetric fields and surface boundary conditions, has been obtained, the boundary currents will be forced by the interior flows to carry the appropriate amount of mass (volume), temperature, etc. so as to satisfy the basic overall conservation laws. This conjecture, upon which we rely, can be regarded as a formal statement of that used by Stommel and Arons (1960) in their discussion of deep boundary currents—whose existence and structure was fixed by the mass and property requirements of the interior flow—even though they were not dynamically resolved.

As with any estimation problem, a crucial element in the determination of the best values lies with the use of realistic error estimates for *all* of the data that are being fit. For a full discussion of the error estimate used here, reference must be made to the literature. Temperature measurements are described by Forget and Wunsch (2007) and Abraham et al. (2013). Altimetry accuracies are discussed by Fu and Haines (2013) and Forget and Ponte (2015). For the gravity data from the GRACE mission, see Quinn and Ponte (2008). Satellite surface salinities are addressed by Vinogradova et al. (2014). Meteorological variable accuracies are described e.g., by Chaudhuri et al. (2013).

This paper is *not* an in-depth analysis of *any* features of the global ocean circulation. It is instead mainly visually descriptive—a suggestive pictorial subsample—intended primarily to serve as an invitation to the wider community to exploit it by demonstrating various products. With the widespread recognition that a steady-state ocean never exists, attention turns instead to the temporal changes over the estimation period.[2] Here for descriptive purposes, some pictures of changes year-by-year for 20 years, by 20-year averages by month, and by season are displayed. All results can readily be calculated month-by-month at the expense of using a larger volume of numbers.

Most results are intended mainly to be indicative of possibilities rather than being the most precise or accurate possible. Thus for example, the heat capacity, c_p and the mean density, $\bar{\rho}$ are treated as constant in calculations of heat uptake even though both are (weak) functions of position.

The State Estimate

The ECCO state estimate is obtained from the *freely-running* MITgcm after the adjustment of the control parameters required to fit the data. In the least-squares methodology with Lagrange multipliers (see Wunsch and Heimbach, 2013), the entire interval 1992-2015 has been

[2] Forget (2010) presented an 18-month estimate from an earlier ECCO state estimate, and which is closer to being a "snapshot" rather than a climatology.

fit to the data. Parameters adjusted include the three-dimensional, top-to-bottom, initial conditions, internal mixing coefficients, and the surface meteorology. At any given time in the estimation interval, the solution represents data both preceding and *following* that date so that the equations are always satisfied while coming as close to the data as possible within uncertainty estimates. The 20-year period 1994-2013 has been chosen for averaging as sufficiently distant from the poorly constrained earlier years before the high accuracy altimetry begins in late 1992 and the time of the then non-existent data following 2016. The period corresponds to that of complete coverage by satellite altimetry, the WOCE CTD survey, and the interval after about 2005 when the Argo array became fully-deployed. All data, plus the ECMWF estimate, have been assigned uncertainties that include both instrumental and natural noise. After adjustment of the parameters, the free-running forward model satisfies all basic conservation requirements and is structurally no different from any other unconstrained model estimate.

No state estimate is definitive or "correct"; they are "best-estimates" for the present time: data are continuously added, both from more recent years and previously omitted earlier values; estimated data errors are sometimes revised; models are improved; and in all situations, minimizing iterations are ongoing. Values shown here are obtained from ECCO version 4 as of mid-November 2016.

Undoubtedly the state estimate has residual systematic errors at some level, particularly in data-poor regions and times. To some extent, these will be removed when considering only temporal changes in the state over the 20-years and these latter are given some emphasis. Uncertainty estimates remain an amorphous problem: much of the variability in the model represents deterministically evolving elements. Stochastic elements are introduced by weather, some longer-period meteorological variability, and by elements of the initial-conditions best regarded as random. Because the true probability distributions are not known, discussion of estimate uncertainties is postponed to Part 4.

A full description of the many features of a 20-year average global ocean circulation requires a book-length publication, if not a library. The strategy here is to sketch the gross hydrographic and circulation features and to do a limited comparison to a few of the special regions (boundary currents, mixed-layer, etc.) to provide some of the flavor of the differences between an average and both the more common limited-time analyses usually available (classical synoptic hydrographic sections) as well as the far more inhomogeneous published climatologies.

With time-mean fields being spatially and temporally smoother than in nominally synoptic measurements, second order quantities such as the time averages e.g., $\langle \mathbf{v} \rangle \langle T \rangle \neq \langle \mathbf{v}T \rangle$, where $\langle \cdot \rangle$ denotes a epace-time average, and the difference may be very large. Much of physical oceanography has been based upon the unstated assumption that quasi-synoptic measurements represented

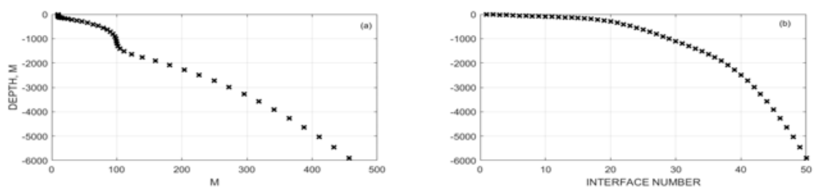

Figure 1: (a) Level thicknesses; (b) level depths in the ECCO version 4 of the MITgcm. {interfaces_la

the mean motion. Thus e.g., the calculation of Sverdrup balance, or of "abyssal recipes", are implicitly steady-state results, despite the common use of individual hydrographic sections. Here true 20-year average estimates are now possible. This description and discussion thus largely focusses on the properties of single variables, T, u, etc., their 20-year means and estimates of the deviation from those means. As Part 1, this paper is confined to the hydrographic products, T, S and their implications for surface elevation, mixed layer depth, deformation radii, etc. The velocity field and its property transports are discussed in Part 2. Most emphasis is placed on the global fields. A number of higher resolution, regional versions, of the state estimate exist (e.g., Gebbie et al., 2006; Mazloff et al., 2010), and a high northern latitude version is forthcoming (An Nguyen, personal communication, 2016), but these are not further discussed here.

All of the ECCO system output described here is available in Matlab form at: http://mit.ecco-group.org/opendap/diana/h8_i48/contents.html[3] as 20-year means, 20-separate annual means, 20-year average individual months, and 20-year average seasonal means (DJF, MAM, JJA, SON) on a grid in 50 vertical levels, of thickness plotted in Fig. 1. Many studies are best done in isopycnal-like coordinate systems; but the present description is confined to calculations in geometrical (latitude-longitude-depth) coordinates, with the interpolations to isopycnals postponed (but see Speer and Forget, 2013 for a mode water discussion).

2 Temperature Field

Data Misfits

Figs. 3-4 show the misfit to the mean temperature over 20 years at two different levels.[4]

[3] Or contact Carl Wunsch directly (cwunsch@mit.edu) for data or advice.

[4] The projections used here are the so-called loximuthal, with the Atlantic placed close to the center. The rationale is that this form both avoids the visual dominance of the tropical Pacific–which tends to get excess attention—and shows the Arctic as a reasonable fraction of the total. Color scales mostly follow the advice of Thyng et al. (2016) as both most suitable for colorblind individuals and with the least visual distortion of the

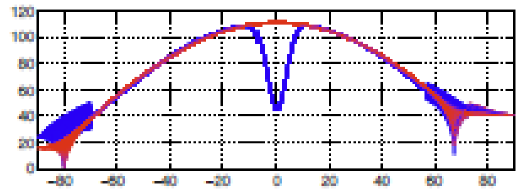

Figure 2: Latitude (blue curve) and longitude spacing in kilometers as a function of latitude (from Forget et al., 2015). Higher latitude spacing exists near the equator. At high latitudes the more complex grid leads to a distribution of spacings (see Figs. 1,2 of Forget et al., 2015). Most of the high latitude southern region is land. {forget_etal_f

Values are calculated from point values where available and then gridded. Although some systematic misfits do appear, particularly in the region of the unresolved western boundary currents and near-surface in the tropical oceans, the bulk of the system is within a fraction of a degree of the observed averages. Although not shown here, misfits can be readily computed for each year, each season, and each month if desired. In an ideal world, the misfit values should be Gaussian, here roughly consistent with the displayed histograms.

The implications of regional misfits to observations is a problem generic to the use of *any* general circulation model: if a model fails to adequately mimic the observations in a particular place at a particular time, does that render useless the solution in other regions and times? The existence of the adjoint (dual) solution as part of the state estimate permits, in the present situation, an answer in terms of global sensitivities computed from the dual (e.g., Heimbach et al., 2011). That discussion is postponed to Part 3 of this climatology.

Estimated Solutions

A representative set of horizontal charts and vertical sections is displayed here. For temperature, the charts and sections are oceanographically qualitatively consistent with conventional descriptions of the large-scale, averaged oceanic circulation. Thus for example, the 20 year average temperatures at 5 and 105m in Figs. 5, 6 show all of the conventional near-surface gyres, the strong Southern Ocean thermal fronts, the upwelling regions off Africa, California and South America, as well as numerous other expected features. The differences between these two maps are a rough measure of the mixed layer temperature gradient (discussed below). Some mapped values are shown with a histogram of their distribution; where not shown they are typically Gaussian—or at least unimodal. Most property anomalies are strongly unimodal; time average

fields.

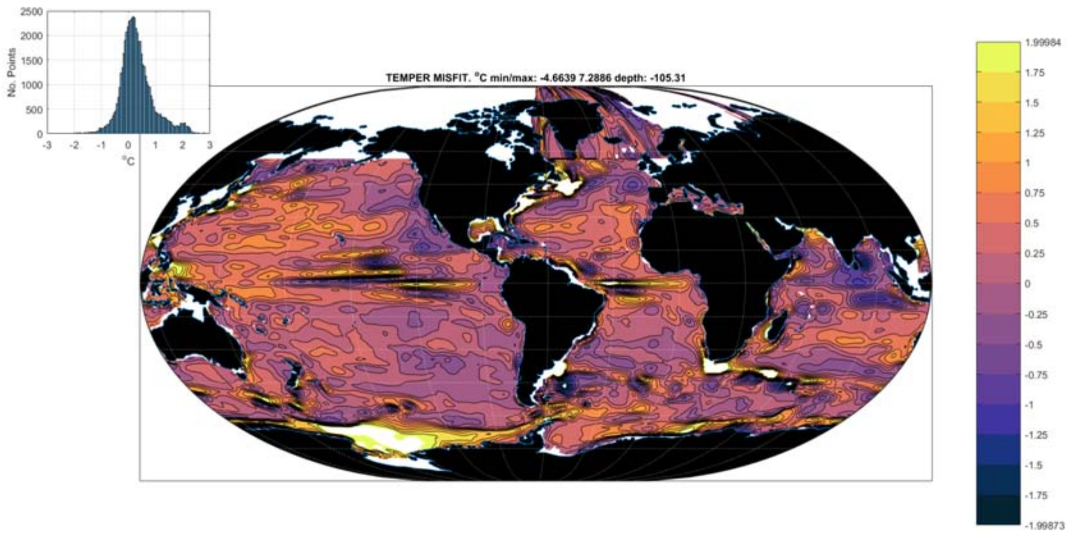

Figure 3: Misfit to the 20-year average temperature (°C) at 105m including Argo, XBT, CTD, and elephant seal profile data. Inset shows a histogram of values. A small number of outliers here and in other charts have been suppressed. {misfit_temper

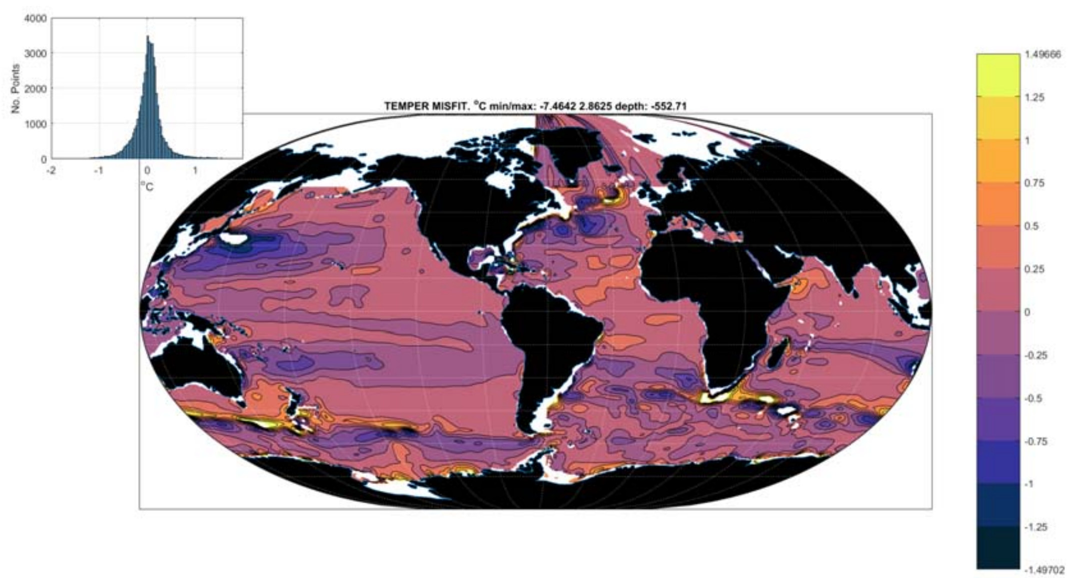

Figure 4: Same as Fig. 3 except at 553 m. {misfit_temper

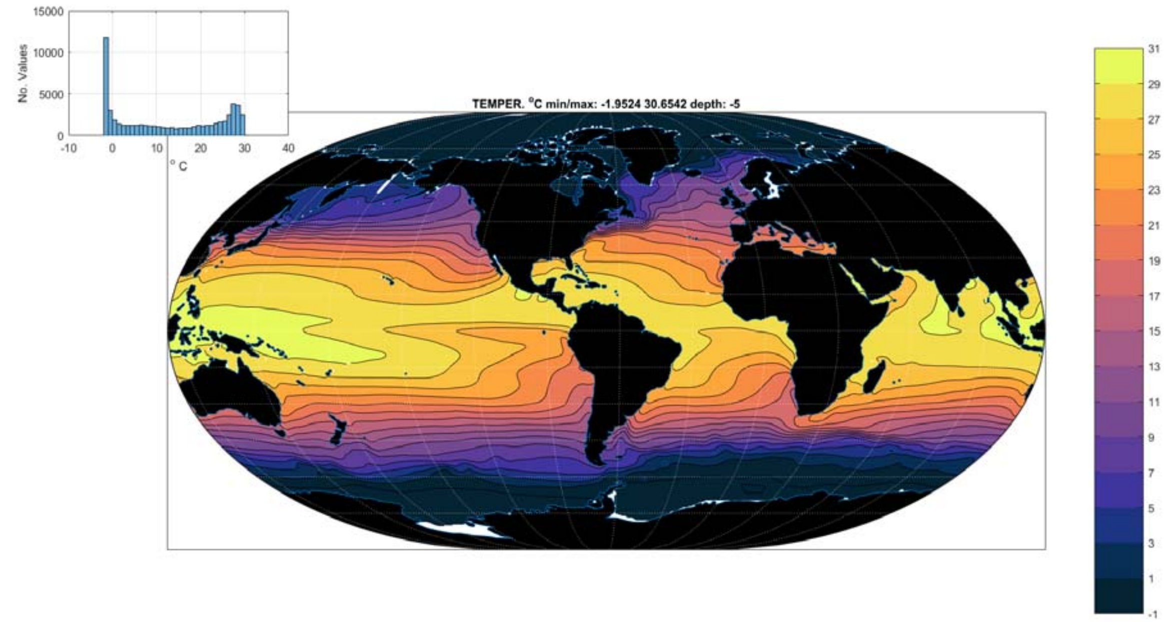

Figure 5: Twenty-year mean potential temperature at 5m depth (°C). Inset shows the histogram of values.

{temperature_2

properties usually are not. An example of the deep temperatures is shown in Fig. 7 near 2100m depth.

At 2100m (Fig. 7) the Atlantic Ocean warmth relative to the rest of the world is obvious, as is the large-scale thermal gradients extending away from the Southern Ocean.

A few traditional potential temperature sections are shown in Figs. 8-11. As compared to standard atlas sections (e.g., the WOCE Atlas Series) they display, as expected, similar large-scale features, but tend to be considerably smoother. Nonetheless, a number of small scale features survive the 20-year averaging, particularly in the Southern Ocean (Fig. 10).

Global Mean temperatures:

The 20-year mean temperatures of the global ocean, including the full Arctic, are shown in Table 1. Volume-weighted global average temperature is 3.32°C as compared to Worthington's (1981) estimate of 3.51°C, but who had no Arctic and very few Southern Ocean values (see his Fig. 2.1 and Fig. 10 here). Table 1 lists volume-weighted mean temperatures, while the ad hoc standard errors are the raw standard deviation of the unweighted temperatures and salinities from the spatial variations of the 20-year means. They give a rough idea of the range of temperatures (and salinities) that enter. On the other hand, the standard errors of the

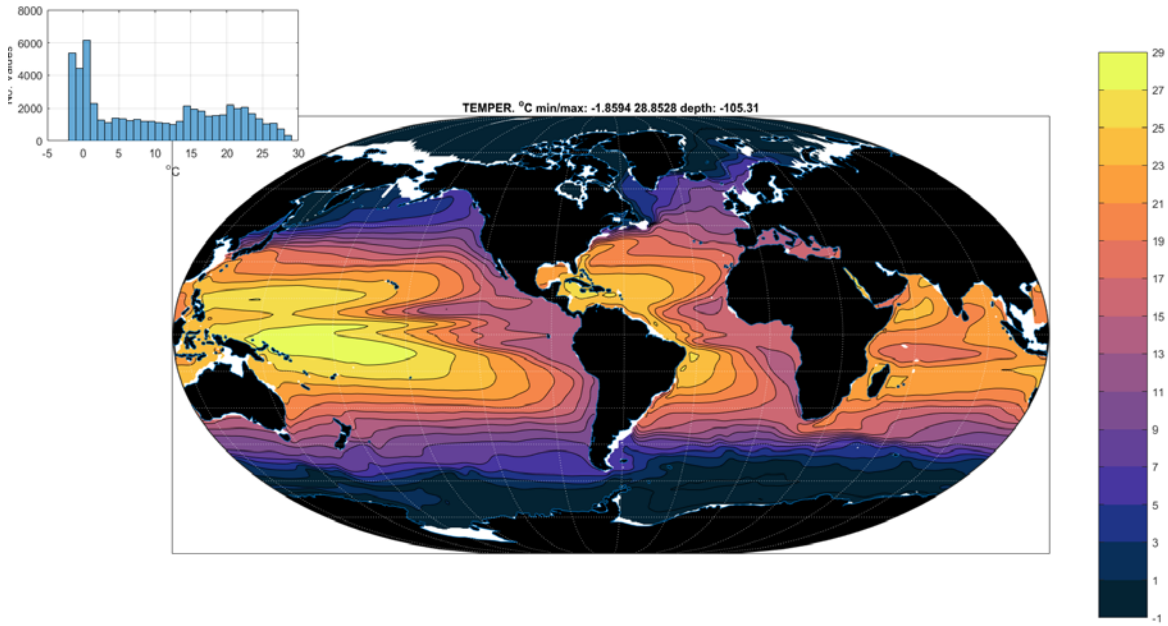

Figure 6: Twenty-year average potential temperature at 105m (°C). Note change in scale from Fig. 5. {temperature_2

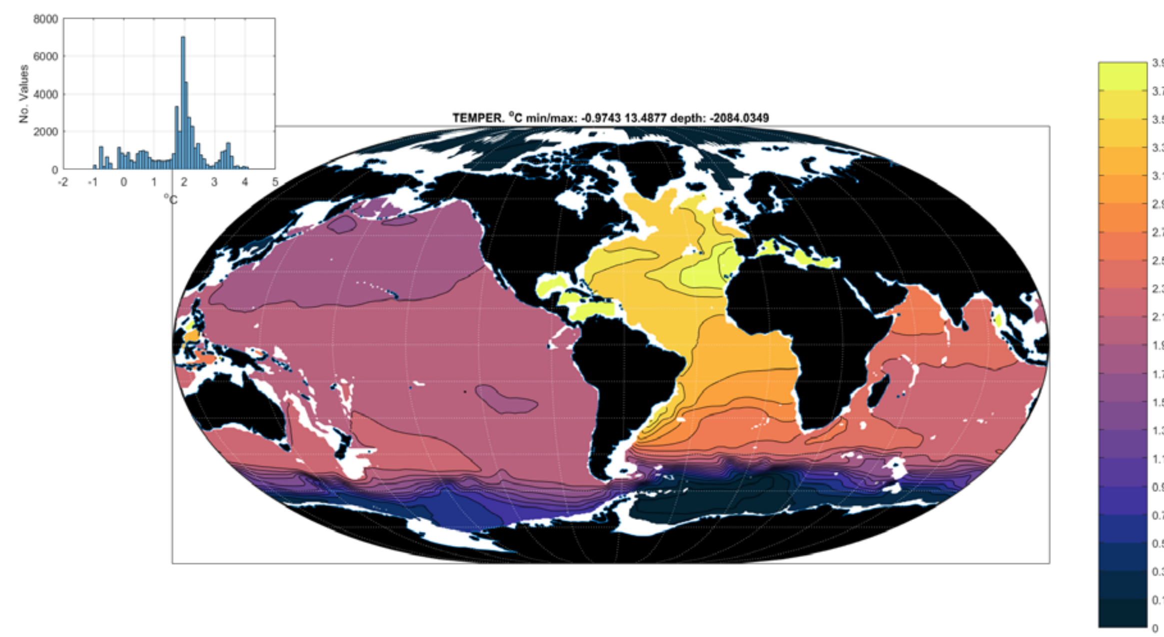

Figure 7: Twenty-year average temperature at 2084m (°C). Color saturates at 3.9 °C with the maximum approaching 13.5°C in the Mediterranean and Gulf of Mexico. {temperature_2

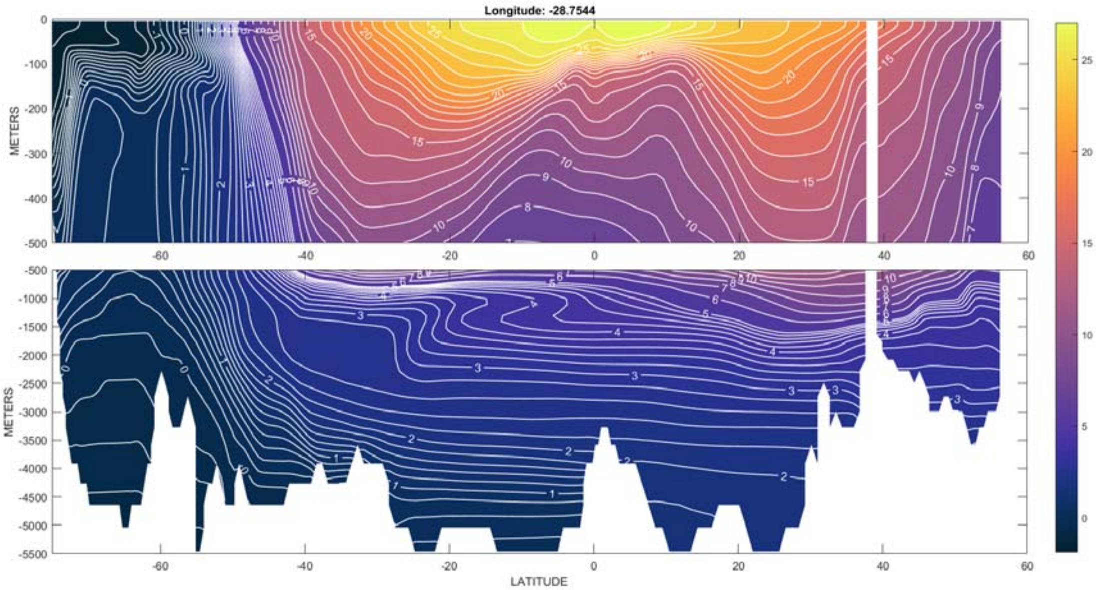

Figure 8: Twenty-year mean section (°C) of potential temperature down 28.8°W in the Atlantic ocean. {temp_20yearme

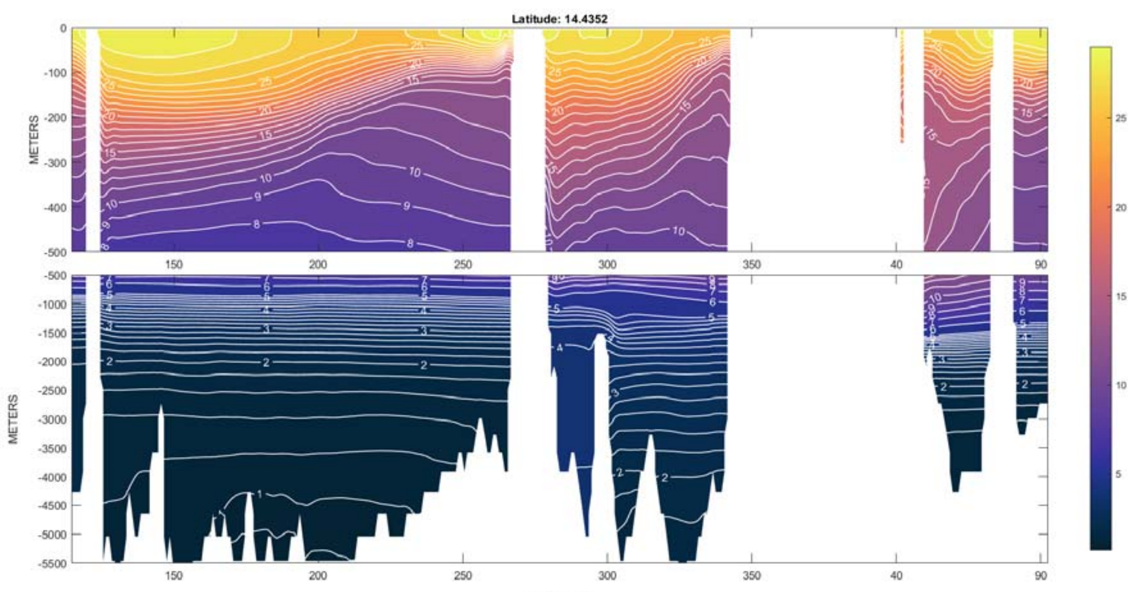

Figure 9: Twenty-year mean potential temperature in all three oceans along 14°N. {temp_20yearme

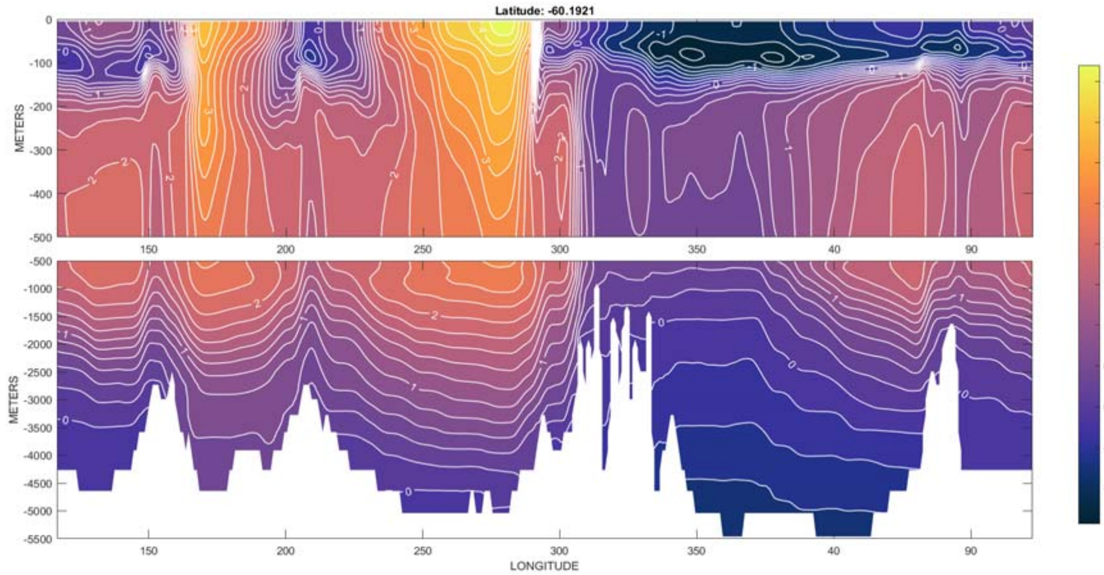

Figure 10: The twenty-year average temperature along 60°S through the Drake Passage. {temp_20yearme

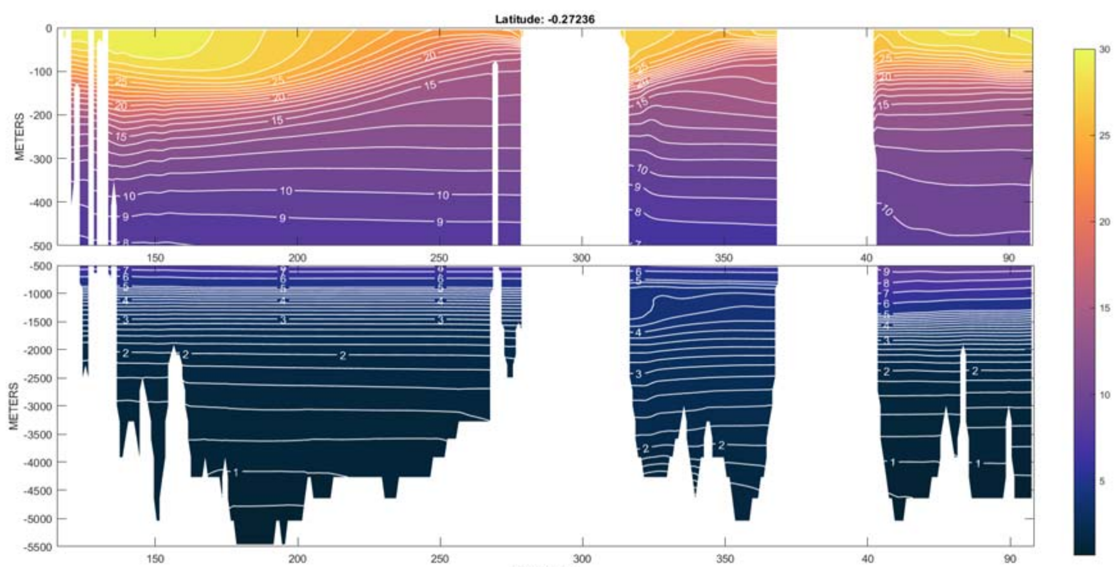

Figure 11: Equatorial 20-year mean potential temperature section. {temp_20yearme

Depth Range (m)	**Mass (Zetta (10^{21}) kg**	**Mean Temperature, °C**	**Mean Salinity, o/oo**
0-100	0.04	15.4(9.3)	34.74(0.10)
0-700	0.32	9.1(7.4)	34.74(0.10)
0-2000	0.90	5.2(6.4)	34.70(0.07)
0-3600	1.5	3.8(6.0)	34.72(0.06)
3600 to bottom	0.31	0.9(0.34)	34.73(0.003)
0 to bottom	1.7	3.32(6.7)	34.72(0.06)

Table 1: Mean temperatures and salinities over 20 years as integrated to various depths. Parenthetical values are the standard deviation of the annual mean temperatures and salinities going into the calculation. They are not any sort of standard error. Standard deviations of volume weighted temperatures are far smaller (e.g., $2x10^{-5}$ degree C). A constant density of 1029 kg/m^3 was used in computing the total masses for each depth range, and which are also displayed. {table_vols}

fractional volume weighted temperatures are far smaller: e.g. for the global mean temperature, that standard error is 4×10^{-7}°C, but which is in large part a measure of the volumetric variability assigned to each temperature under the pretence of statistical independence of each value. Let V_{ijk} indicate the volume occupied by any grid box, at horizontal location indices i, j, and with depth index k. Fig. 12 shows the distribution of fractional values $T_{ijk}V_{ijk}/\sum_{ijk} V_{ijk}$ in the 20-year mean temperatures. There the vertical index k ranges over the top 100m, and over the full water column. The bimodal, non-normal distribution renders an ordinary variance estimate of the mean not particularly meaningful. Useful uncertainties would come from computing means from resampling strategies dictated by actual observational distributions (e.g., Wunsch, 2016; Boyer et al., 2016), but which is not carried out here. Such estimates depend sensitively on statistical assumptions about the space-time distribution for “infilling” purposes.

2.1 Annual Changes

Figs. 13-16 show individual year-long average anomalies relative to the 20-year average at two representative depths. Apart from major regional features (e.g., the Gulf of Alaska and the Indo-Pacific tropics), these results emphasize the very intricate patterns appearing, and the consequent highly challenging space/time sampling program for forming large-spatial scale means.

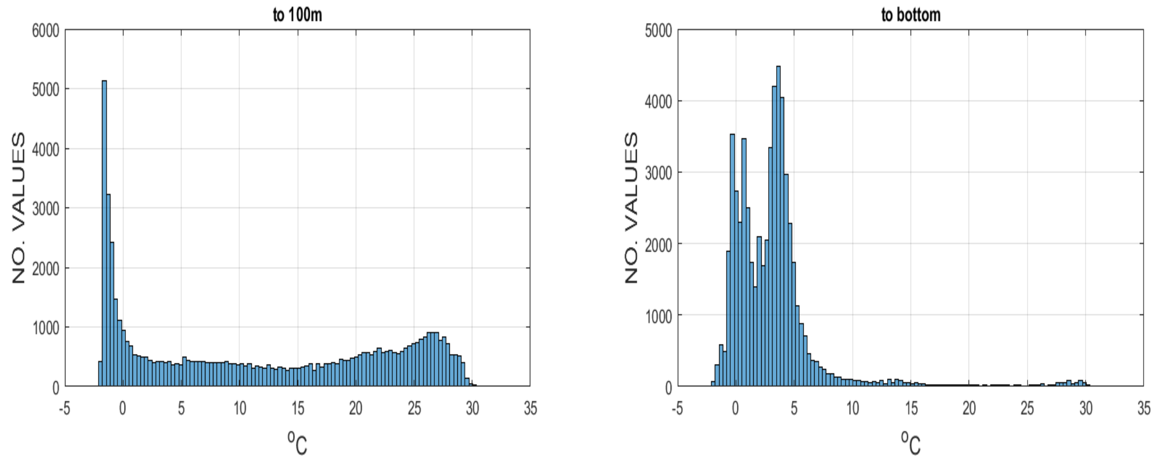

Figure 12: (Left panel). Histogram of volume weighted temperature values of $T_{ijk}V_{ijk}/\sum_{ijk} V_{ijk}$ for the global 20-year temperature mean in the top 100m of the model. (Right panel) Same as the left panel except for the entire water column. ijk are the three grid box indices, V_{ijk} is the volume assigned to temperature T_{ijk}. Note the bimodal nature of the distributions and the long-tail for the top 100m values. See also, Fig. 5. {temp_20yrmean

Period & Fraction of Water Column	**1 W/m^2 Heating/Cooling Rate**	**1 mm/y GMSL Change**
1 Year, Full Depth	0.002°C	0.0015°C
20 Years, Full Depth	0.04°C	0.03°C
1 Year, Upper 700 m	0.01°C	0.008°C
20 Years, Upper 700 m	0.2°C	0.16°C
1 Year, Below 700 m	0.0025°C	0.002°C
20 Years, Below 700 m	0.05°C	0.04°C

Table 2: Approximate oceanic temperature changes implied by a 1 W/m^2 heating (or cooling)-rate over different times and depths, as well as the temperature change equivalent of a 1 mm/y global mean sea level (GMSL) change. For rough calculation purposes, the heat capacity $c_p = 4000J/kg/^oC$, $h = 3800m$, $\rho = 1029kg/m^3$, Expansion coefficients α are in the range $5 - 30x10^{-5}/C$ (Thorpe, 2005) and smaller near the freezing point. Modified from Wunsch and Heimbach (2014). {table2}

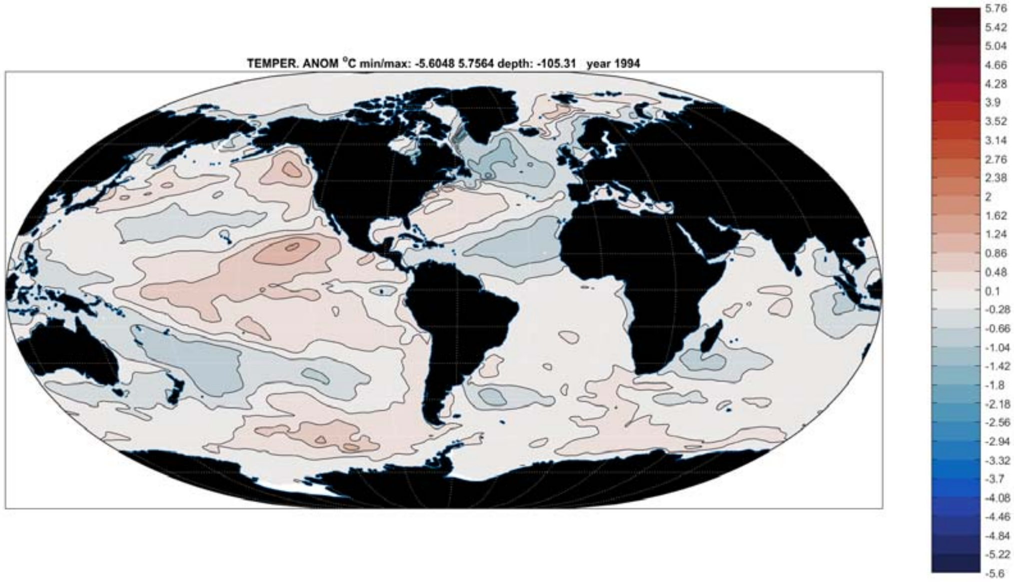

Figure 13: Anomaly of temperature in 1994 relative to the 20 year mean at 105m.

{temp_anom_199

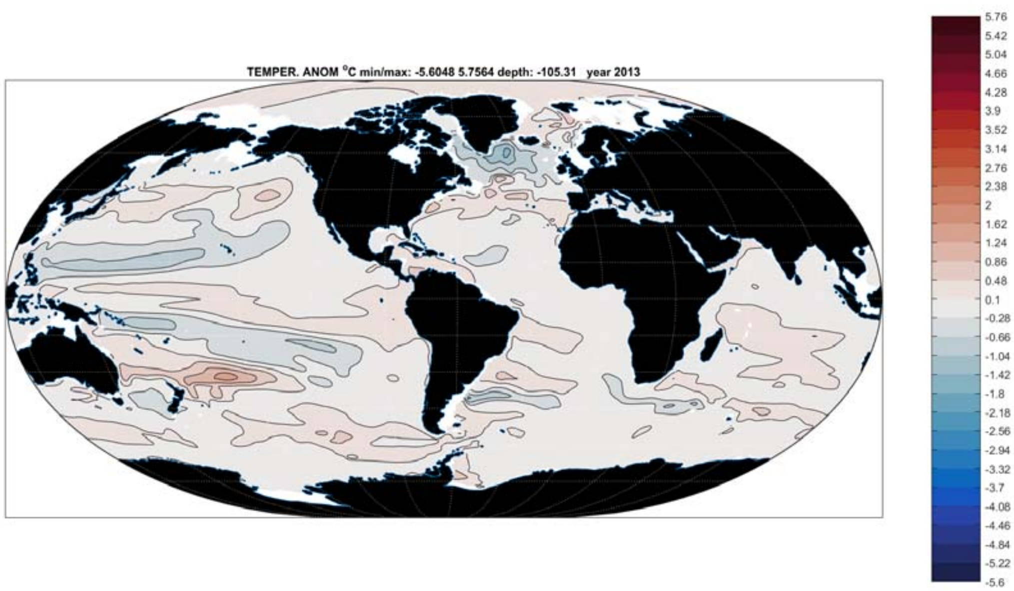

Figure 14: Twenty-year mean anomaly of temperature at 105m in 2013, twenty-years after that in Fig. 13.

{temp_anom_201

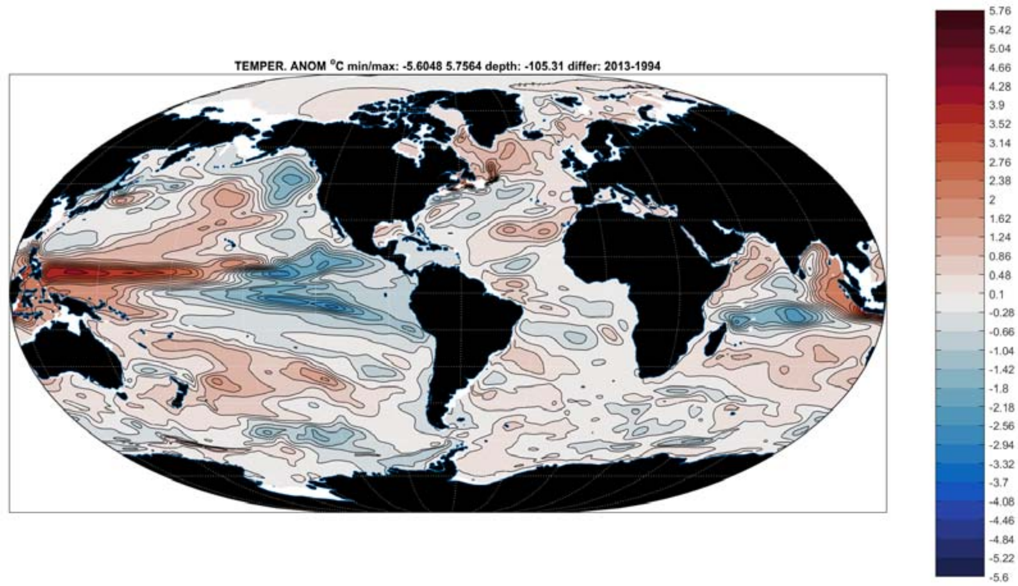

Figure 15: Change in temperature between 2013 and 1994 at 105m, the difference of Figs. 14 and 13. {temp_anom_201

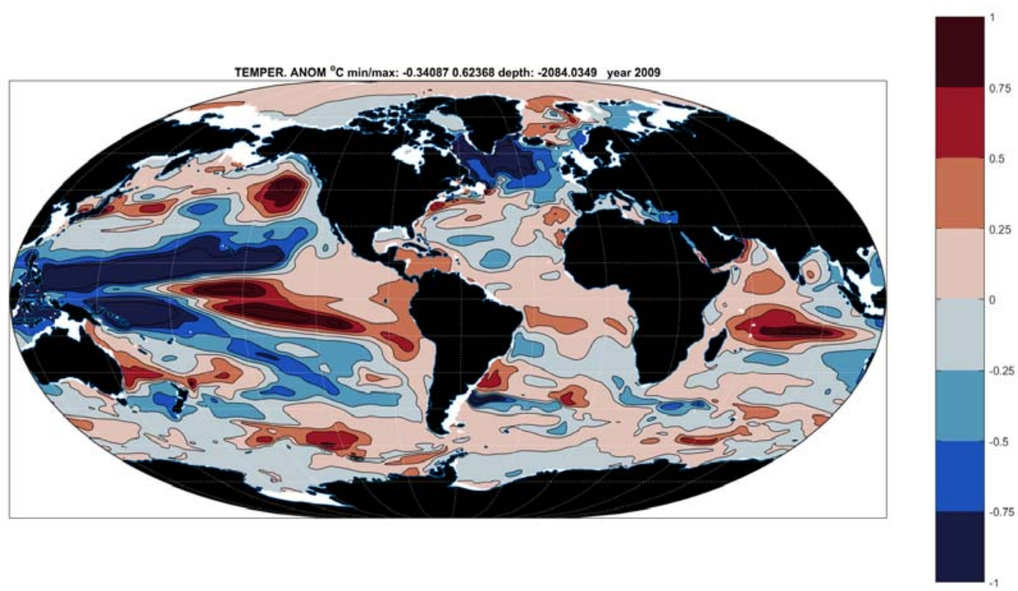

Figure 16: Temperature anomaly at 2100m in 1994 relative to the 20-year mean. {temp_anom_200

2.2 Heat Uptake

A large literature has grown up surrounding the notion of a "hiatus" in global warming during the nominal period 1998-2013. No consensus has emerged over the reality or significance of this phenomenon in the presence of very noisy, under-sampled sets of data as well as the exchanges (re-arrangements) of heat energy *within* the ocean itself. To the extent that the phenomenon is a real one, it has been argued that the ocean uptake of heat must have increased during that period, subject to the assumption of little or no change of net solar radiation during that interval. Conversion of out-of-equilibrium heating rates, which are minute compared to the background values, is not very intuitive. Thus Table 2 converts a net ocean uptake change of $1\mathrm{W/m}^2$ into an approximate temperature change, depending upon the depth over which the change is to be attributed. So for example, if the changed heat content all resides in the upper 700m, the mean temperature would change by 0.2°C in 20 years. Similarly, the Table also shows the temperature change over different layers that would lead to a 1mm/y change in global mean sea level. In terms of the ordinary, measured, oceanic temperature, the changes are dauntingly small.

The inferred 20-year change in heat content is depicted in Fig. 17, displaying the computed yearly-average global mean temperature anomaly for each year. Deeper values are accompanied by a least-squares fitting straight-line. The "abyssal" region, 3600m to the bottom shows a slight cooling. Heat content changes, involving the massive volumes in the deeper integrals, are tabulated in Table 3. A map of the vertically integrated heat content can be seen in Wunsch (2016) and see Liang et al. (2016a,b) for further discussion. Negative values in the abyss are most easily interpreted as owing to cooling there during the adjustment from the estimated initial conditions. Discussion of the linear fits and their statistical significance, if any, is left to the references except to say that no obvious evidence of a "hiatus" or other time-limited shift, appears.

The global mean ocean temperature shows an increase over 20 years to 2000m of 0.02°C (difference of first and last years and not a fitted trend). That change translates (Table 2) into a heating rate of $0.3\mathrm{W/m}^2$. The change to 700 m is 0.08°C translating into $0.13\mathrm{W/m}^2$ not inconsistent with numerous published estimates, including that of Wunsch and Heimbach (2014) from a previous state estimate. Although the upper 100m displays, as expected, a much larger noisiness, including e.g., the 1997-98 El Niño event, the deeper integrals display no such effect. The calculation of differences tends to remove systematic errors in the ECCO system, but a further quantification is not available. The total warming over 20 years includes the *cooling* below 3600m remarked by Wunsch and Heimbach (2014) which persists even with the inclusion

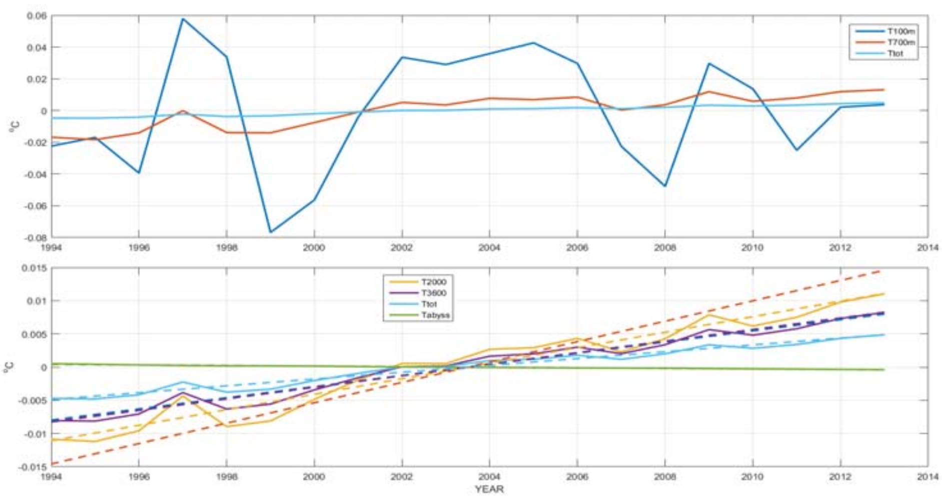

Figure 17: Volume weighted temperature change °C by year. Upper panel is the average to 100m and 700m, and lower panel the averages to 2000m, 3600m, the total top to bottom, and the abyssal layer below 3600m. Dashed lines are a best linear fit using a jackknifed estimate of the uncertainty in the values (not shown).

{heat_content_

Depth Range (m)	Mean Heat Content (YJ: 10^{24}J)	Temp. Change 20 Yrs °C	Warming 20 Year DifferenceW/m^2
0-100	2.6	0.03	0.02
0-700	11.6	0.03	0.13
0-2000	18.9	0.02	0.26
0-3600	22.2	0.02	0.32
3600-bottom	1.1	-0.09	-0.004
0-bottom	23.3	0.01	0.23

{meanheat}

Table 3: Time-mean heat content in the ocean by depth range in Joules. The net change, converted to W/m^2 , calculated from the difference between 2013 and 1994 is shown. Most of the oceanic mass lies below 700m. Mean temperatures are shown in Table 1.

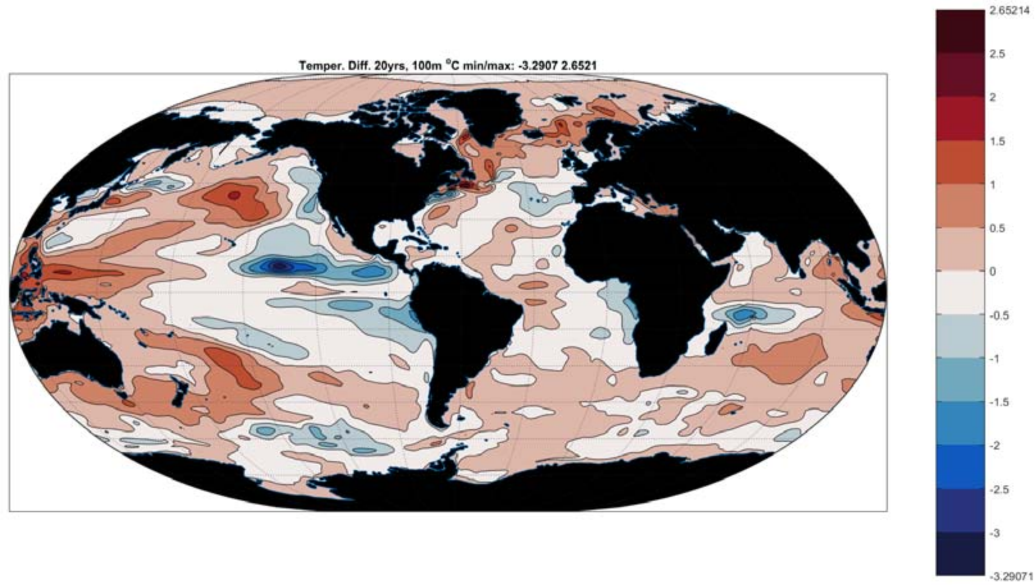

Figure 18: Vertical temperature difference over averaged over the top 100m from 2014-1993. A La Niña pattern is visible, but embedded within a complex structure of global change.

{temp_lastminu

of 0.1W/m^2 average geothermal heating[5].

Changes in heat content, as reflected in temperature, have a complex spatial pattern varying with depth. Figs. 18-20 show the column averaged temperature differences for three representative depths, including the top-to-bottom. These are presumably the result of interior redistributions, and air-sea fluxes over the 20 years. As always, the irregular sampling distribution for in situ measurements used alone is challenging if accurate global means are required. Standard deviations of the annual means, which become part of the discussion of sampling strategies, are shown in Figs. 21-22 again depicting the strong regionality. Instantaneous standard deviations are necessarily far larger. Huge standing reservoirs of thermal energy in the ocean, and the very small dis-equilibrium of the climate system, renders accurate determination of the very slight reservoir changes to be a difficult problem.

2.3 Annual Cycle

The largest ongoing climatological signal is the seasonal oscillation. Vinogradov et al. (2008) have described the seasonal cycle of sea level in an earlier ECCO state estimate. Fig. 23-26

[5] More precisely 0.095 W/m^2.

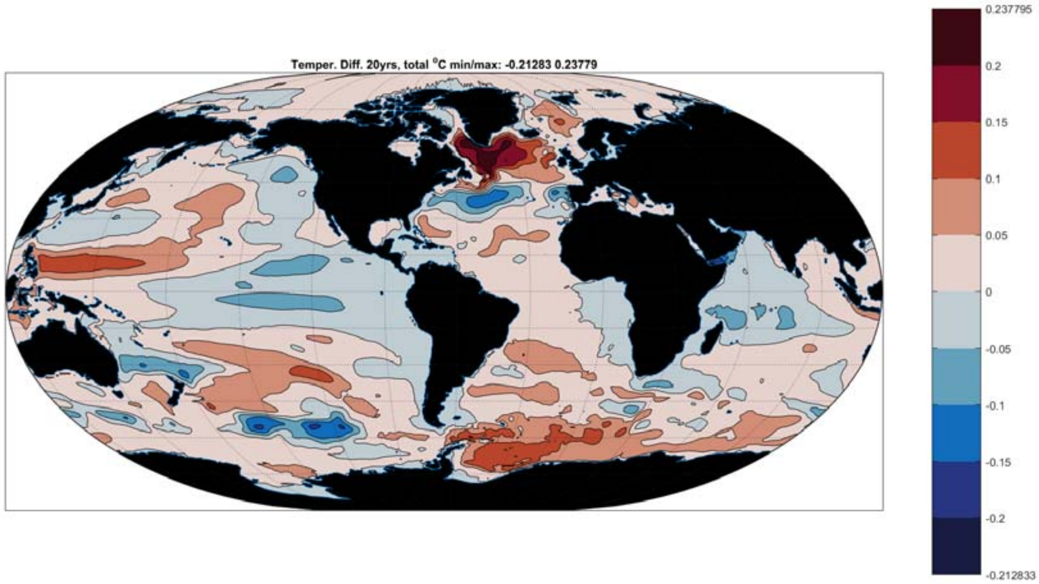

Figure 19: Vertical average temperature change, top-to-bottom, 2013 minus 1994 in °C. {temp_differen

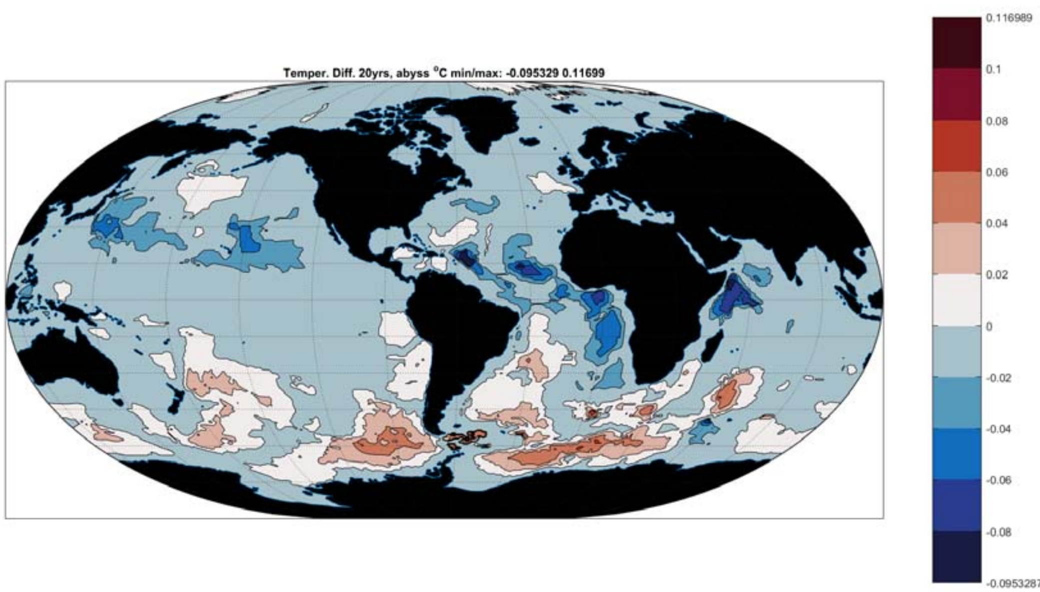

Figure 20: Abyssal temperature change, 3600m to the bottom, over 20 years. The warming of the Antarctic Bottom Water (Purkey and Johnson, 2010) is apparent, with a cooling over much of the rest of the ocean (see Wunsch and Heimbach, 2014). {temp_lastminu

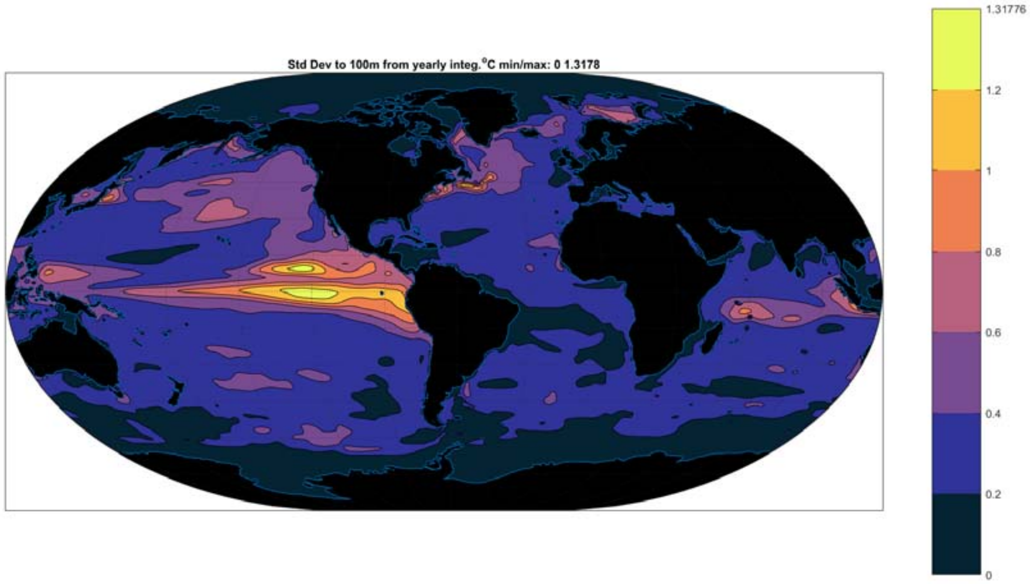

Figure 21: Standard deviation of temperature (°C) averaged over top 105m based on yearly variations. {temp_stdev_to

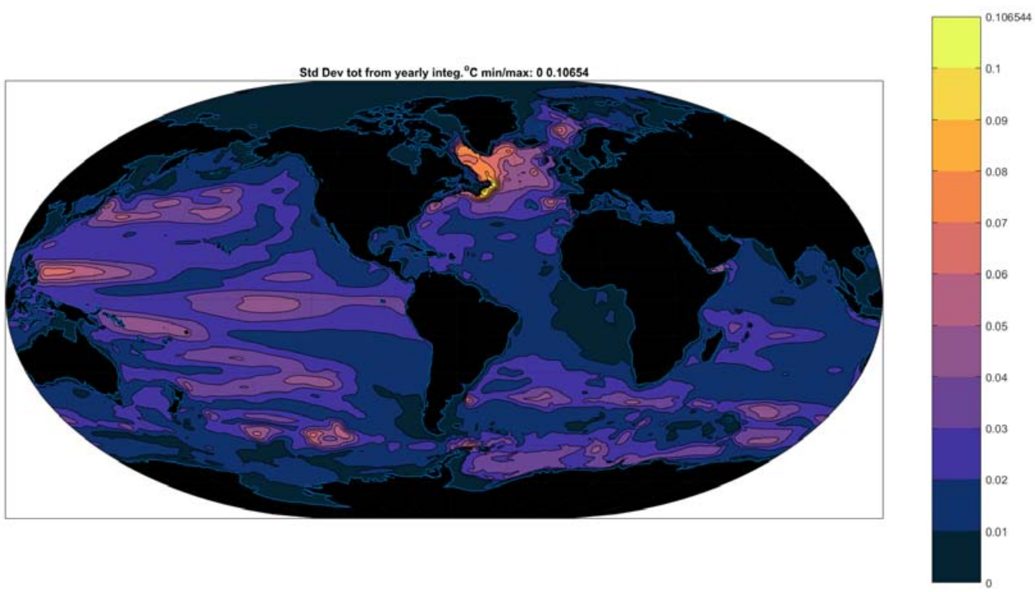

Figure 22: Vertical average temperature, (°C) top-to-bottom, standard deviation based on annual fluctuations. Relatively intense values in the northwestern Atlantic Ocean need to be rationalized (some discussion is provided by Hakkinen et al., 2013). {temp_stdev_to

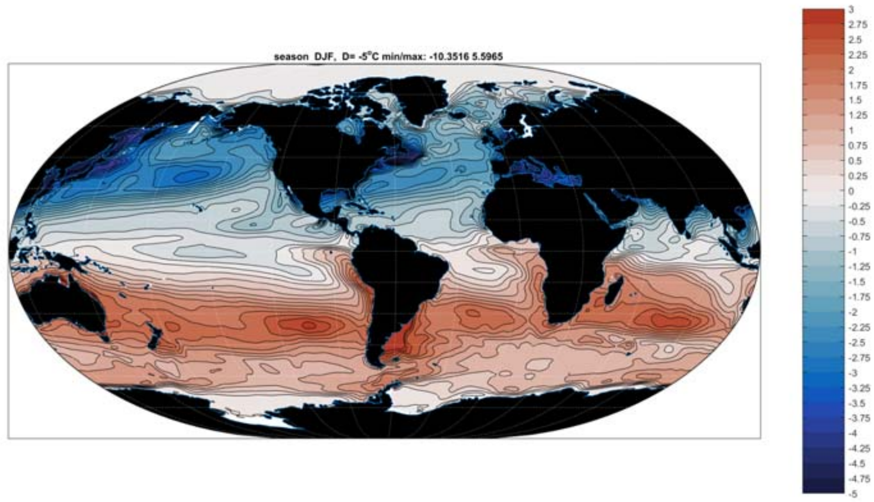

Figure 23: Seasonal (December, January, February, DJF) mean 5m temperature anomalies. The main feature is the interhemispheric anti-symmetry with the conventional larger amplitudes in the northern region.

{temp_djf_5m.t

displays the four seasonal temperature anomaly means at the 5m level in the present estimate. The largest signals are in the shallow regions on the eastern coasts of Asia and North America where the continental meteorology first encounters the ocean.

Non-equatorial vertical propagation of seasonal forcing tends to be suppressed rapidly with increasing depth (Gill and Niiler, 1973). Some understanding of the overall depth/spatial structure of the seasonal cycle can be obtained from the singular value decomposition of the seasonal average temperature. With four seasons, only four pairs of singular vectors fully describe the patterns, and because the time average of the anomalies vanishes, only three pairs are required. The singular values are 2706, 1083, 436. Figs. 27-29 show the most energetic component $\mathbf{u}_1$ for three depths. But from Fig. 30, on the spatial average, the annual cycle in temperature penetrates only to about 100m, and beneath that depth (in the spatial average) it is negligible.

3 Salinity Field

Data Misfits

Twenty-year average salinity misfits are displayed in Figs. 31, 32. Largest values and outliers are at continental margins where model resolution is inadequate, and where issues concerning land runoff data accuracies persist.

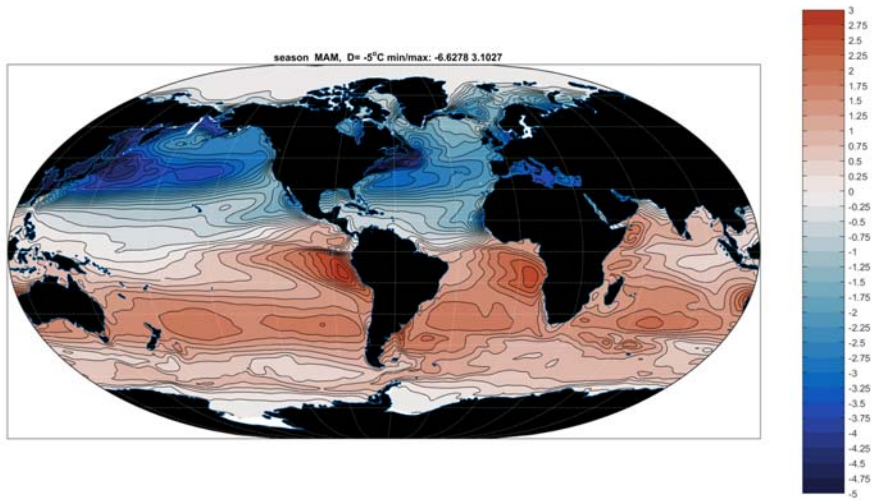

Figure 24: Twenty-year average temperature anomaly March, April, May at 5m. {temp_mam_5m.t

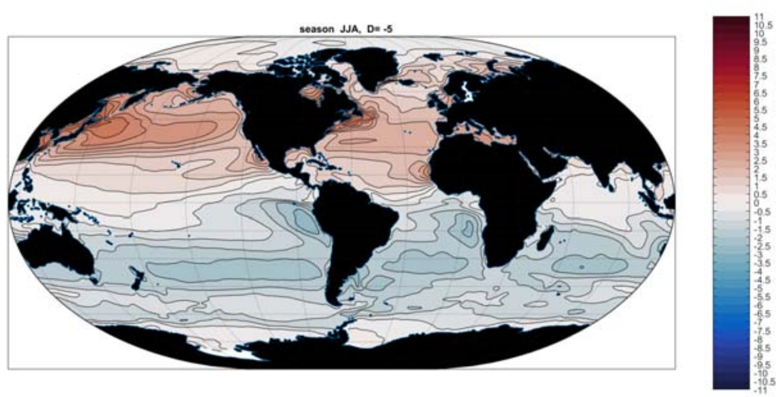

Figure 25: Twenty-year average temperature anomaly at 5 m, June, July, August. {temp_jja_5m.t

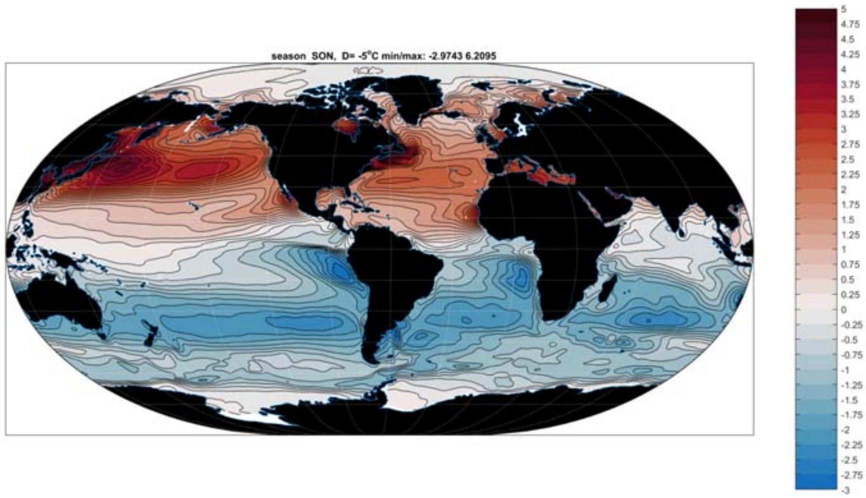

Figure 26: Twenty-year seasonal mean temperature anomaly at 5m September, October, November. {temp_son_5m.t

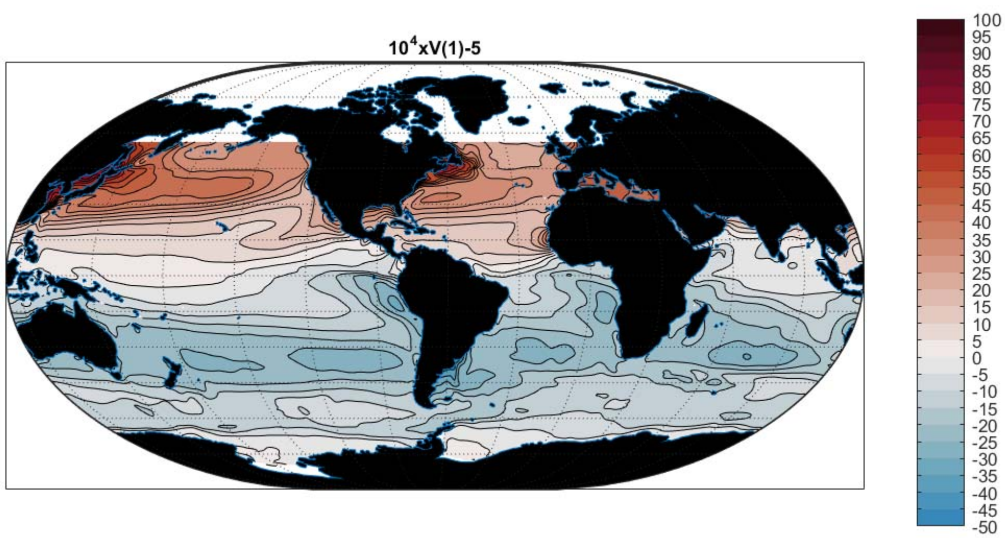

Figure 27: The first EOF (singular vector) of temperature at 5m. multiplied by 10^4. Values are dimensionless with units being ascribed to the singular values. {temp_v1svd_5m

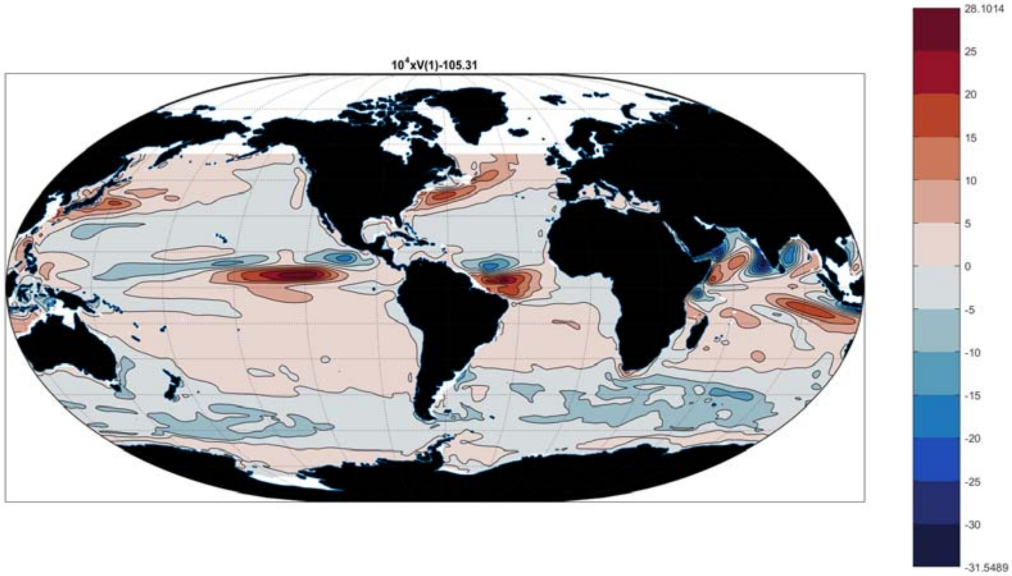

Figure 28: Same as Fig. 27 except at 105m. {temp_v1svd_10

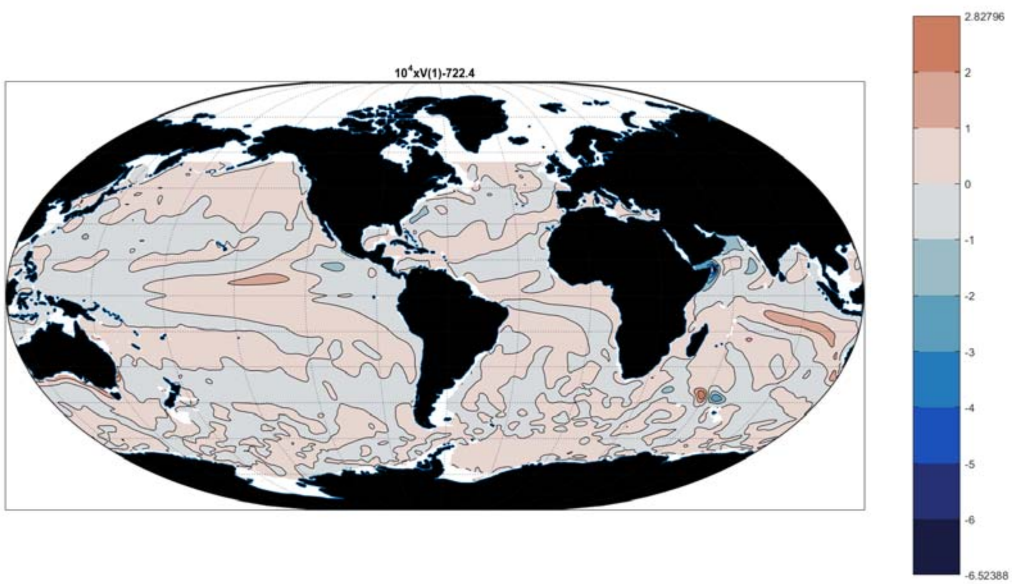

Figure 29: Same as Fig. 27 except at 722m. A monsoonal response is visible, particularly in the eastern and western tropical Indian Ocean. Otherwise, the annual cycle at this depth is effectively negligible. {temp_v1svd_72

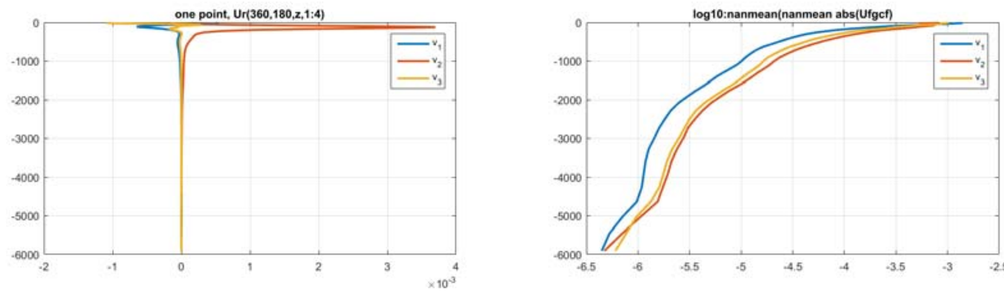

Figure 30: (Left panel) The first three singular vectors of the annual cycle in temperature as a function of depth at one point on the Atlantic equator (0°E, 0°N). (Right panel). Logarithm of the areal mean as a function of depth of the 3 singular vectors of temperature. The annual cycle in temperature is effectively confined to the top 100m of the ocean. {temp_svd_viwi

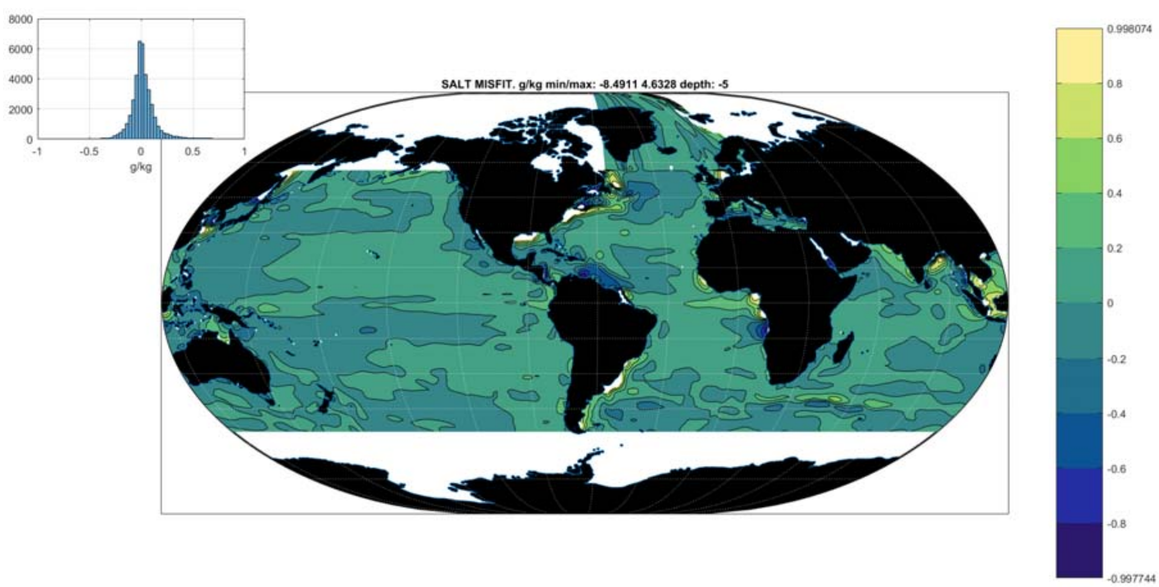

Figure 31: Misfit of the state estimate to the salinity data averaged over 20 years at 5m—effectively the surface. (g/kg). {misfit_salt_5

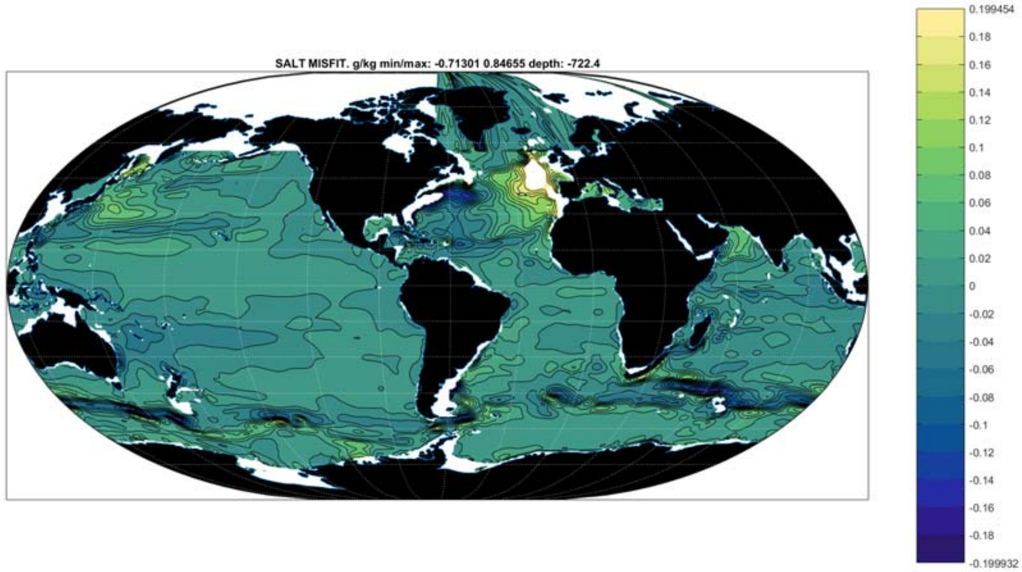

Figure 32: Same as Fig. 31 except at 722m. {misfit_salt_7

Salinity Charts

A number of representative maps and sections are shown in Figs. 33-39. These are again broadly consistent with historically available estimates.

The global mean salinity (volume weighted) is 34.72, fortuitously identical to Worthington's (1981) estimate from a very sparse data set. Apparent changes in upper ocean salinity over 50 years have been discussed e.g., by Durack et al. (2012) and Vinogradova and Ponte, (2016). The histogram of the distribution of salinity is in Fig. 40, showing the comparatively narrow range existing over the oceanic bulk.

3.1 Regional Examples

As an example of what can be done regionally with salinity, Fig. 41 displays the twenty-year seasonal average anomalies at 5m depth of salinity in the Bay of Bengal (see e.g.,the special issue *Oceanography*, 29(2), 201) for a comparison).

Among other regional applications is that of Pillar et al. (2016) in the North Atlantic, and which includes a sensitivity analysis using the dual solution (see also, Part 3 of this series), Wunsch (2010) for the Indonesian Throughflow, Buckley et al. (2014, 2015) and Evans et al. (2017) for North Atlantic changes.

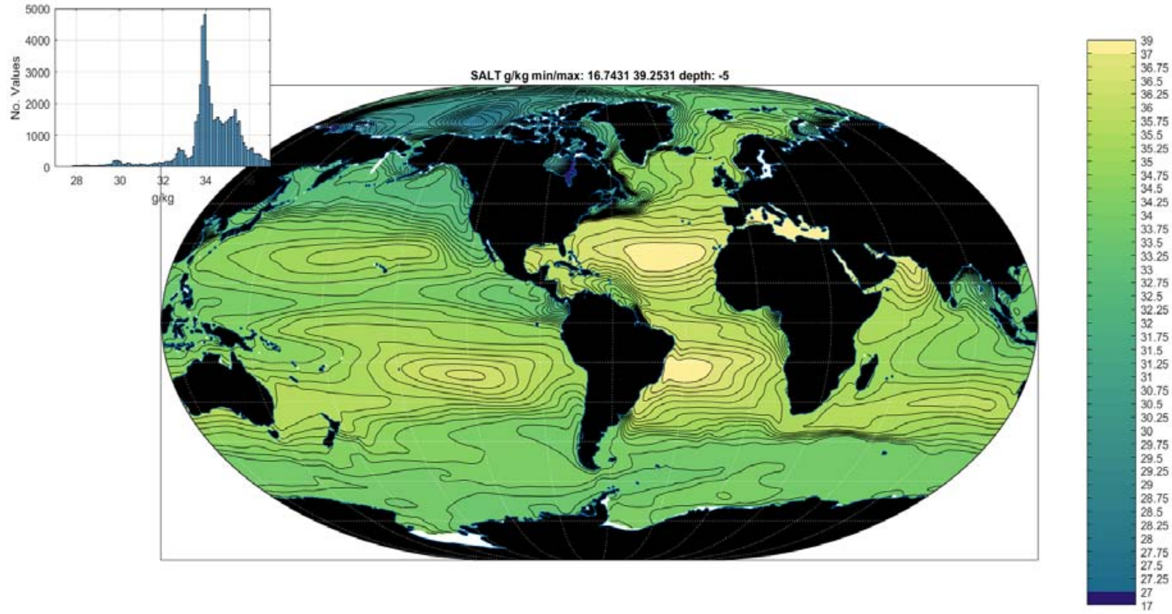

Figure 33: 20-year average salinity, g/kg, at 5m depth. {salt_20yrmean

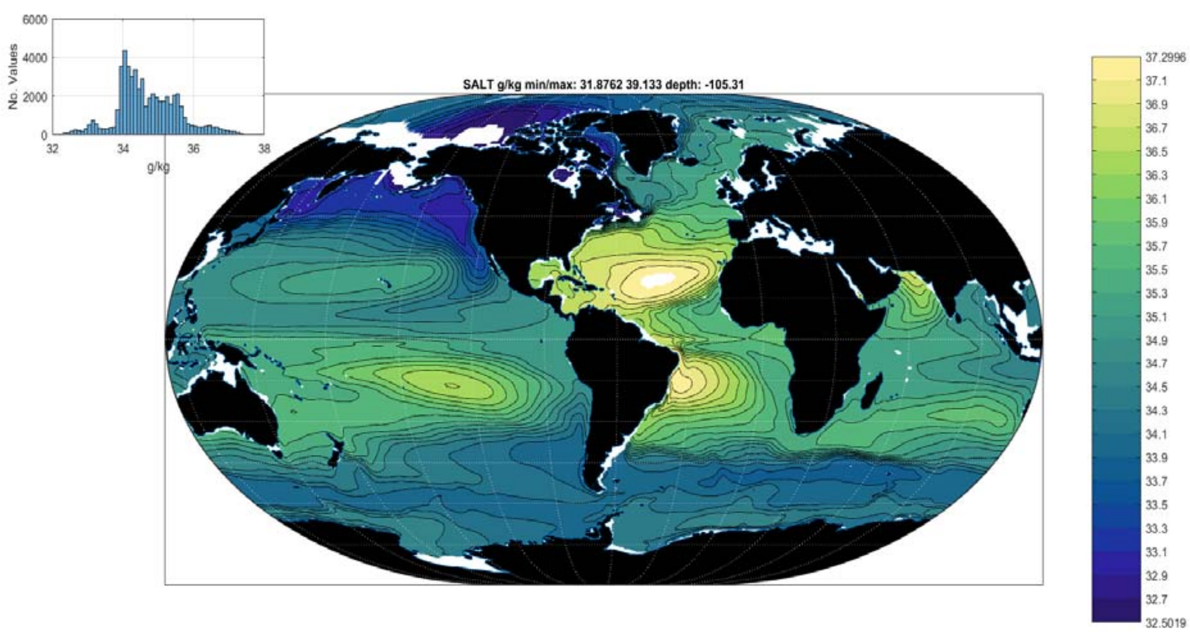

Figure 34: Twenty-year mean salinity (g/kg) at 105m depth. A marked difference with the near surface (5m) values is apparent. {salt_20yrmean

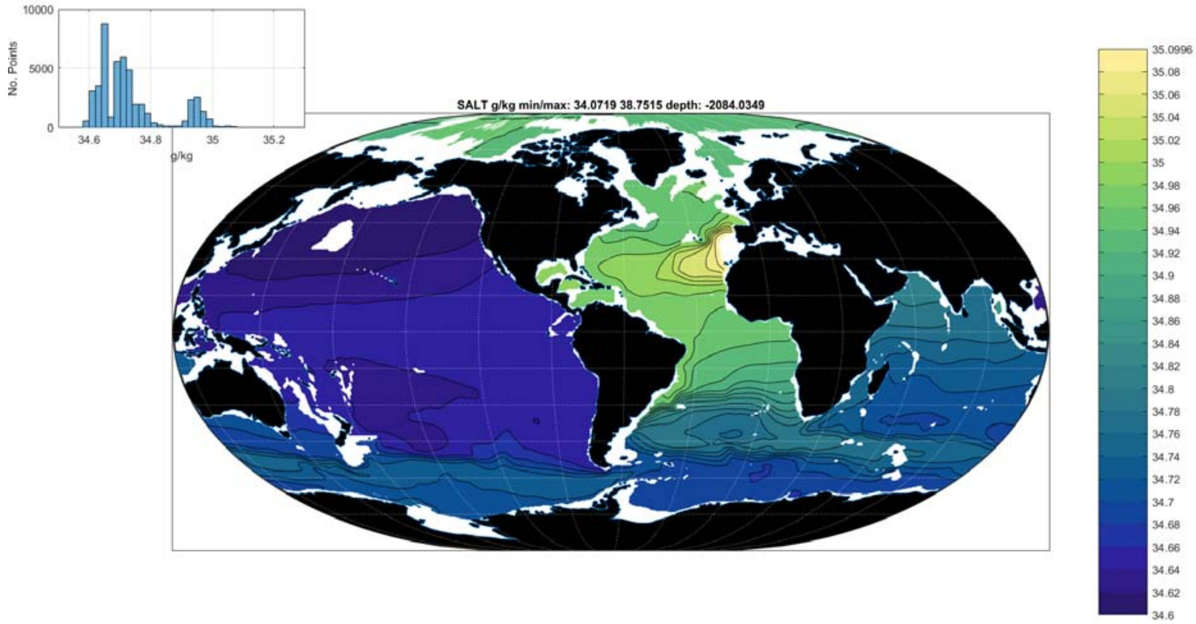

Figure 35: Twenty-year average salinity at 2100m. Excess values in the North Atlantic and the extreme of the Mediterranean Sea (values truncated here) are visible. The relatively saline Atlantic and fresh Pacific Oceans are apparent.

{salt_20yrmean

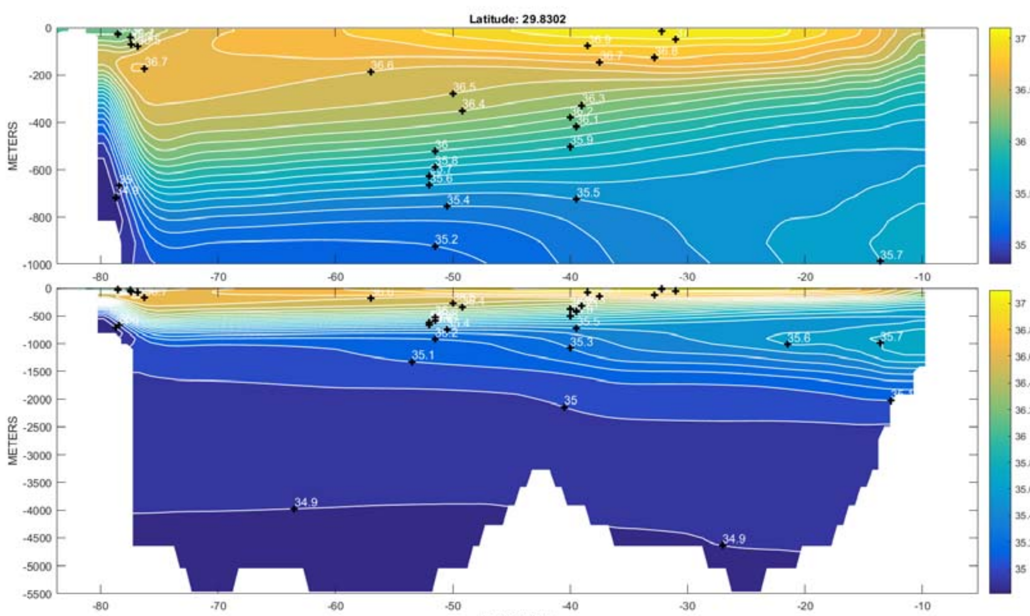

Figure 36: Twenty-year average salinity (g/kg) along a section at 30°N in the North Atlantic Ocean.

{salt_zonalsec

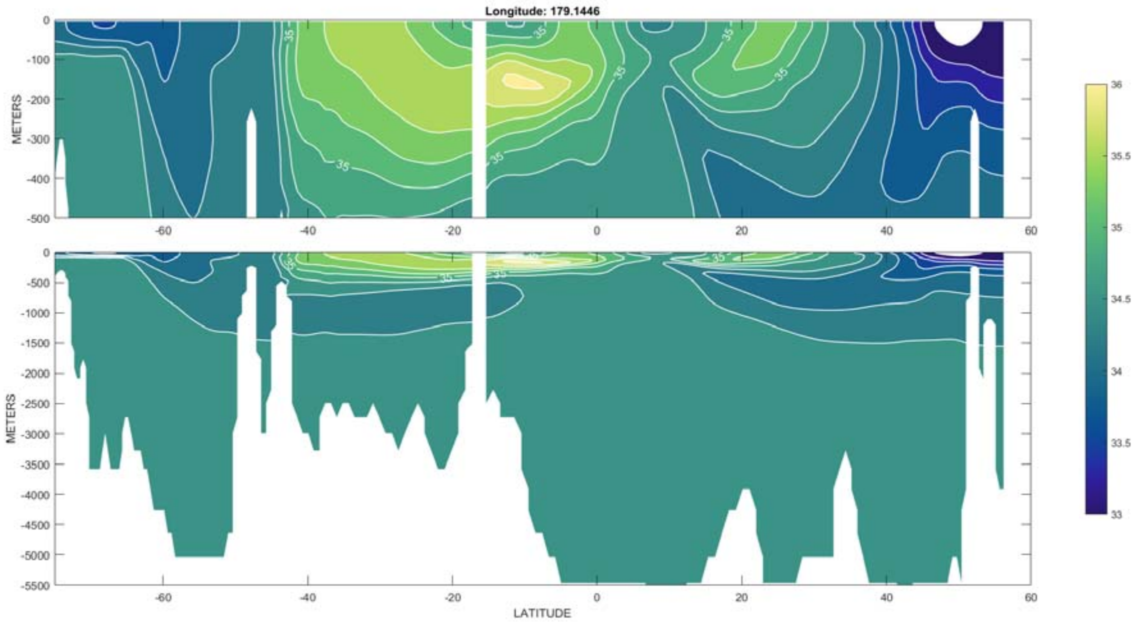

Figure 37: Meridional section of 20-year average salinity(g/kg) along 180°W in the Pacific Ocean. Note the presence of ice at the surface at the northern latitudinal extreme. {salt_20yrmean

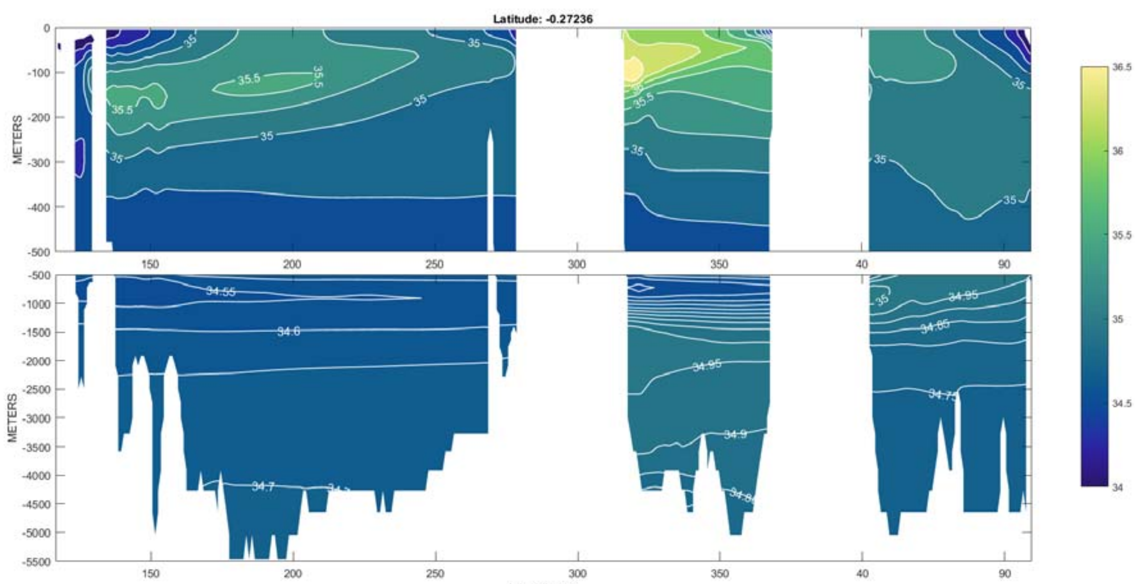

Figure 38: Twenty-year average salinity, g/kg, in a zonal section along the equator in all oceans. Note extra contours below 500m. {salt_20yrmean

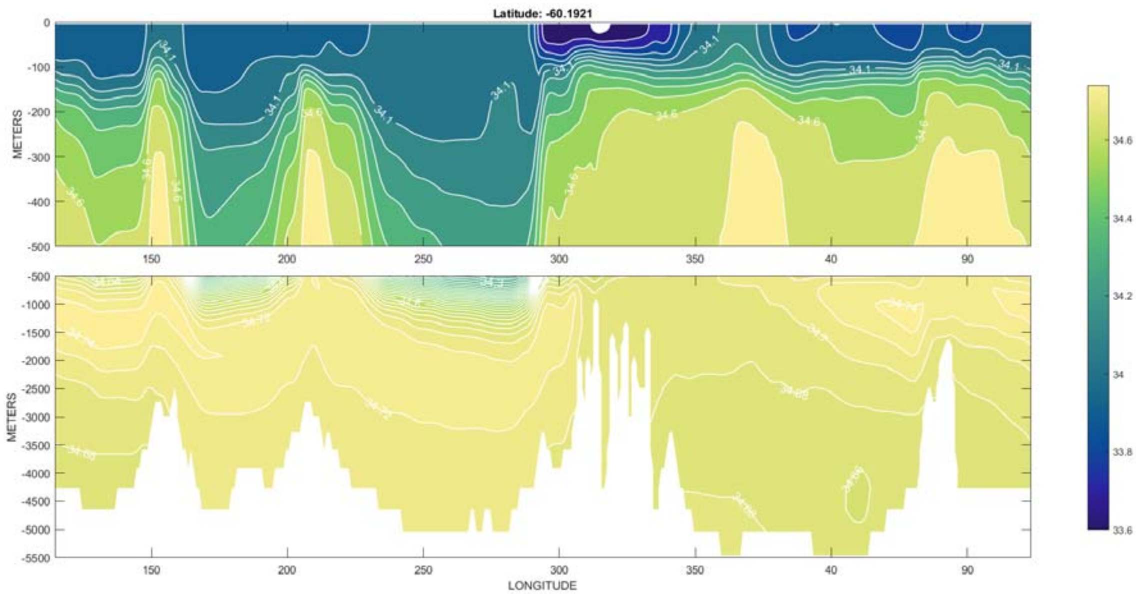

Figure 39: Twenty-year mean salinity in a zonal section through the Drake Passage with a complex zonal structure as seen also in temperature (Fig. 10) and producing a similarly complex zonally varying $T-S$ relationship in the Southern Ocean. {salt_20yrmean

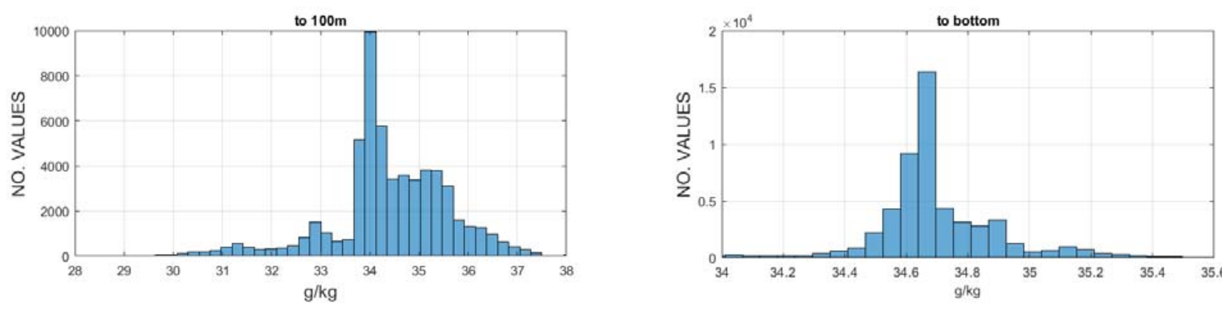

Figure 40: Histogram of salinity values averaged over the top 100m (left panel) and to the bottom (right panel). The latter is truncated so that some very small numbers of outliers are not shown. {histo_salt_20

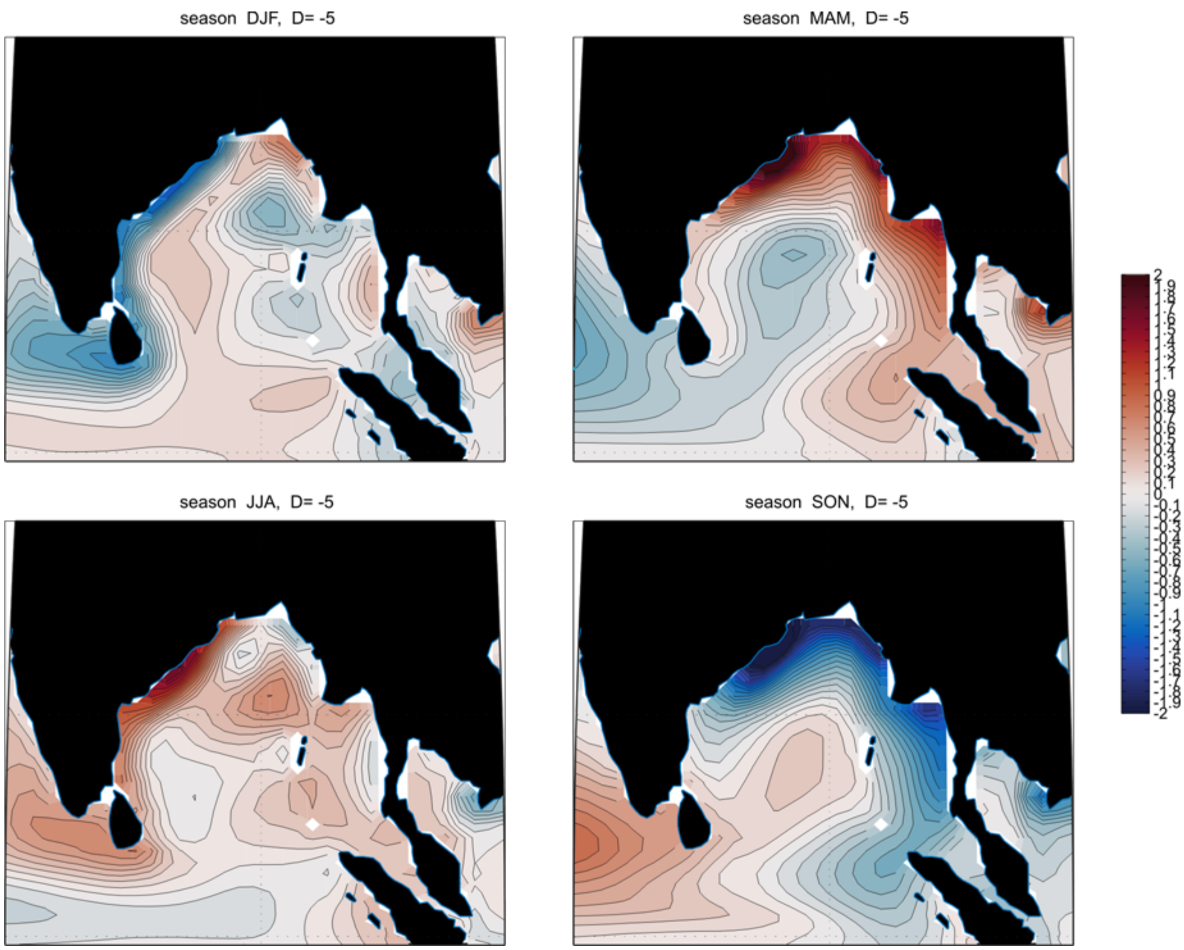

Figure 41: Twenty-year seasonal averages of salinity anomalies at 5m in the Bay of Bengal. September-November. {bayofbengal_s

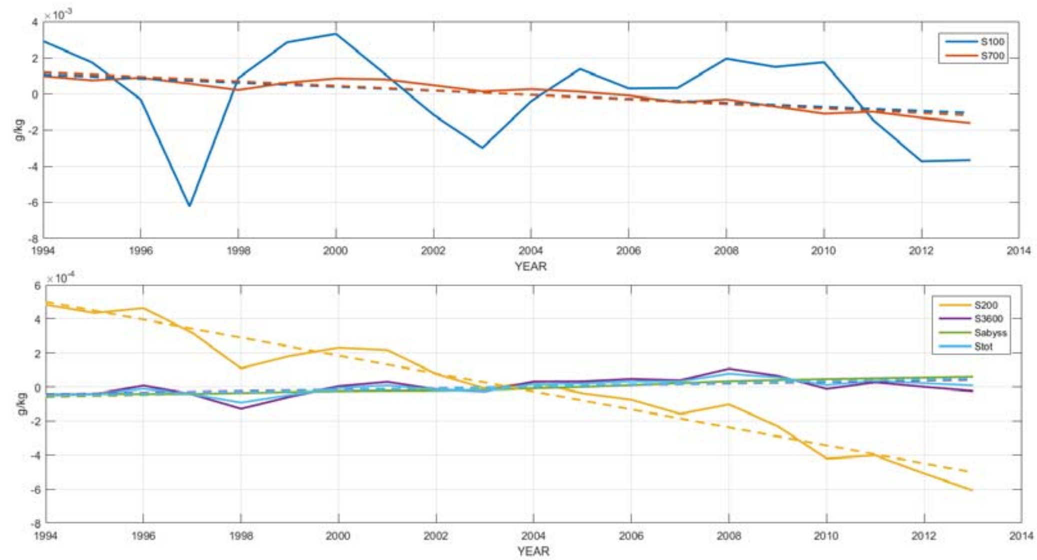

Figure 42: Salinity anomaly by year and depth interval. The upper ocean becomes fresher with a small salinity increase below 3600m corresponding to the slight net warming there and again most likely owing to the adjustment to initial conditions.

{salt_anom_byy

3.2 Fresh Water uptake

Fig. 42 shows the small changes through time occur in the salinity fields, including a weak freshening below 100m but above the abyss. The equivalent freshwater injections are shown in Table 4 as meters of water each year. The net change over 20 years to 2000m corresponds to about 3 mm/y freshwater addition or about 0.04 Sv. (For comparison, net annual precipitation over the ocean is about 12 Sv.) Spatial variations in $\partial\rho/\partial S$ were not included. If justified, more accurate calculations are obviously possible.

3.3 Surface Salinity Change

The difference between the annual mean near-surface (5 M) salinity anomalies in 2013 minus those in 1994 is shown in Fig. 43 and can be compared with the 20-year near-surface mean surface salinity in Fig. 33. Durack et al. (2012) have suggested that the surface salinity patterns over *50* years have become more intense in the last decades. In contrast with their result, the pattern correlation between the time average salinity and the 20-year difference is 0.26. Even if statistically significant (not clear) the mean salinity pattern accounts for less than 10% of of the spatial variation in the change; cf. Vinogradova and Ponte (2016).

Depth Range m	**20 y mean Sal** g/kg	**Salinity Change 20 y** 10^{-3}g/kg	**Freshwater Input** mm/y
0-100	34.74 (7.2)	-6.6	1.2
0-700	34.74 (17.2)	-2.6	3.2
0-2000	34.70 (17.1)	-1.1	3.8
0-3600	34.72 (17.0)	0	-0.1
0-bottom	34.72 (16.7)	0	-0.4
Abyss (3600m-bottom)	34.73 (11.2)	+0.1	-0.1

Table 4: Time-mean salinity in the ocean by depth range, the calculated change over 20 years, and approximate conversion to equivalent freshwater input or extraction. {meansalt}

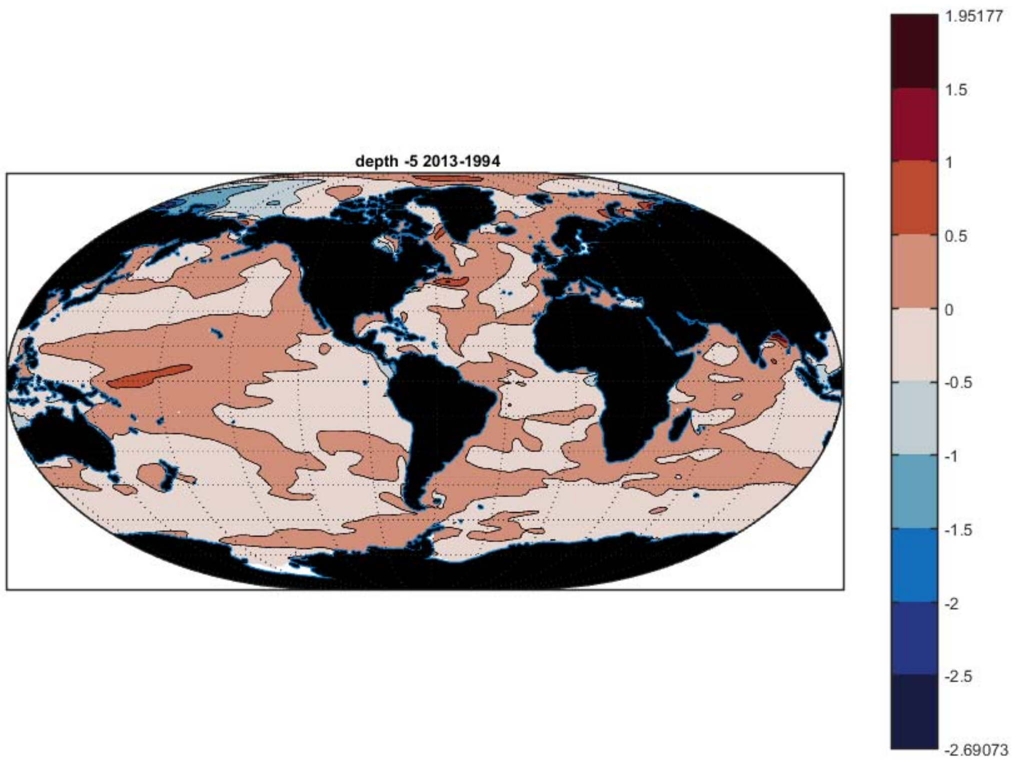

Figure 43: Change in 5m salinity between 1993 and 2014. {salt_5m_2013_

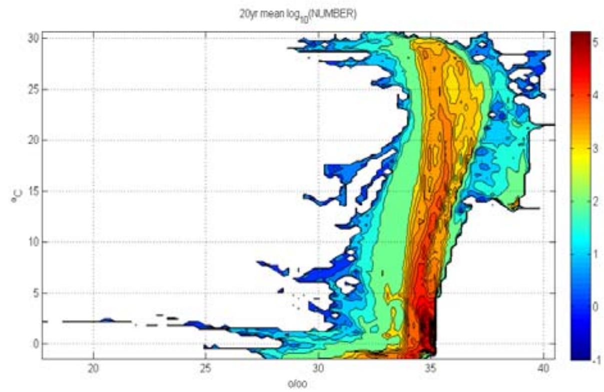

Figure 44: T-S histogram of the raw (not volume weighted) temperatures and salinities in the 20-year mean. The logarithm of the relative volume is plotted. (Cf., Fig. 3 of Wunsch and Heimbach, 2014). {rawts_20yearm

3.4 TS-Distribution

In the 20-year average, the largest volume of water in T-S space (Fig. 44) has a temperature of 0.5°C and a salinity of 34.70 g/kg. Worthington (1981) had estimated the most abundant water in the ocean was in the intervals 1.1-1.2°C, 34.68-34.69 g/kg. Separate histograms for volume weighted temperature and salinity have already been shown above.

4 Surface Elevation and Bottom Pressure

Misfits

Surface elevation, $\eta\,(\theta, \lambda, t)$ relative to an estimated geoid is largely, but not completely, determined by the altimetric data: the state estimate is simultaneously being fit to meteorological forcing, the thermal, salinity and ice fields, and any other data (e.g., gravity and altimeter height changes) that are present. A full determination of cause would depend upon the adjoint sensitivity of η to each of these data sets. The adjoint solution is discussed in Part 3. But because the altimetric records are the only ones nearly uniform and global over the entire 20 years, the 20-year average misfit to the time-varying altimetric measurement of η is shown in Fig. 45. Apart from some isolated outliers that have been suppressed, the misfits are generally within 10cms overall, highest at high latitudes, and showing some residual structures in the tropics. Misfits associated with the moving Kuroshio also appear.

Dynamic Topography

The 20-year mean surface elevation relative to the EGM2008 geoid (the dynamic topography; see Pavlis et al., 2012) is shown in Fig. 46. Quantitative differences exist between this estimate

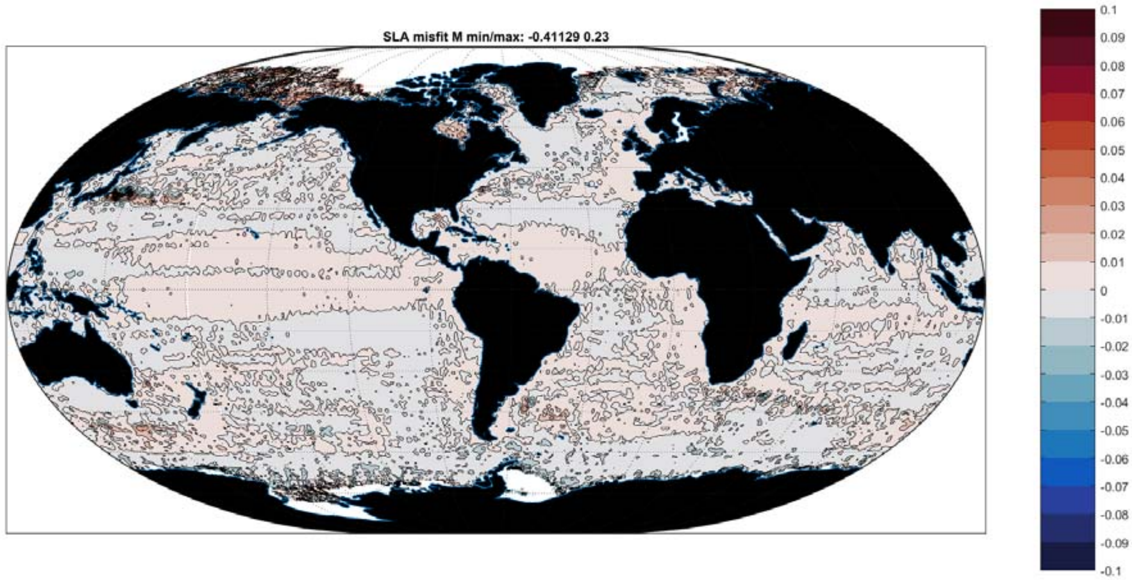

Figure 45: Average misfit (m) over 20 years of the state estimated values of η and that measured by the suite of altimeters. Based upon the average of the monthly misfits. {slamisfit_20y

and the initial estimate from Rio and Hernandez (2004). Maximenko et al. (2009) published similar but different estimates based on various data sets, including surface drifter data corrected for ageostrophic effects; these latter data are not included in ECCO v4 because of concerns over the appropriate error estimates (e.g., Elipot et al., 2016).

Seasonal mean anomalies of η are in Fig. 47-50 and have the expected dominant hemispheric shifts. Some of the large-scale gyres, and particularly the western boundary current regions, as well as the ice-covered regions near Antarctica, show considerable seasonality. Ice-covered regions are difficult to measure whether in situ or by satellite, and high-latitude seasonal biases probably exist in all data sets. The present estimate does include some 200,000 elephant seal profiles (Roquet et al., 2013), many from under the floating ice regions.

The seasonal cycle in η is depicted in Figs. 47-50. Interhemispheric interchange is the major expected feature, but complex structures in the tropics remain even with 20 years of averaging.

Anomalies of η relative to the 20-year average in 1994 and 20 years later are shown in Figs. 51, 52. One can infer a general rise in value over the 20-years, but it is highly structured. Using only tide gauges to determine the global average of figures such as Fig. 51 —to a useful accuracy—is an exercise in finding a small residual in the presence of much larger spatial and temporal fluctuations.

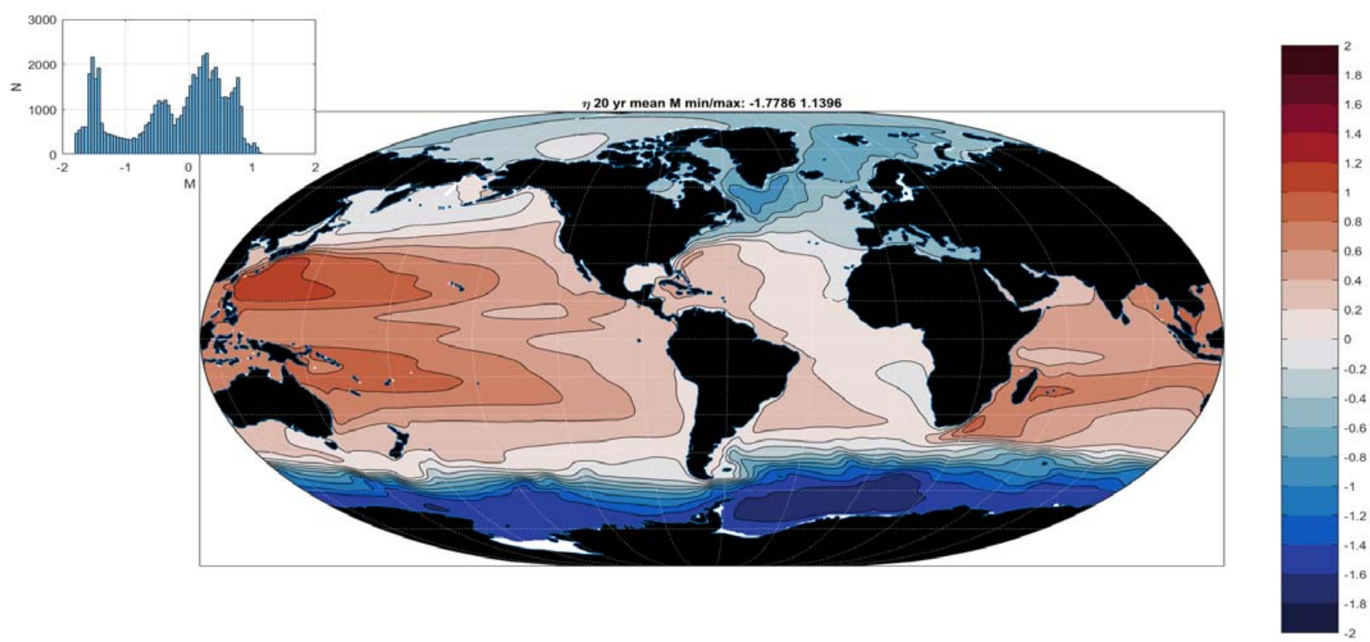

Figure 46: Twenty-year mean dynamic topography . Very low values in the ice-covered areas account separately for the ice thickness. Off-setting the entire surface by a constant would have no observable dynamical consequences. Compare to Maximenko et al. (2009), Knudsen et al. (2011). Inset shows the histogram of values about the mean.

{eta_20yearmea

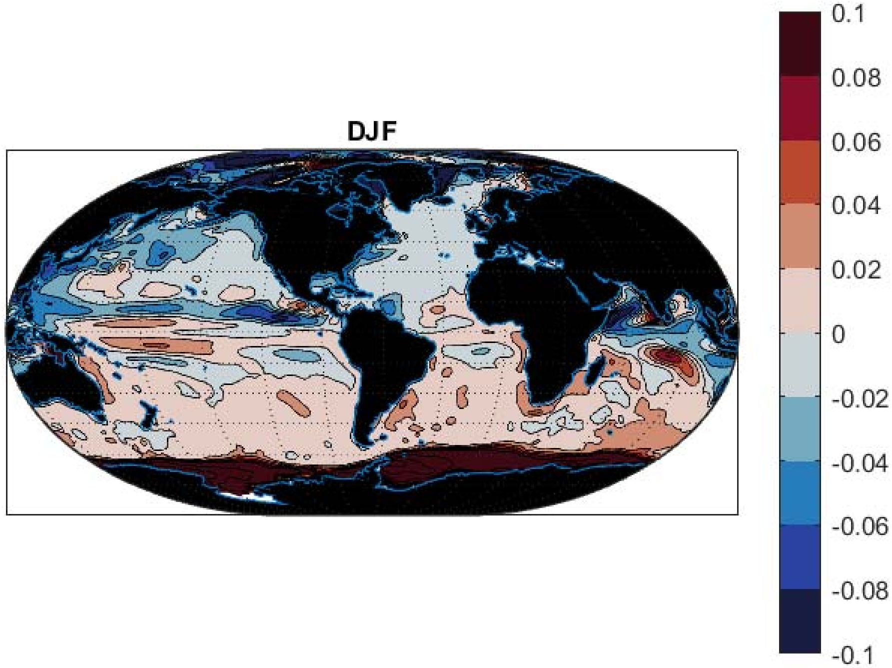

Figure 47: Twenty-year average elevation anomaly in December, January, February. {eta_djf.tif}

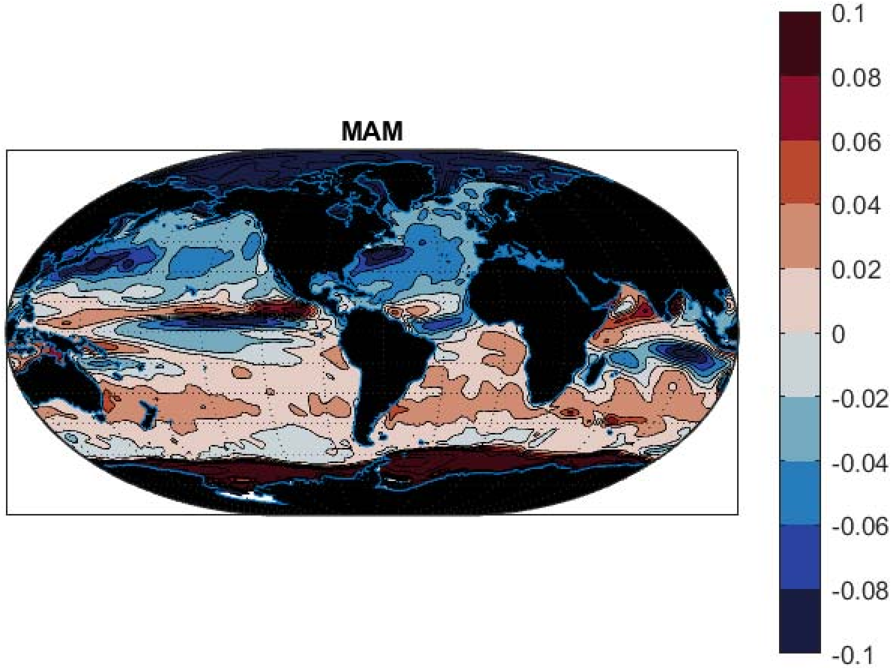

Figure 48: Same as 47 except March, April, May. {eta_mam.tif}

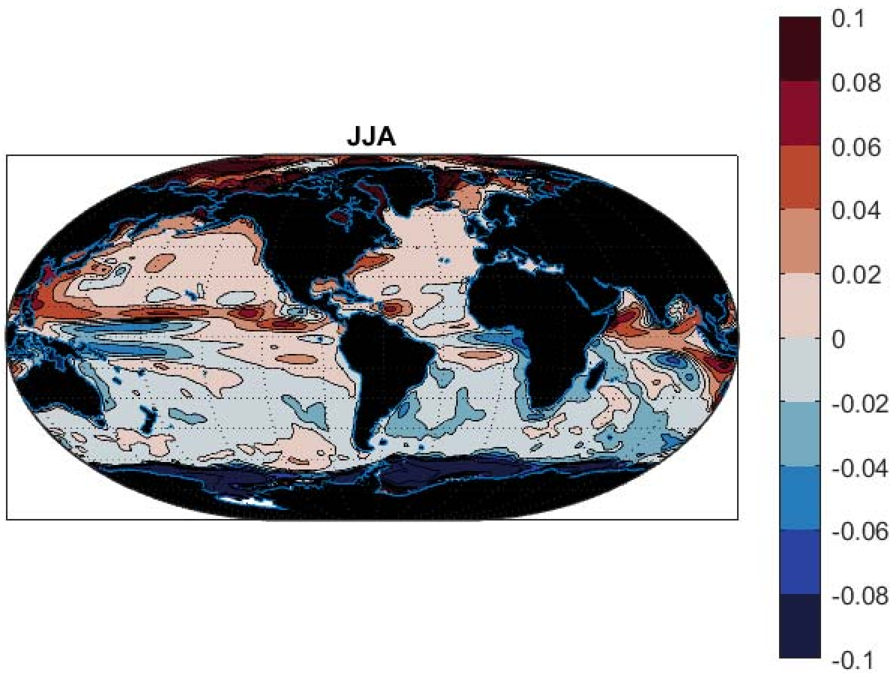

Figure 49: η anomaly, JJA. {eta_jja.tif}

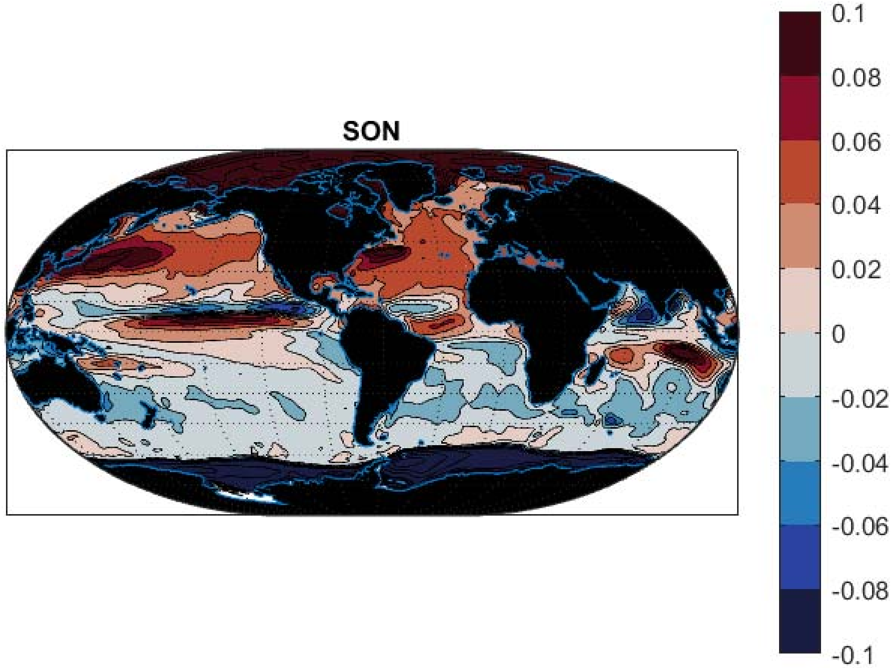

Figure 50: η anomaly September, October, November. {eta_son.tif}

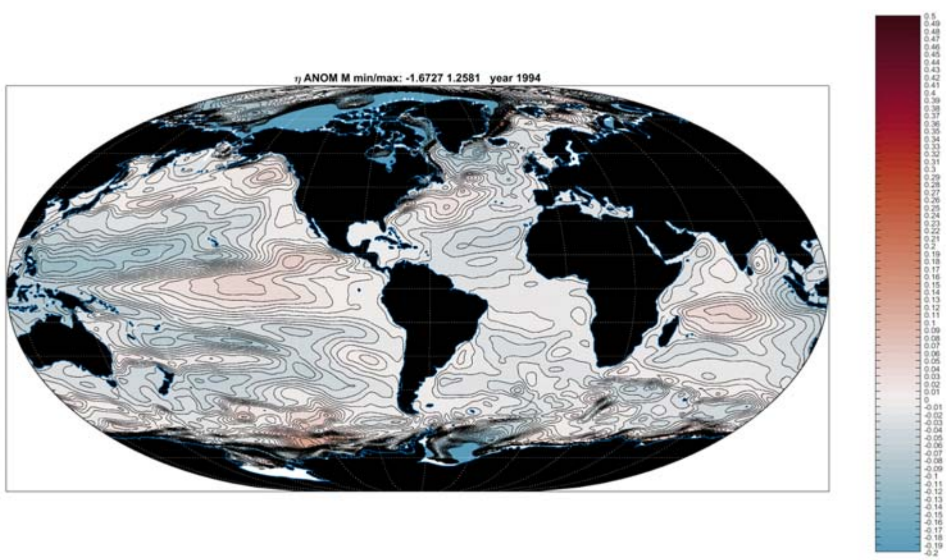

Figure 51: Anomaly (meters) of sea surface elevation η in 1994. Anomalies are relative to the mean in Fig. 46 {eta_anom_1994

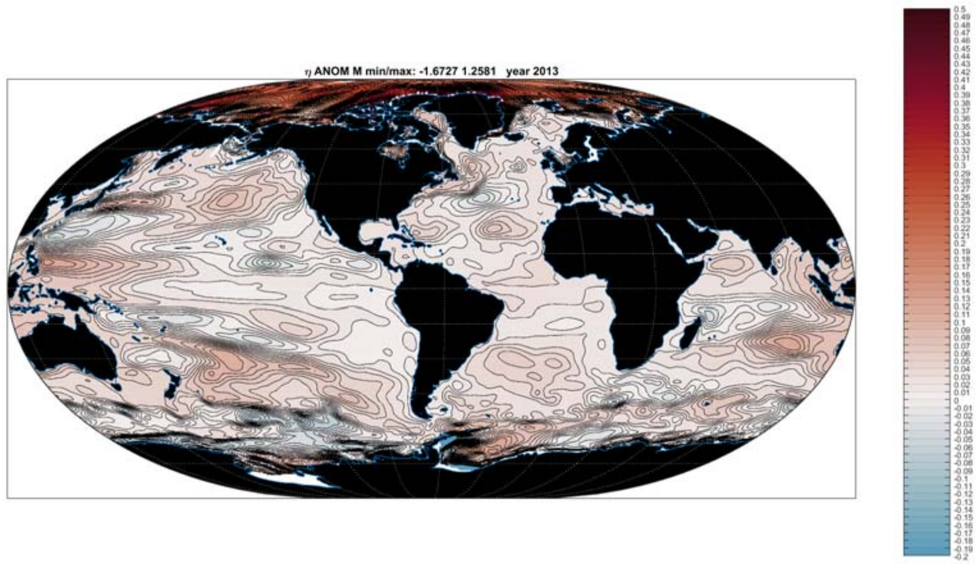

Figure 52: Anomaly of η in 2013. Compare to Fig. 51. {eta_anom_2013

Bottom Pressure

Oceanic bottom pressure, p_b, is of intense interest in the analysis of the GRACE satellite data, in studies of the rotation of the Earth, as well as in the diagnoses of sea level change (see Ponte et al., 2007; Piecuch et al., 2015). Fig. 53 displays the mean seasonal cycle, while Fig. 54 indicates the change from 1994-2013 and can be compared to the estimated linear trend in Fig. 55. The bottom pressure variance represents the residual about the linear trend of the yearly fluctuations. In all cases a spatial mean was removed before plotting, so that total mass change is not reflected in these plots.

5 ENSO and Equatorial Structures

The El Niño-Southern Oscillation (ENSO) component is, apart from the annual cycle, by far the strongest of all short-term (sub-decadal) climatic changes. Entire books have been devoted to its physics (e.g., Philander, 1990 ; Sarachik and Cane, 2010). As examples of its character, Figs. 57- 59 display the elevation and thermal anomaly at 95m and 2000m respectively during 1997-2000.

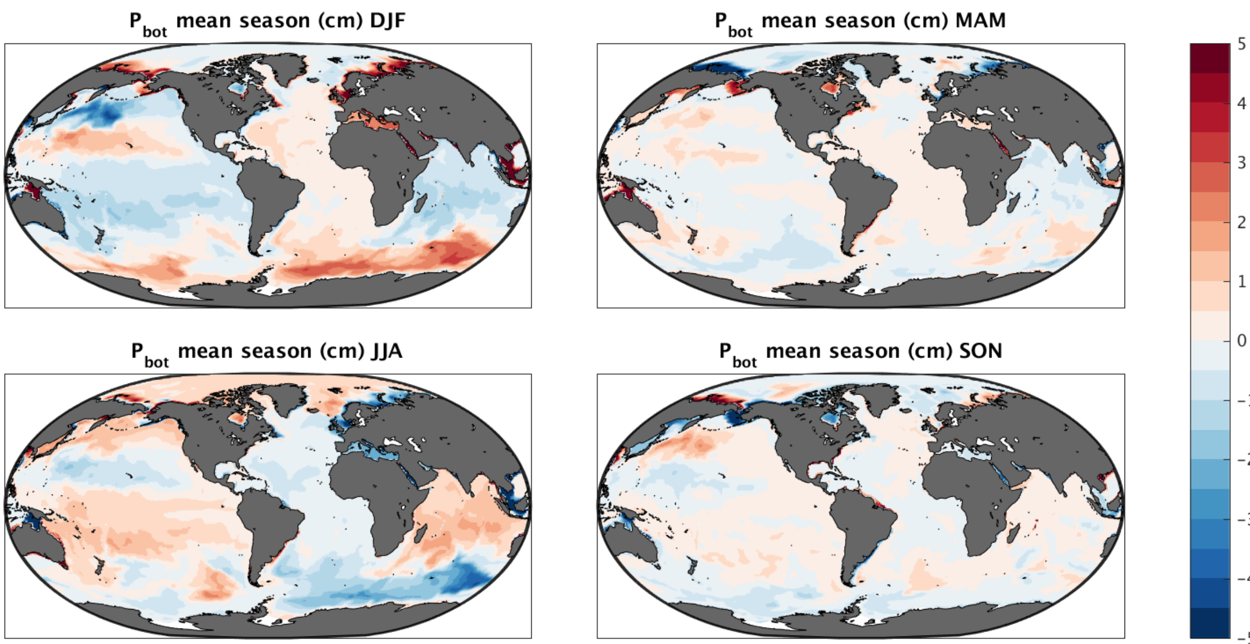

Figure 53: Twenty-year mean seasonal oscillation of bottom pressure anomaly, p_b. {pbot_quinn_cl

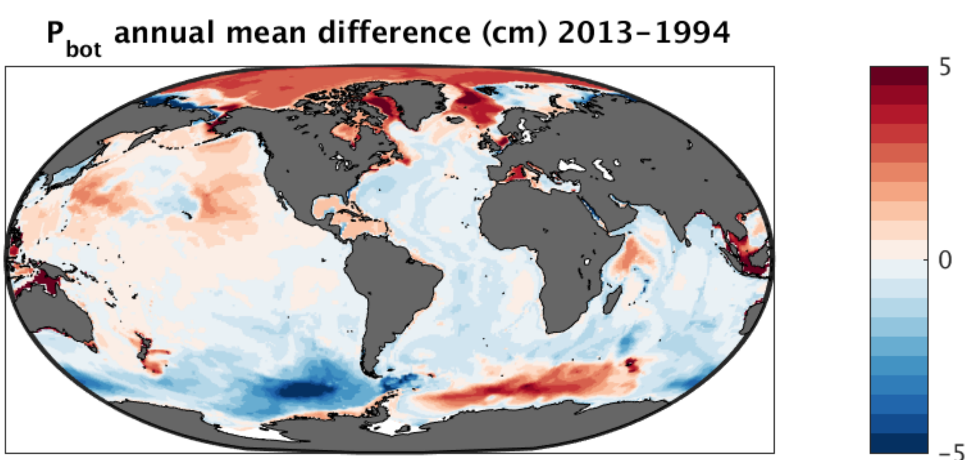

Figure 54: Bottom pressure anomaly in 2013 minus that in 1994. Spatial means removed. {pbot_quinn_cl

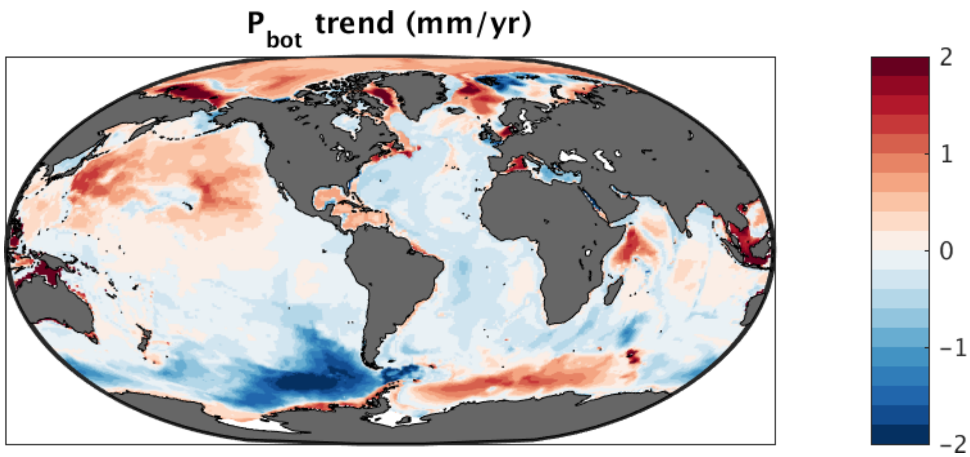

Figure 55: Linear trend (mm/y) in the bottom pressure anomaly. Compare to Fig. 54. {pbot_quinn_cl

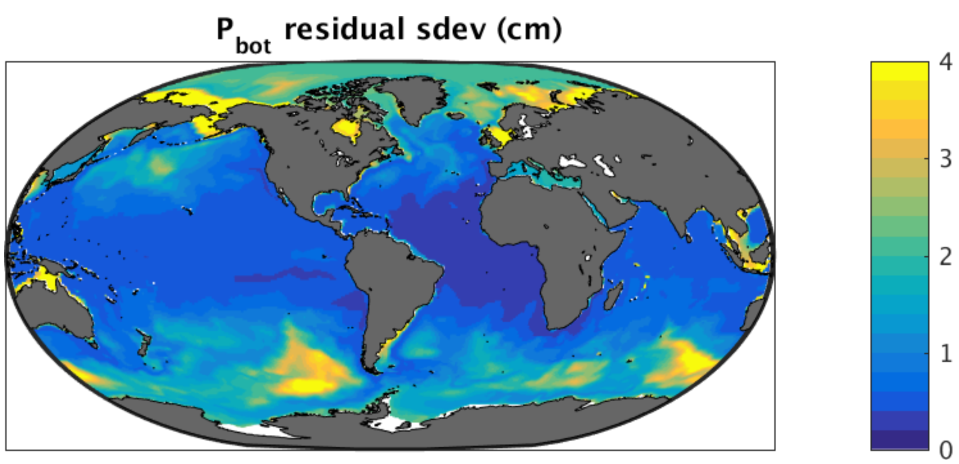

Figure 56: Standard deviation (cm) over 20 years (from annual values) of the residual bottom pressure anomaly (a linear trend estimate was removed). {pbot_quinn_cl

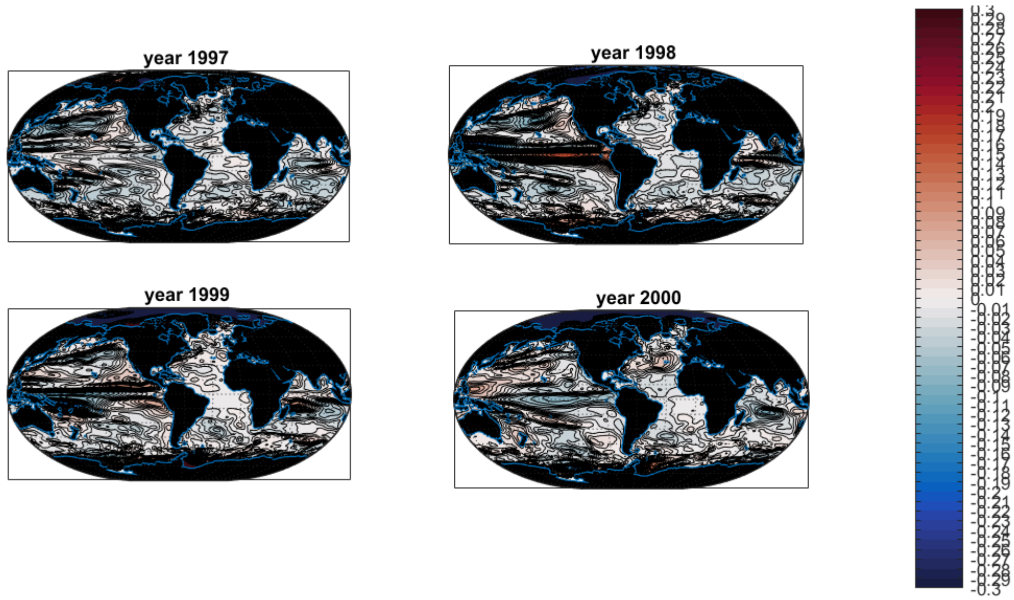

Figure 57: Annual average η (meters) for the years surrounding the 1997-1998 El Niño event. Note the Indian Ocean structure in 1998.

{eta_enso_4yea

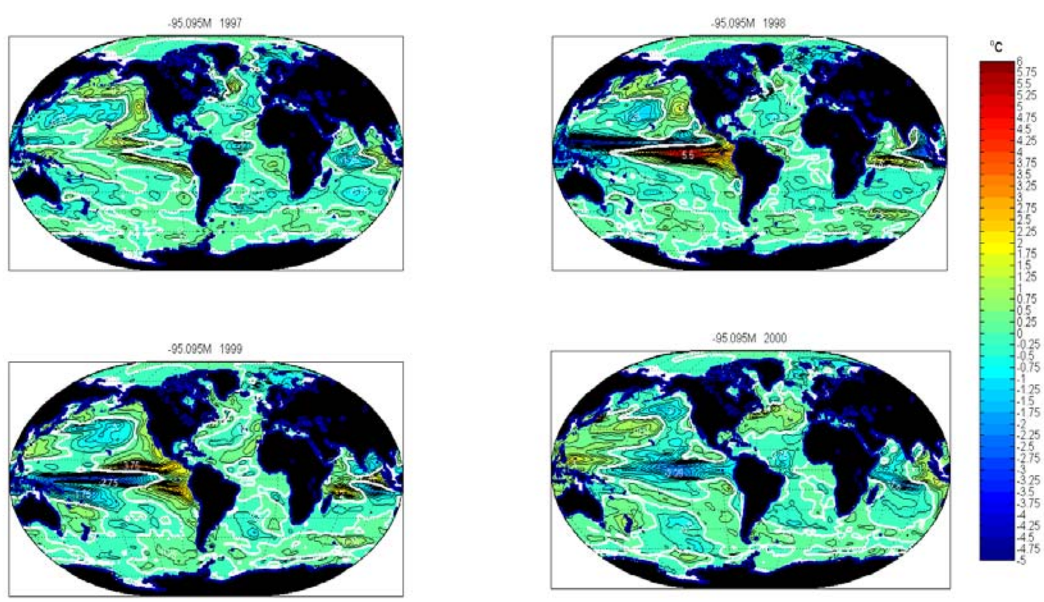

Figure 58: Annual averages at 95m of temperature in the years surrounding the 1997-1998 El Niño event.

{theta_ensoyea

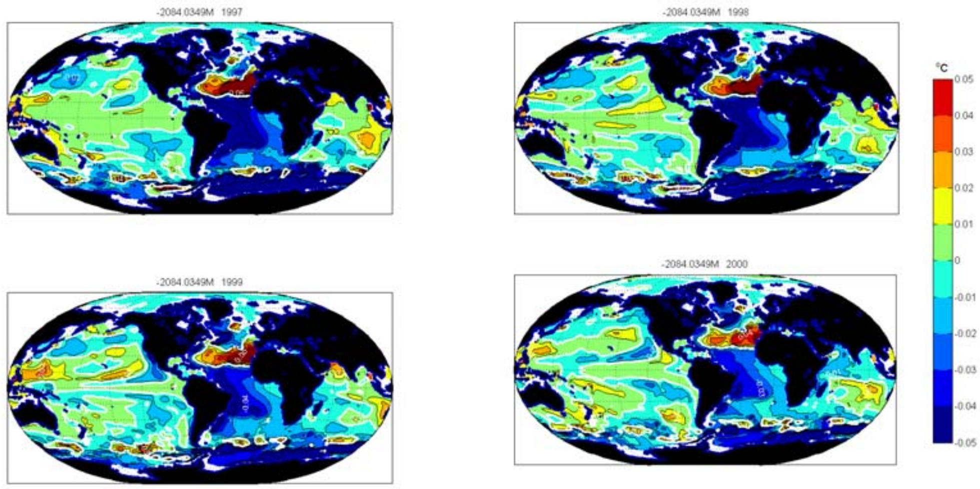

Figure 59: Same as Fig. 58 except at 2000m. {theta_ensoyea

6 Mixed-Layer Depth

The mixed-layer depth Fig. 60 is based upon the density algorithm of Kara et al. (2003) to which comparison may be made. Fig. 61 shows the strong average seasonal response in that depth. Fig. 62 shows the 20-year mean difference in temperature between 5m and 15m and is an indication of the time-average mixed layer vertical gradient.

7 Buoyancy Frequency, Rossby Radii, and Equivalent Depths

An important dynamical consequence of a climatology is encompassed in the buoyancy frequency, $N(\phi, \lambda, z, t)$, the derived baroclinic Rossby radii of deformation R_{Di}, and the related equivalent depths, $h_j^{\prime}$, $j = 1, 2, ...,$ where,

$$R_{Di} = \frac{\sqrt{g h_i^{\prime}}}{f}. \qquad (1)$$ {deformationra

Display of N at 722m can be seen in Fig. 63 and in Wunsch (2013). Here $R_{D1,2}$ are computed from eigenvalues, γ_i, of the Sturm-Liouville problem for the flat-bottom ocean of locally constant physical depth $h(\phi, \lambda)$,

$$\frac{d^2 G_i(z)}{dz^2} + \gamma_i^2 N^2(\phi, \lambda, z) G_i(z) = 0 \qquad (2)$$

with $w(-h) = w(0) = 0$, implying $G_i(-h) = G_i(0) = 0$. (In the interests of efficiency, the full free surface boundary condition was replaced by a rigid lid; see Wunsch, 2013 for full discussion.)

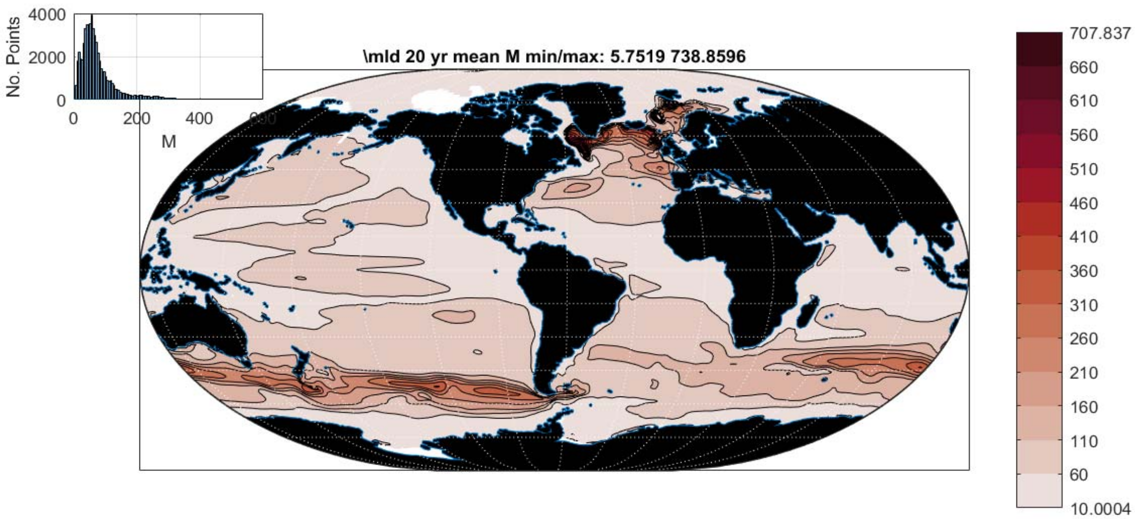

Figure 60: Twenty-year average mixed-layer depth as defined by Kara et al. (2003). Most of the ocean has values near 100m, with extreme values above 700m in the high latitude North Atlantic Ocean. {mixed_layer_2

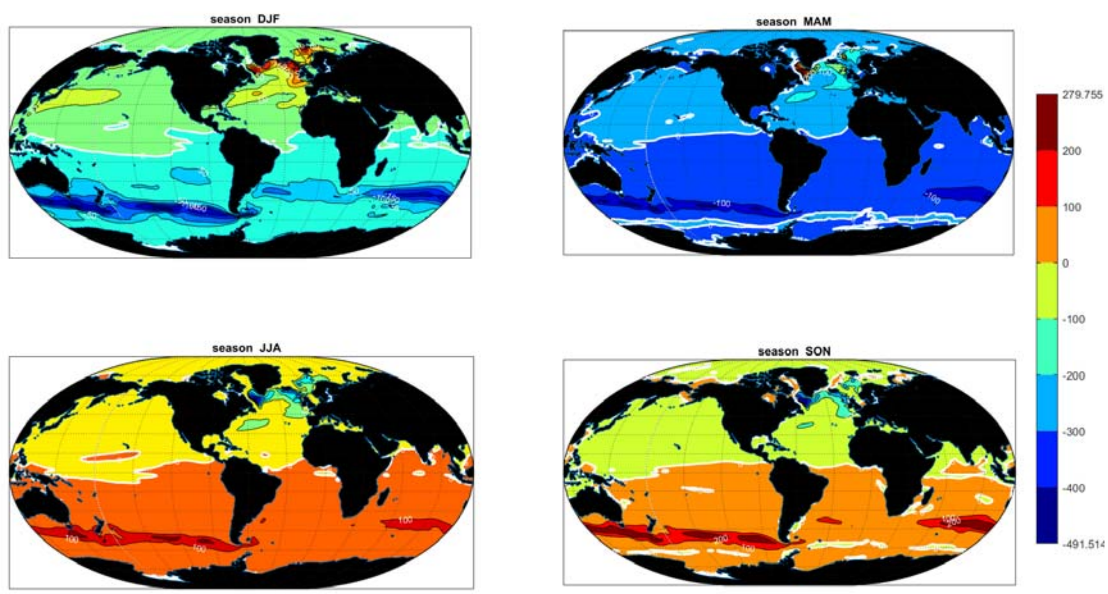

Figure 61: Anomaly of mixed-layer depth as a 20-year seasonal average. Negative values denote a shoaling relative to the mean in Fig. 60. {mixed_layerde

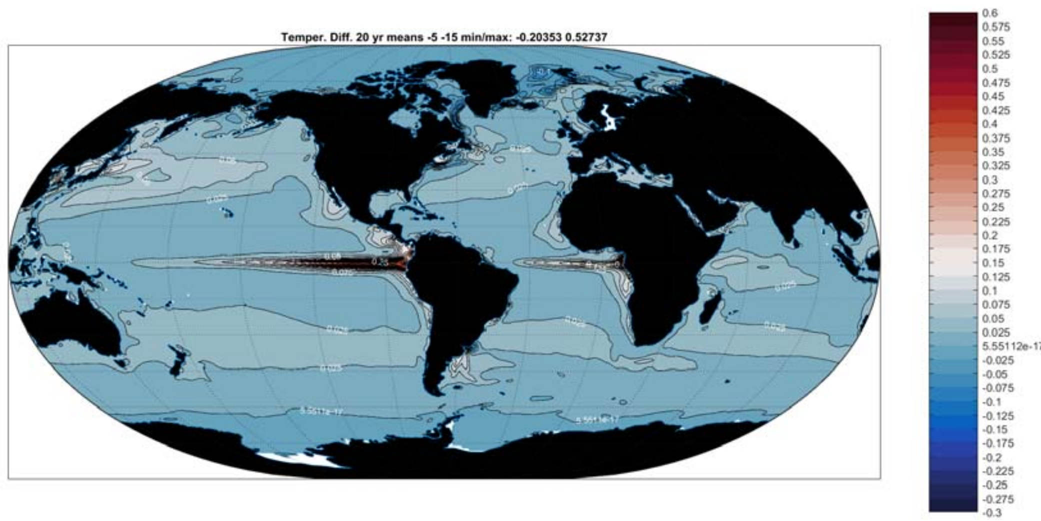

Figure 62: Difference in the temperatures at 5m and 15m as a 20 year mean. The figure is an indication of the near-surface mixed layer thermal gradient (compare Figs. 5, 6).

{temp_20yrmean

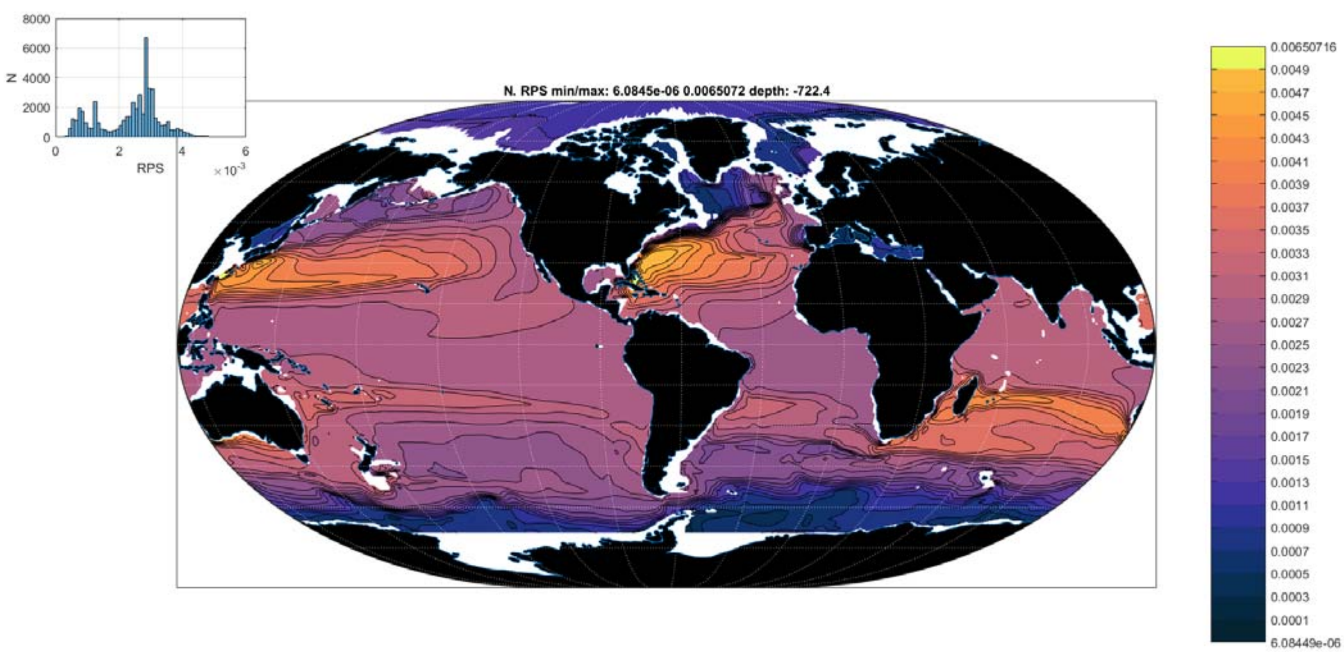

Figure 63: Estimated buoyancy frequency (N) in radians/sec at 722m as computed from the TEOS simplified formula for density and their algorithm. Estimates at other depths can be seen in Wunsch (2013).

{n_20yearavera

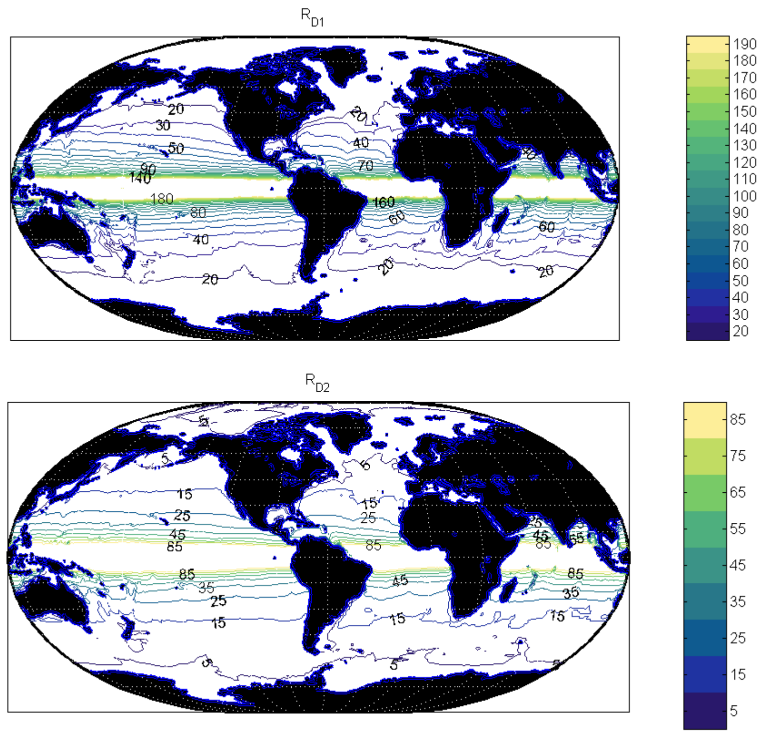

Figure 64: First and second Rossby radii, $R_{D1,2}$ computed from the solution of the rigid lid Sturm-Liouville problem. Contouring near the equatorial singularity is incomplete. {rd1_rd2.tif}

Visually the chart is very similar to the earlier one of Chelton et al. (1998), but with detailed differences presumed to arise from their use of a very different climatology. Values of $G_i(0)$ are important in the interpretation of altimetric data as representing isopycnal disturbances, but the free surface boundary condition is required (which leads to a vertical velocity reversal near to the free surface). The ratio R_{D2}/R_{D1} varies between about 0.31 and 0.79 (not shown) with the smallest values at high latitudes and near the equator. A second mode weights the upper ocean differently than does the first mode and this sensitivity accounts for much of the spatial variation in the ratio. For numerical models trying to obtain realism for second and higher mode vertical structures (three or more levels or layers), resolving this second and higher deformation radius can be a serious problem.

The equivalent depth, h_1' is shown in Fig. 65 and differs in detailed structure from the phase speed values $\sqrt{gh_1'}$ of Chelton et al. (1998) or Rainville and Pinkel (2006).

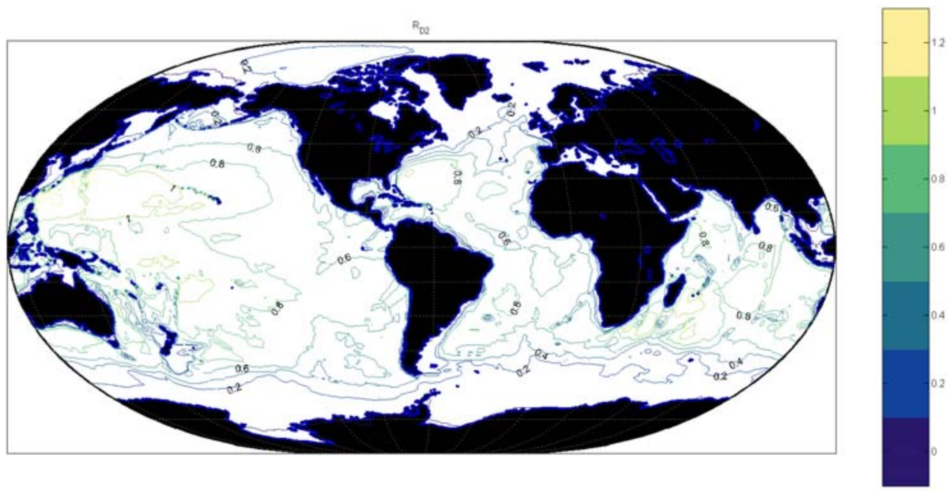

Figure 65: First equivalent depth, h'_1, in meters. The high frequency internal wave gravity phase speed, plotted by other authors (e.g., Chelton et al, 1998; Rainville and Pinkel, 2006) from a different climatology is $\sqrt{gh'_1}$. No equatorial singularity occurs. {h1.tif}

8 Comments

An important qualitative result of the state estimate is the spatial complexity of most variables even after 20 years of averaging (see for example, Figs. 7, 10, 39, 41). The central message must be that global space-time sampling of almost any quantity must be nearly complete—should any accurate average be required. In many variables, such as upper ocean temperature and salinity and mixed layer depth, the strong seasonal cycle must be resolved to determine the interannual changes with useful accuracies.

Further Parts in this series will depict the velocity field and its changes, the meteorological variables and their changes, the heat and salt transports,ice cover, a few regional comparisons, and discussion of the adjoint/dual solution and of the uncertainties.

Acknowledgments

Supported by NASA for the ECCO Consortium at MIT, AER, JPL. We thank all of the people, scientists, engineers, ships' crews, program managers, who finally made possible the gathering of global ocean data, as well as all those who have worked on the ECCO system and models.

References

Abraham JP, Baringer M, Bindoff NL, Boyer T, Cheng LJ, et al. 2013. A review of global ocean temperature observations" implications for ocean heat content estimates and climate change. Rev. Geophys. 51: 450-83

AchutaRao KM, Ishii M, Santer BD, Gleckler PJ, Taylor KE, et al. 2007. Simulated and observed variability in ocean temperature and heat content. Proceedings of the National Academy of Sciences of the United States of America 104: 10768-73

Adcroft A, Hill C, Campin JM, Marshall J, Heimbach P. 2004. Overview of the formulation and numerics of the MIT GCM

Boyer T, Domingues CM, Good SA, Johnson GC, Lyman JM, et al. 2016. Sensitivity of Global Upper-Ocean Heat Content Estimates to Mapping Methods, XBT Bias Corrections, and Baseline Climatologies. Journal of Climate 29: 4817-42

Chaudhuri AH, Ponte RM, Forget G. 2016. Impact of uncertainties in atmospheric boundary conditions on ocean model solutions. Ocean Modelling 100: 96-108

Chaudhuri AH, Ponte RM, Forget G, Heimbach P. 2013. A Comparison of Atmospheric Reanalysis Surface Products over the Ocean and Implications for Uncertainties in Air-Sea Boundary Forcing. Journal of Climate 26: 153-70

Chelton DB, Schlax MG. 1996. Global observations of oceanic Rossby waves. Science 272: 234-38

Colin de Verdière A, Ollitrault M. 2016. A Direct Determination of the World Ocean Barotropic Circulation. Journal of Physical Oceanography 46: 255-73

Dee DP, Balmaseda M, Balsamo G, Engelen R, Simmons AJ, Thépaut JN. 2014. Toward a Consistent Reanalysis of the Climate System. Bulletin of the American Meteorological Society 95: 1235-48

Durack PJ, Wijffels SE, Matear RJ. 2012. Ocean Salinities Reveal Strong Global Water Cycle Intensification During 1950 to 2000. Science 336: 455-58

Elipot S, Lumpkin R, Perez RC, Lilly JM, Early JJ, Sykulski AM. 2016. A global surface drifter data set at hourly resolution. Journal of Geophysical Research: Oceans

Forget G. 2010. Mapping ocean observations in a dynamical framework: A 2004-06 ocean atlas. Journal of Physical Oceanography 40: 1201-21

Forget G, Campin J-M, Heimbach P, Hill C, Ponte R, Wunsch C. 2015. ECCO version 4: an integrated framework for non-linear inverse modeling and global ocean state estimation. Geosci. Model Dev. 8: 3071?104

Forget G, Ponte RM. 2015. The partition of regional sea level variability. Progress in Oceanography 137: 173-95

Fu LL, Haines BJ. 2013. The challenges in long-term altimetry calibration for addressing the problem of global sea level change. Adv. Space Res. 51: 1284-300

Fuglister FC. 1960. Atlantic Ocean Atlas of Temperature and Salinity Profiles and Data from the International Geophysical Year of 1957-1958. 209 pp pp.

Gill AE, Niiler PP. 1973. The theory of the seasonal variability in the ocean. Deep-Sea Res. 20: 141-77

Gouretski VV,. Koltermann, K. P. 2004. WOCE Global Hydrographic Climatology.

Häkkinen S, Rhines PB, Worthen DL. 2013. Northern North Atlantic sea surface height and ocean heat content variability. Journal of Geophysical Research: Oceans 118: 3670-78

Kara AB, Rochford PA, Hurlburt HE. 2003. Mixed layer depth variability over the global ocean. J. Geophys. Res. 108: 3079

Knudsen P, Bingham R, Andersen, O.,Rio, M. H. 2011. A global mean dynamic topography and ocean circulation estimation using a preliminary GOCE gravity model. Journal of Geodesy 85: 861-79

Koltermann KP, Gouretski VV, Jancke K, eds. 2011. Hydrographic Atlas of the World Ocean Circulation Experiment (WOCE). Volume 3: Atlantic Ocean International WOCE Project Office, Southampton, UK, ISBN 090417557X.

Levitus S. 1982. Climatological Atlas of the World Ocean. 173 pp plus microfiche pp.

Liang X, Piecuch CG, Ponte RM, Forget G, Wunsch C, Heimbach P. 2016. Change of the Global Ocean Vertical Heat Transport over 1993-2010. Submitted for publication

Liang X, Wunsch C, Heimbach P, Forget G. 2016. Vertical redistribution of oceanic heat content. J. Clim. 28: 3821-33

Marshall J, A. Adcroft, C. Hill, L. Perelman, Heisey C. 1997. A finite-volume, incompressible Navier Stokes model for studies of the ocean on parallel computers. J. Geophys. Res., 102: 5753-66

Maximenko N, Niiler P, Rio MH, Melnichenko O, Centurioni L, et al. 2009. Mean Dynamic Topography of the Ocean Derived from Satellite and Drifting Buoy Data Using Three Different Techniques. Journal of Atmospheric and Oceanic Technology 26: 1910-19

Pavlis NK, Holmes SA, Kenyon SC, Factor JK. 2012. The development and evaluation of the Earth Gravitational Model 2008 (EGM2008). J. Geophys. Res.-Solid Earth 117

Pillar HR, Heimbach P, Johnson HL, Marshall DP. 2016. Dynamical Attribution of Recent Variability in Atlantic Overturning. Journal of Climate 29: 3339-52

Ponte RM, C. Wunsch, Stammer D. 2007. Spatial mapping of time-variable errors in TOPEX/POSEIDON and Jason-1 seasurface height mesurements. J. Atm. Oc. Tech,, 24: 1078-85

Purkey SG, Johnson GC. 2010. Warming of Global Abyssal and Deep Southern Ocean Waters between the 1990s and 2000s: Contributions to Global Heat and Sea Level Rise Budgets. Journal of Climate 23: 6336-51

Quinn KJ, Ponte RM. 2008. Estimating weights for the use of time-dependent gravity recovery and climate experiment data in constraining ocean models. Journal of Geophysical Research-Oceans 113

Rio MH, Hernandez F. 2004. A mean dynamic topography computed over the world ocean from altimetry, in situ measurements, and a geoid model. Journal of Geophysical Research-Oceans 109

Roquet F, Wunsch C, Forget G, Heimbach P, Guinet C, et al. 2013. Estimates of the Southern Ocean general circulation improved by animal-borne instruments. Geophysical Research Letters 40: 6176-80

Stammer D, Balmaseda M, Heimbach P, K?hl A, Weaver A. 2016. Ocean Data Assimilation in Support of Climate Applications: Status and Perspectives. Annu. Rev. Mar. Sci. 8: 491-518

Stammer D, Wunsch C, Giering R, Eckert C, Heimbach P, et al. 2002. Global ocean circulation during 1992-1997, estimated from ocean observations and a general circulation model. Journal of Geophysical Research-Oceans 107: -

Stommel H, Arons AB. 1960. On the abyssal circulation of the world ocean-I. Stationary planetary flow patterns on a sphere. Deep-Sea Res., 6: 140-54

Talley LD, Feely RA, Sloyan BM, Wanninkhof R, Baringer MO, et al. 2016. Changes in Ocean Heat, Carbon Content, and Ventilation: A Review of the First Decade of GO-SHIP Global Repeat Hydrography In Annual Review of Marine Science, Vol 8, ed. CA Carlson, SJ Giovannoni, pp. 185-215

Vinogradov SV, Ponte RM, Heimbach P, Wunsch C. 2008. The mean seasonal cycle in sea level estimated from a data-constrained general circulation model. Journal of Geophysical Research-Oceans 113

Vinogradova NT, Ponte RM. 2016. In search for fingerprints of t he recent intensification of the ocean water cycle. J. Clim. (submitted)

Vinogradova NT, Ponte RM, Fukumori I, Wang O. 2014. Estimating satellite salinity errors for assimilation of Aquarius and SMOS data into climate models. Journal of Geophysical Research-Oceans 119: 4732-44

Wunsch C. 2016. Global Ocean Integrals and Means, with Trend Implications In Annual Review of Marine Science, Vol 8, ed. CA Carlson, SJ Giovannoni, pp. 1-+

Wunsch C, Heimbach P. 2013. Dynamically and kinematically consistent global ocean circulation state estimates with land and sea ice In Ocean Circulation and Climate, 2nd Edition, ed.

JC G. Siedler, W. J. Gould, S. M. Griffies, Eds., pp. 553-79: Elsevier

Wunsch C, Heimbach P. 2014. Bidecadal thermal changes in the abyssal ocean and the observational challenge. J. Phys. Oc. 44: 2013-30

A Twenty-Year Dynamical Oceanic Climatology: 1994-2013. Part 2: Velocities, Property Transports, Meteorological Variables, Mixing Coefficients

The ECCO Consortium (M. Buckley[8], J.-M. Campin[3], A. Chaudhuri[1], I. Fenty[2], G. Forget[3], I. Fukumori[2], P. Heimbach[3,4], C. Hill[3], C.King[3], X. Liang[5], A. Nguyen,[4] C. Piecuch[1], R. Ponte[1], K. Quinn[1], M. Sonnewald[3], D. Spiegel[3], N. Vinogradova[7], O. Wang[2], C. Wunsch[3,6])[†]

June 13, 2017

Abstract

The World Ocean Circulation Experiment (WOCE) was created to produce the first truly climatologically useful picture of the ocean circulation and its variability. This goal is addressed here from the state estimate of the Estimating the Circulation and Climate of the Ocean (ECCO) consortium, which uses almost all of the data obtained during WOCE and its aftermath along with the much improved general circulation modeling capabilities. A dynamically and data-consistent, state estimate is available depicting the ocean and its ice-cover over a 24-year time-span, globally, from the sea surface to the sea floor. The resulting time-dependent 20-year long climatology includes temperature, salinity, surface elevation, bottom pressure, sea-ice, and three components of velocity. Accompanying the state estimate are modified estimates of meteorological forcing-fields, ocean interior mixing coefficients, and initial conditions. Much spatial structure persists through the two-decade averaging. Results here are primarily pictorial in nature, intended to give the wider community a sense of what is now available and useful and where more detailed analysis would be fruitful. An extended reference list is included.

[*]For corrections, additions, comments and criticisms please email carl.wunsch@gmail.com.

[†]1. AER, Inc., 2. Jet Propulsion Laboratory, 3. MIT, 4. U. Texas Austin, 5. U. South Florida, 6. Harvard U., 7. Cambridge Climate Institute, 8. George Mason U.

1 Introduction: The State Estimate (Mostly Repeated from Introduction to Part 1)

Purpose

One of the central goals of the World Ocean Circulation Experiment (WOCE) was to produce the first truly global time-varying estimate of the circulation over approximately a decade, an estimate that would be useful in defining the major climatologically important ocean elements. The Estimating the Circulation and Climate of the Ocean (ECCO) project was formed near the start of the WOCE field program so as to address this goal using both the conventional and newly-deploying WOCE observation system, along with the rapidly advancing general circulation modelling capability (Stammer et al., 2002). In this paper, and in subsequent Parts, this WOCE goal is addressed by defining a time-dependent climatology over the 20-year (bidecadal) interval 1994-2013. Little or no dynamical or kinematical interpretation is provided—that is left to other authors and times.

Various oceanic climatologies are in use by the oceanographic and climate dynamics communities. They serve as tests of models, as initial conditions, and as a basic descriptor of the ocean. Definitions of climatologies vary widely both in terms of how they were formed and the durations they represent. Here we describe a 20-year average modern climatology from a dynamically consistent model that also has a consistent fit to the majority of global data between 1992 and 2015 (Wunsch and Heimbach, 2013; Fukumori et al., 2017). The climatology is based upon the ECCO version 4 state estimate (Forget et al., 2015). It derives from a least-squares fit of the evolving MITgcm (Marshall et al., 1997; Adcroft et al., 2004; Forget et al., 2015) to the numerous and diverse global observations. A summary would be that all of the Argo, altimetry, the CTD hydrography appearing in the WOCE Climatology and successors (Gouretski and Koltermann, 2004; Talley et al., 2016), all extant, bias error-corrected XBTs, the considerable elephant seal profile data (Roquet et al., 2013), GRACE mission mean and time-dependent geoids, satellite-measured sea surface temperature and salinity, and the ECMWF[1] ERA-interim reanalysis of the meteorological variables (Dee et al., 2011, 2014), have been included, with the fits inferred to be adequate relative to the estimated uncertainties of the data. (Atmospheric reanalyses should not be considered "data", however.)

Previous climatologies, e.g. Levitus et al. (1982) and its later incarnations as the NOAA World Ocean Atlas, or Gouretski and Koltermann (2004) have usually been based only upon temperature and salinity averages and over much longer time intervals than employed here. Other climatologies (e.g., AchutaRao et al., 2007) have focussed on the upper 700 or 1000m

[1] European Centre for Medium Range Weather Forecasts

and relied heavily on XBT measurements. Ishii et al. (2005) is a climatology of the sea surface temperature. As such, all these suffer from the very great inhomogeneities of data distribution prior to the WOCE period and a series of untestable statistical hypotheses (see e.g., Kennedy et al., 2011; Wunsch, 2016; Boyer et al., 2016). This present climatology differs from earlier ones most obviously in its production of the three-dimensional, time-varying, three components of velocity and of a self-consistent surface meteorology, as determined at the model time-step, $\Delta t \approx 1$ h. Use of *any* fluid climatology confronts one basic problem: that the resulting time or space-time average fields do not satisfy any simply derivable equations of motion—requiring a variety of turbulence closure schemes—and the relationships among the different variables can be complicated and poorly known. Here, time/space means of fluid quantities are based upon the uniform average of fields exactly satisfying the model equations at each model time-step (at present, 1 hour) and grid-point. Some authors have used ocean general circulation models fit to data in methods analogous to those in meteorology and commonly known as "reanalyses." These, unfortunately, are usually not property conserving (heat, salt, momentum, etc.) and thus unsuitable for global-scale climate calculations (see e.g., Wunsch and Heimbach, 2013; and Fig. 1 of Stammer et al., 2016).

Some sketches of global-scale analyses of earlier multi-decadal ECCO estimates have been published starting with Stammer et al. (2002). Among them, an earlier 16-year global time-average was described by Wunsch (2011), with a focus on the accuracy of Sverdrup balance, and Wunsch and Heimbach (2014) discussed the heat content changes. Liang et al. (2015, 2017) describe the vertical redistribution of heat and Forget and Ponte (2015) the regional sea level changes. Forget (2010) presented an 18-month estimate from an earlier ECCO state estimate. In general, the present solution differs only subtly from those previously used, with the chief differences being ascribed to the inclusion of more data over a longer duration, inclusion of geothermal heating (see Piecuch et al. 2015), improvements in the handling of sea ice, and where appropriate, separate uncertainties for time-average and time-anomaly measurements. Solutions are generally robust, as much of the volume of ocean in the model state vector is in near-geostrophic balance with the density field at all times longer than a few days.

By choosing the period following 1992, a much more nearly uniform global data coverage is obtained than was possible earlier. Chief among the remaining data inhomogeneities are the intensification of the Argo float profile data availability after about 2005.

Any temporally averaged state will be considerably smoother than states which are sampled more or less as "snapshots." Thus classical ship-borne hydrographic sections (e.g., Fuglister, 1960 or the various WOCE Atlases) show many small-scale features which vanish on averaging. Suppressed features include internal waves, tides, and geostrophically balanced eddy motions.

Meandering currents, such as the off-shore Gulf Stream, are broader and smoother than in any near-synoptic estimate. In addition, fluid regions that are only marginally or poorly resolved numerically (particularly boundary currents), will be smoother than even a true 20-year average would be. Nonetheless, even a 20-year average leaves remarkably many structures much smaller than the basin-scale in the estimated circulation.

No model with a nominal horizontal grid-spacing of 1° of longitude can resolve small-scale circulation features, which include the important boundary currents. Nonetheless, the near-geostrophy of the bulk of the ocean supports the conjecture that to the extent that a successful fit to the interior temperature, salinity, and altimetric fields and surface boundary conditions, has been obtained, the boundary currents will be forced by the interior flows to carry the appropriate amount of mass (volume), temperature, etc. so as to satisfy the basic overall conservation laws. This conjecture, upon which we rely, but which is tested elsewhere, can be regarded as a re-statement of that used by Stommel and Arons (1960) in their discussion of deep boundary currents—whose existence and structure was fixed by the mass and property requirements of the interior flow—even though they were not dynamically resolved.

As with any estimation problem, a crucial element in the determination of the best values lies with the use of realistic error estimates for *all* of the data that are being fit. For a full discussion of the error estimate used here, reference must be made to the literature. Temperature measurements are described by Forget and Wunsch (2007) and Abraham et al. (2013). Altimetry accuracies are discussed by Fu and Haines (2013) and Forget and Ponte (2015). For the gravity data from the GRACE mission, see Quinn and Ponte (2008). Satellite surface salinities are addressed by Vinogradova et al. (2014). Meteorological variable accuracies are described e.g., by Chaudhuri et al. (2014, 2016).

This paper is *not* an in-depth analysis of *any* features of the global ocean circulation. It is instead mainly visually descriptive—a suggestive pictorial subsample—intended primarily to serve as an invitation to the wider community to exploit it by demonstrating various products. With the widespread recognition that a steady-state ocean never exists, attention turns instead to the temporal changes over the estimation period. Here for descriptive purposes, a few pictures of changes year-by-year for 20 years, by 20-year averages for each month, and by season, are displayed. All results can readily be calculated month-by-month at the expense of using a larger volume of numbers.

Results here are intended mainly to be indicative of possibilities and an invitation to use, rather than being the most precise or accurate possible. Thus for example, the heat capacity, c_p and the mean density, $\bar{\rho}$ are treated as constant in calculations of heat uptake even though both are (weak) functions of position.

The State Estimate

The ECCO state estimate is obtained from the *free-running* MITgcm after the adjustment of the control parameters required to fit the data. In the least-squares methodology with Lagrange multipliers (see Wunsch and Heimbach, 2013), the entire interval 1992-2015 has been fit to the data. Parameters adjusted include the three-dimensional, top-to-bottom, initial conditions, internal mixing coefficients, and the surface meteorology. At any given time in the estimation interval, the solution represents data both preceding and *following* that date so that the equations are always satisfied while coming as close to the data as possible within uncertainty estimates. The 20-year period 1994-2013 has been chosen for averaging as sufficiently distant from the poorly constrained earlier years before the high accuracy altimetry begins in late 1992 and the time of the then non-existent data following 2016. The period corresponds to that of complete coverage by satellite altimetry, the WOCE CTD survey, and the interval after about 2005 when the Argo array became fully-deployed. All data, plus the ECMWF estimate, have been assigned uncertainties that include both instrumental and natural noise. After adjustment of the parameters, the state estimates are the solution to a forward model satisfying all basic conservation requirements. Structurally, it is no different from any other unconstrained model estimate except that its residual data misfits are fully known.

No state estimate is definitive or "correct"; they are "best-estimates" for the present time: data are continuously added, both from more recent years and previously omitted earlier values; estimated data errors are sometimes revised; models are improved; and in all situations, minimizing iterations are ongoing. Values shown here are obtained from ECCO version 4 as of mid-November 2016.

Undoubtedly the state estimate has residual systematic errors at some level, particularly in data-poor regions and times. To some extent, these will be removed when considering only temporal changes in the state over the 20-years and these latter are given some emphasis. Uncertainty estimates remain an amorphous problem: much of the variability in the model represents deterministically evolving elements. Stochastic elements are introduced by weather, some longer-period meteorological variability, and by elements of the initial-conditions best regarded as random. Because the true probability distributions are not known, discussion of estimate uncertainties is postponed to an intended Part 4.

A full description of the many features of the 20-year global ocean circulation requires a book-length publication, if not a library. The strategy here is to sketch the gross hydrographic and circulation features and to do a limited comparison to a few of the special regions (boundary currents, mixed-layer, etc.) to provide some of the flavor of the differences between a moderate-duration, nearly homogeneous, average and both the more common limited-time analyses usually available (classical synoptic hydrographic sections), as well as the far more data-inhomogeneous published climatologies.

With time-mean fields being spatially and temporally smoother than in nominally synoptic measurements, second order quantities such as the time averages e.g., $\langle \mathbf{v} \rangle \langle T \rangle \neq \langle \mathbf{v}T \rangle$, where $\langle \cdot \rangle$ denotes a space-time average, and the difference between them may be very large. Much of physical oceanography has been based upon the unstated assumption that quasi-synoptic measurements represented the mean motion. Thus e.g., the calculation of Sverdrup balance, or of "abyssal recipes", are implicitly steady-state results, despite the common use of individual hydrographic stations or sections. Here true 20-year average estimates are now possible. This description and discussion thus largely focusses on the properties of single variables, T, u, etc., their 20-year means and estimates of the deviation from those means. As Part 2, this paper describes the three dimensional Eulerian velocity field and the estimated (that is, adjusted) meteorological forcing. The hydrographic fields and related properties are discussed in Part 1. Most emphasis is placed on the global fields. A number of higher resolution, regional versions, of the state estimate exist (e.g., Gebbie et al., 2006; Mazloff et al., 2010), and a high northern latitude version is forthcoming (An Nguyen, in preparation, 2017), but these estimates are not further discussed here.

All of the ECCO system output described here is available in Matlab® form at: http://mit.ecco-group.org/opendap/diana/h8_i48/contents.html/[2] as 20-year means, 20-separate annual means, 20-year average individual months, and 20-year average seasonal means (DJF, MAM, JJA, SON) on a grid in 50 vertical levels, of thickness plotted in Fig. 1. Many studies are best done in isopycnal-like coordinate systems; but the present description is confined to calculations in geometrical (latitude-longitude-depth) coordinates, with the interpolations to isopycnals postponed (but see Speer and Forget, 2013 for a mode water discussion).

2 Eulerian Horizontal Velocities

Misfits

As described in Part 1 (ECCO Consortium, 2017), a misfit can be computed between the state estimate and any particular data type. Here, Fig. 3 displays the misfit to some of the TOGA-TAO equatorial current meter array data (Hayes et al., 1991) annual means to the state estimate. Note that in this case, the data were *not* used as constraints on the state estimate, and are thus a completely independent test. At shallower depths (not shown), the consistency between the two estimates is even better.

[2] Or contact Carl Wunsch directly (cwunsch@mit.edu) for data or advice.

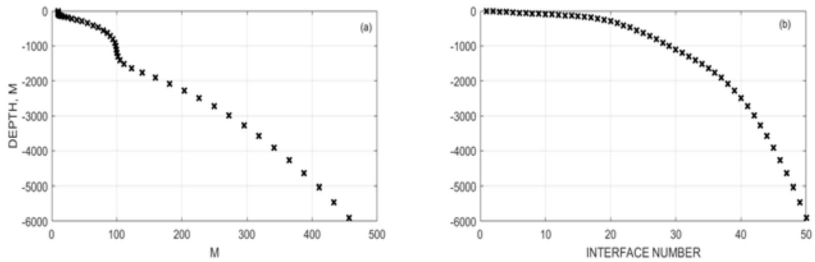

Figure 1: (a) Level thicknesses; (b) level depths in the ECCO version 4 of the MITgcm. {interfaces_la

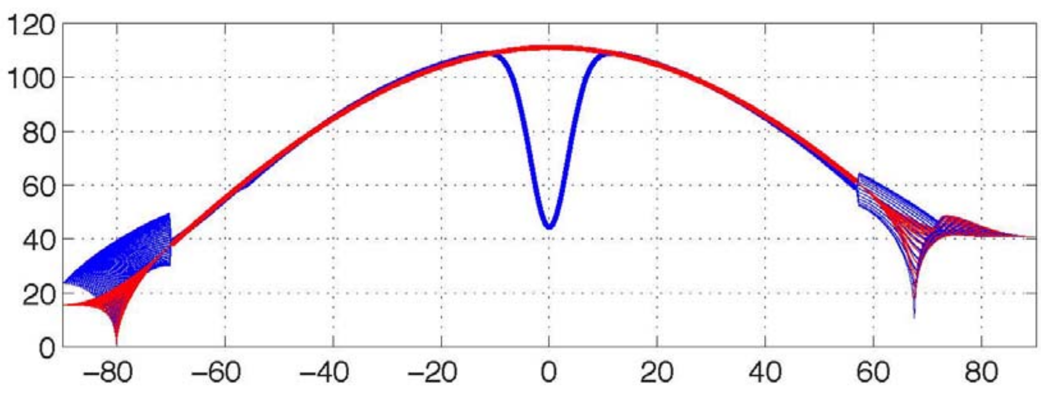

Figure 2: Latitude (blue curve) and longitude spacing in kilometers as a function of latitude (from Forget et al., 2015). Higher latitude spacing exists near the equator. At high latitudes the more complex grid leads to a distribution of spacings (see Figs. 1, 2 of Forget et al., 2015). Most of the high latitude southern region is land. {fig03-eccov4_

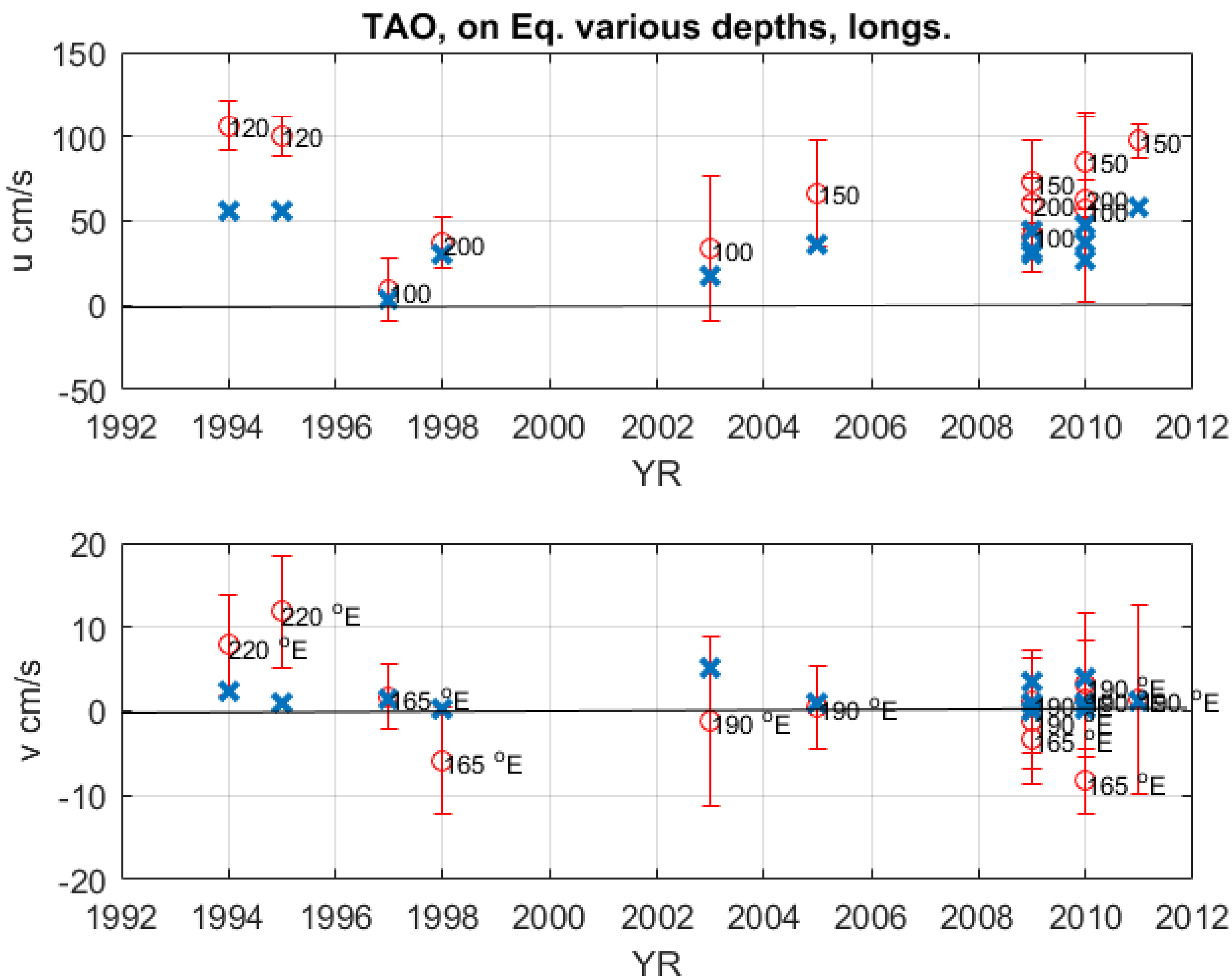

Figure 3: Upper panel shows the u component from the TAO array on the equator at various depths (red symbols) with standard errors. $'\times'$denotes the corresponding ECCO state estimate annual mean. Values are within one standard error. Labels are the water depth. Lower panel shows the same result for the v component. Now the labels indicate the longitude of the measurement.

{tao_annmeans_

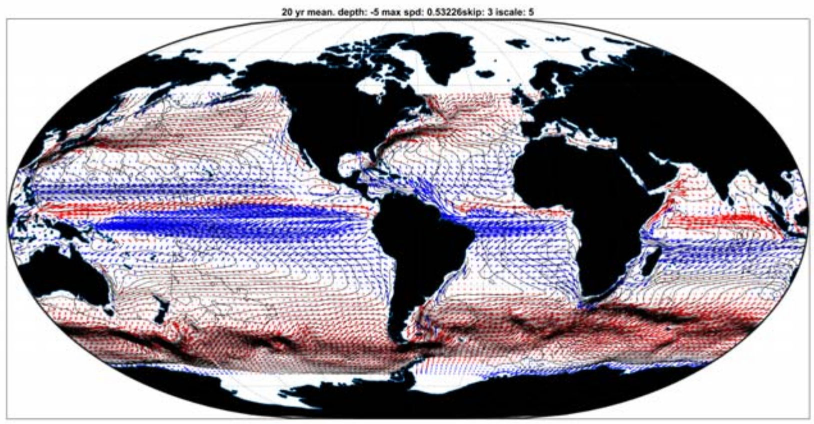

Figure 4: The 20-year average Eulerian flow at 5m depth superimposed upon the time-mean surface elevation, η. Red arrows have an eastward component, blue a westward one. Largest value here (longest arrow) correspond to 40cm/s. In the centers of gyres, particularly, the ageostrophic component of flow visually crosses the surfaces of constant elevation.

{quiver_map_5m

Time Means

Figs. 4-8 depict the 20-year Eulerian mean flow fields as arrow plots at four depths. A number of distinct, expected features can be seen. These include the strongly divergent (to north and south) flows on the equator, the western boundary currents and their extensions as well as the Antarctic Circumpolar Current. All of these flows are broader and smoother than is familiar from attempts at instantaneous depictions. The corresponding pressure field contours are also shown as a visual guide.

The time average zonal flow on the equator is displayed in Fig. 9 with a conspicuous equatorial undercurrent; and the average meridional flow across the equator is in Fig. 10. Time average zonal flow in the Drake Passage is shown in Fig. 11 with a net transport of 146Sv, close to most published values (Meredith et al., 2011), but in contrast to the much larger transport claimed by Donohue et al. (2016), the difference probably owing to the strong assumptions made there. The estimated value here is necessarily consistent with the near-geostrophic interior flows both to the west and east of the passage. Mild annual variations in the transport are depicted below. Fig. 12 shows the remarkably complex meridional mean flow at 60°S, a latitude passing through the Drake Passage.

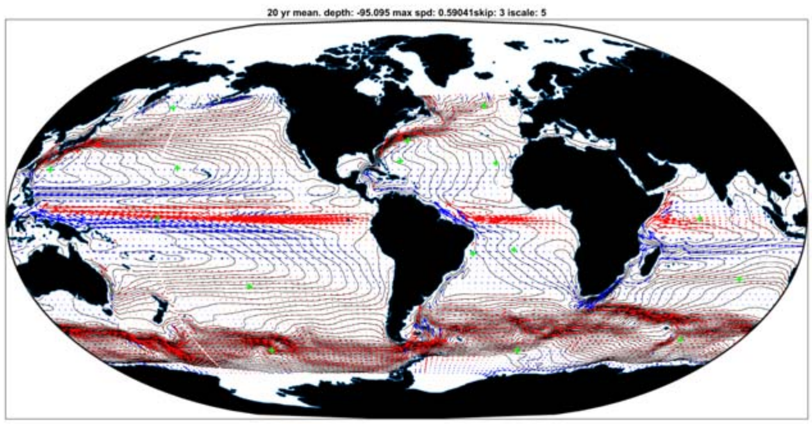

Figure 5: Twenty-year average of the mean horizontal flow at 95m superimposed on the time-mean sea surface elevation. Largest value is 59 cm/s. Vectors more closely follow the elevation lines than does the velocity at 5m in Fig. 4. Note the strong eastward flow on the equator as compared to the near-surface values. {quiver_map_10

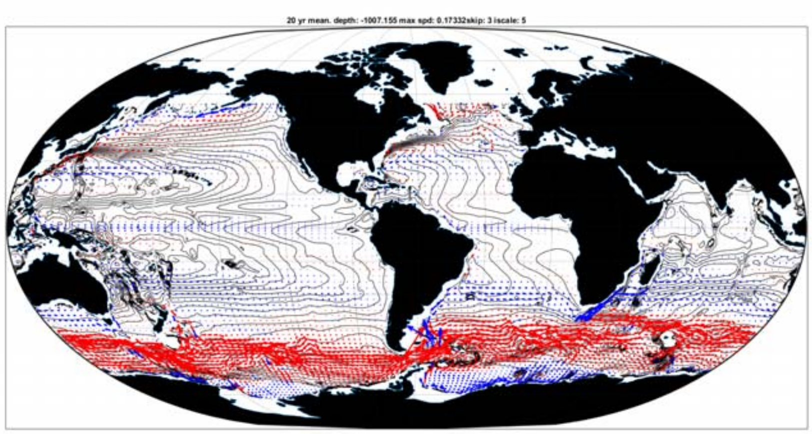

Figure 6: Twenty-year mean flow at 1000m (compare Ollitrault and Colin de Verdiere, 2014). Largest value shown is 17 cm/s, but arrow lengths are saturated in the Southern Ocean. Weak banding is visible in the tropics generally. The corresponding hydrostatic pressure field at this depth is shown. {quiver_map_20

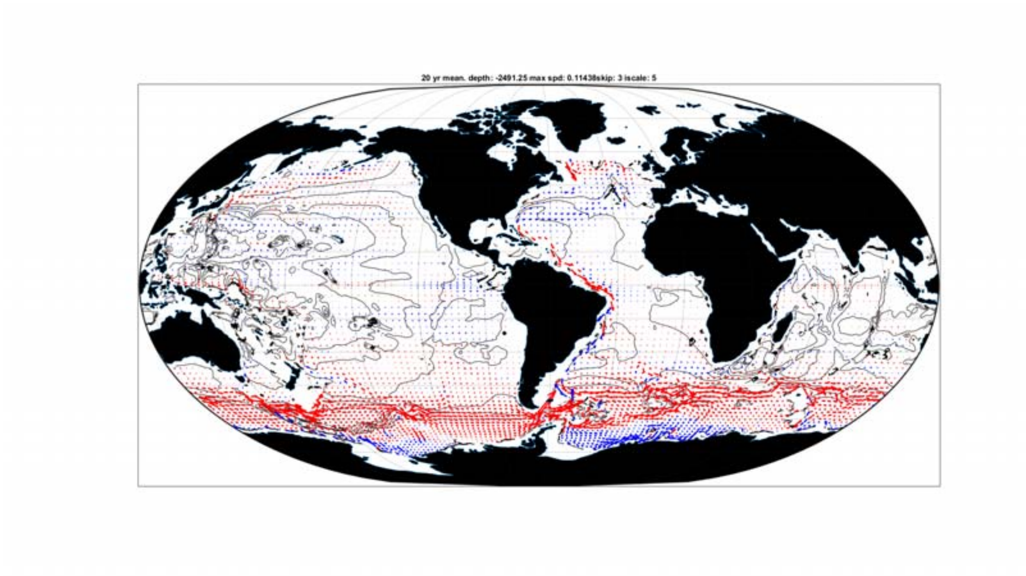

Figure 7: Same as Fig. 4 except at 2500m . Largest arrow corresponds to 13 cm/s. The Atlantic deep western boundary current and the Southern Ocean eastward flow are the most conspicuous features.

{quiver_map_20

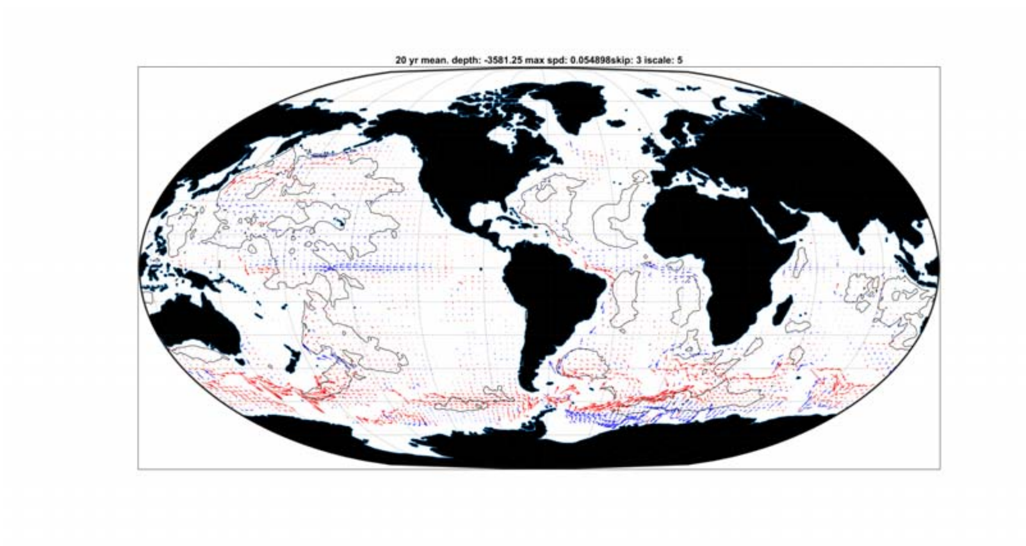

Figure 8: Twenty-year average horizontal flow at 3600m with the 5000m contour and not the pressure field. Largest arrow is 5.5 cm/s.

{quiver_map_20

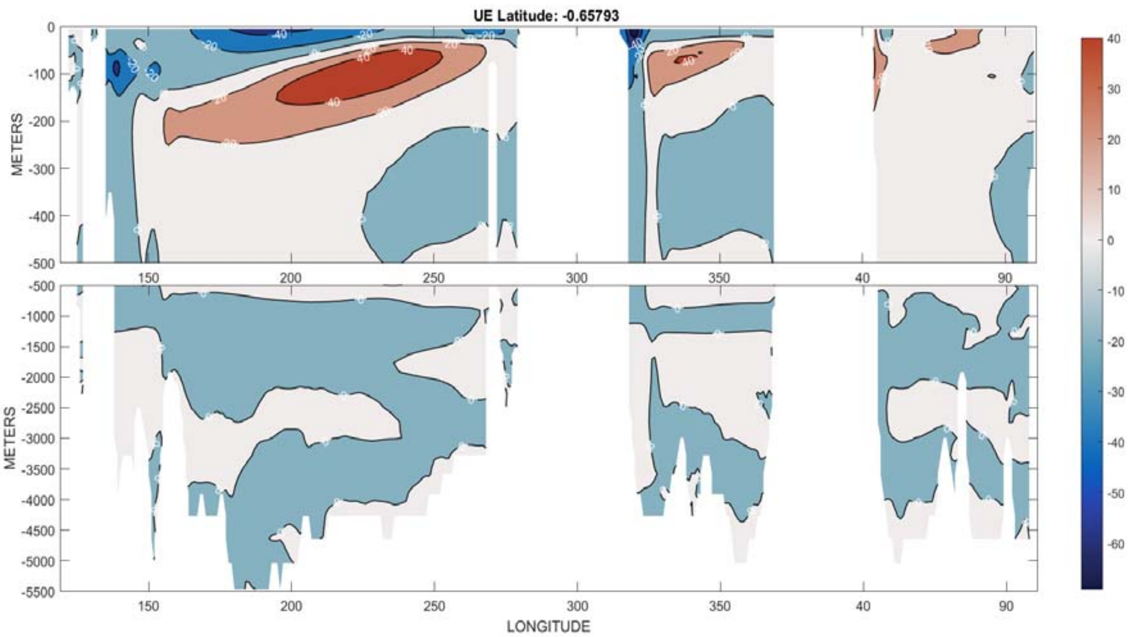

Figure 9: Twenty-year average Eulerian zonal flow, u, *along* the equator in all three oceans (cm/s). The eastward flowing equatorial undercurrent is visible in the Pacific and Atlantic Oceans, as is a zonal westward flow below. {ue_20yr_secti

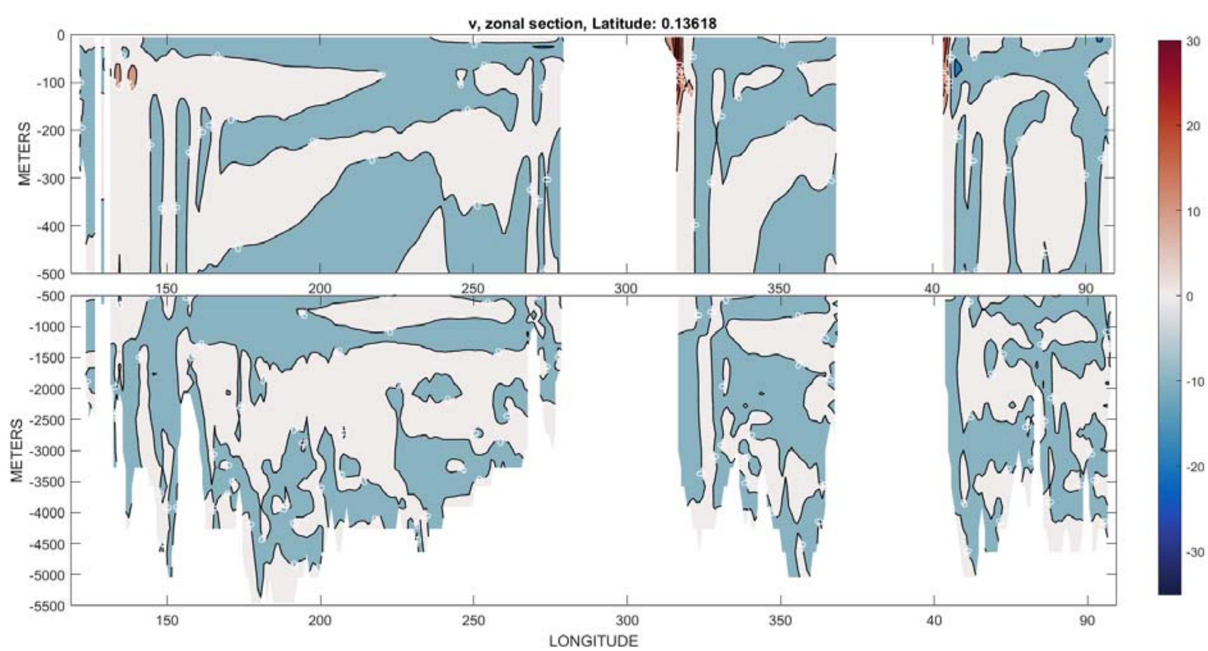

Figure 10: Twenty-year average mean Eulerian meridional velocity, v, at the equator (cm/s). {vn_equatorial

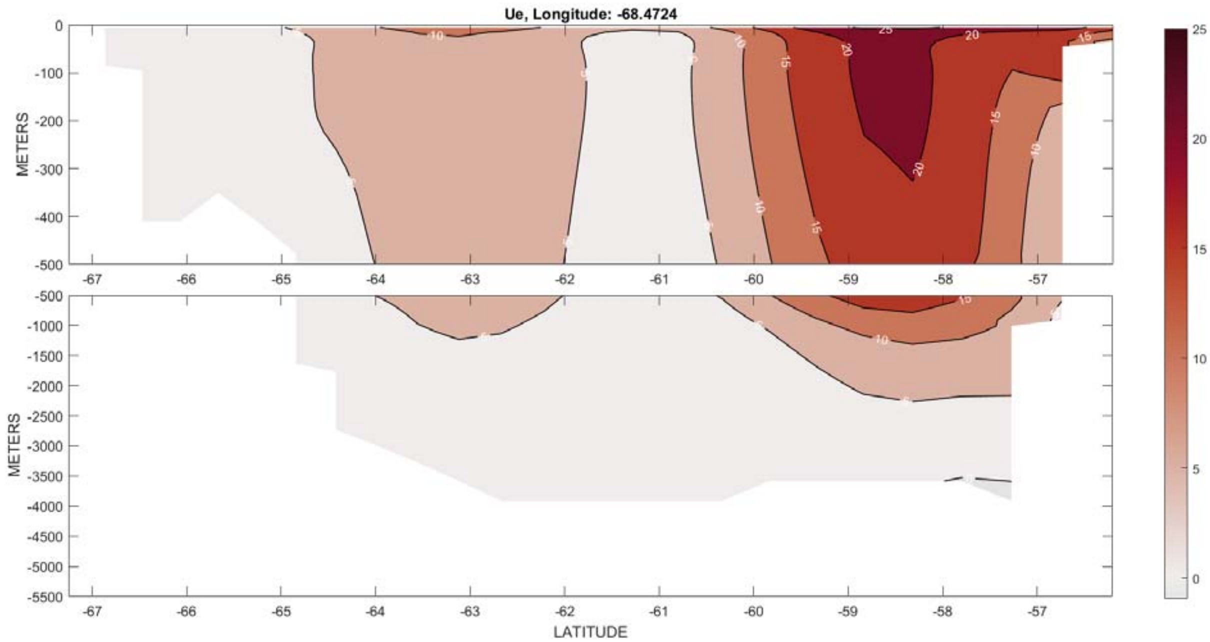

Figure 11: Twenty-year average *zonal* flow, u in the Drake Passage at 70°W. The 20 year average transport is 146 Sv.

{zonalflow_20y

3 Time-Dependent Flows

The oceanic flow field varies on all time scales from seconds to the age of the ocean. In Figs. 13-15 are shown the anomalies of Eulerian velocity about the 20-year mean at 5 m.

A few representative anomalies of the annual average meridional component, v, are shown in Figs. 16-18 across the equator. Such results become part of the story of tropical variability including the ENSO cycle.

Oceanic kinetic energy is one of its basic physical properties. Fig. 19 displays the logarithm of the 5m depth value of the kinetic energy in one year (2004). As expected, some variation in total kinetic energy (top-to-bottom) for each of the 20 years as well as that for the abyssal layer (3600m to the bottom) can be seen in Fig. 20. The slow overall increase over 20 years and the decay in the abyss are not easily testable.

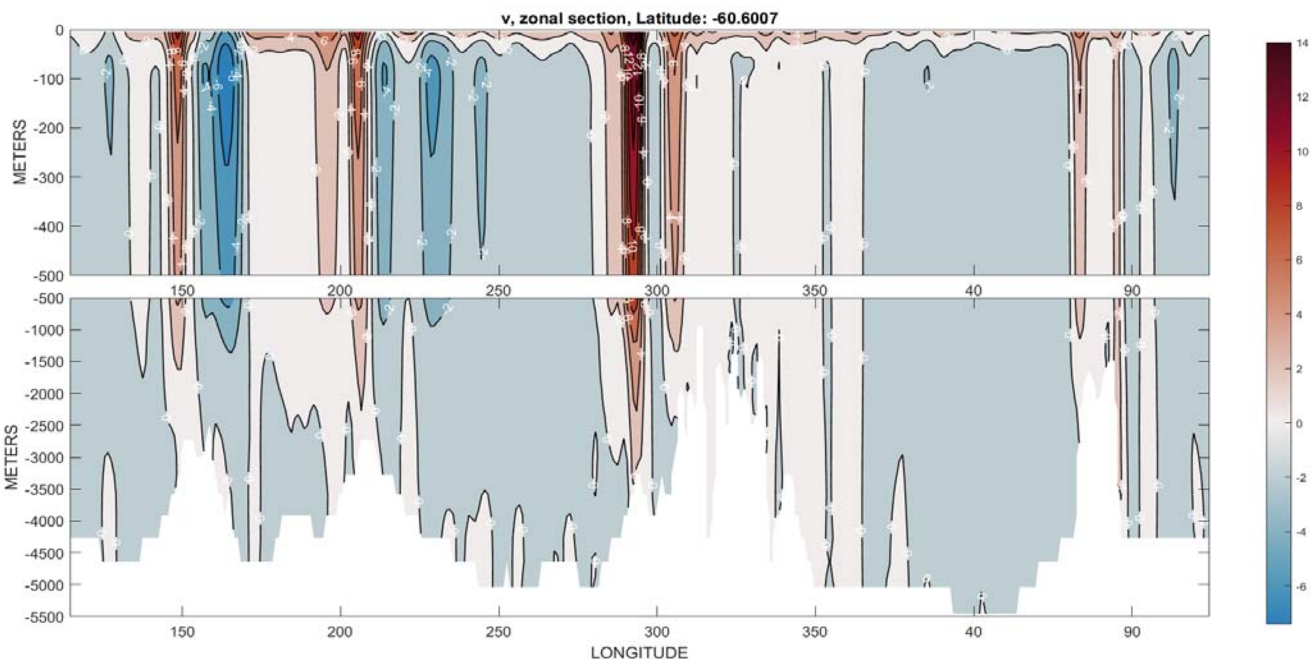

Figure 12: Twenty-year mean meridional velocity, v, in a section through the Drake Passage. A conspicuously variable structure survives 20-years of averaging.

{vn_drakepassa

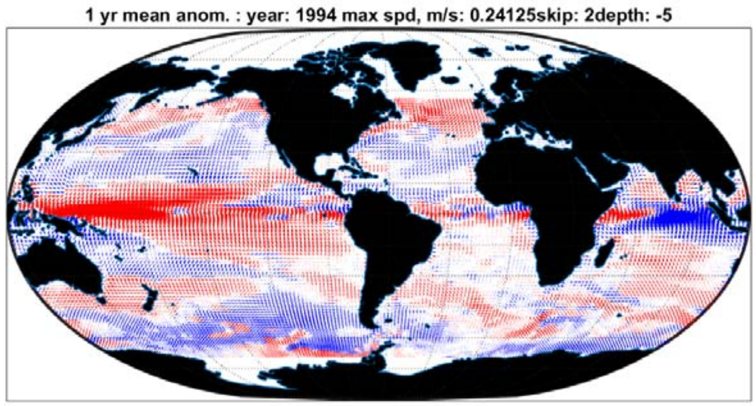

anom yr 1994.tif

Figure 13: Anomaly of the 5m horizontal flow in 1994, again with red arrows having an eastward component. Largest arrow is 24 cm/s. {quiver_anom_y

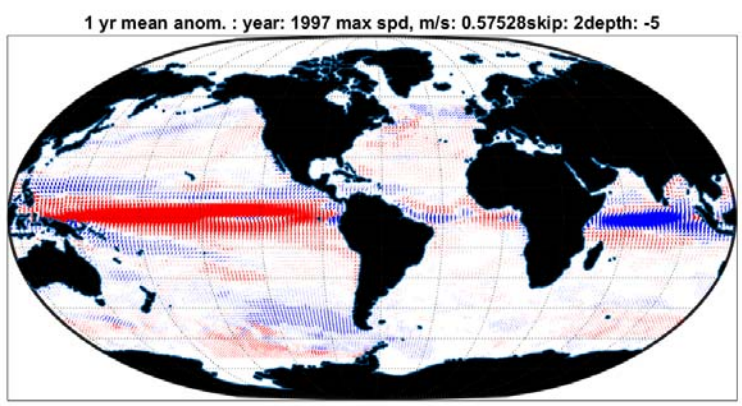

anom yr 1997.tif

Figure 14: Same as Fig. 13 except for 1997 with the largest arrow at 58 cm/s. {quiver_anom_y

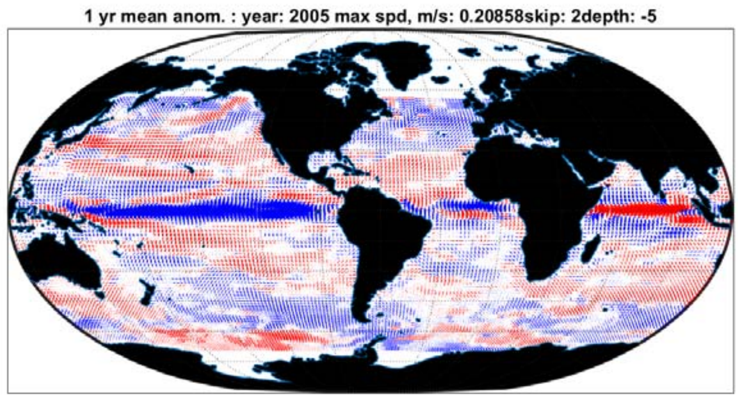

anom yr 2005.tif

Figure 15: Same as Fig. 13 except for 2005 with the largest value be 21 cm/s. {quiver anom y

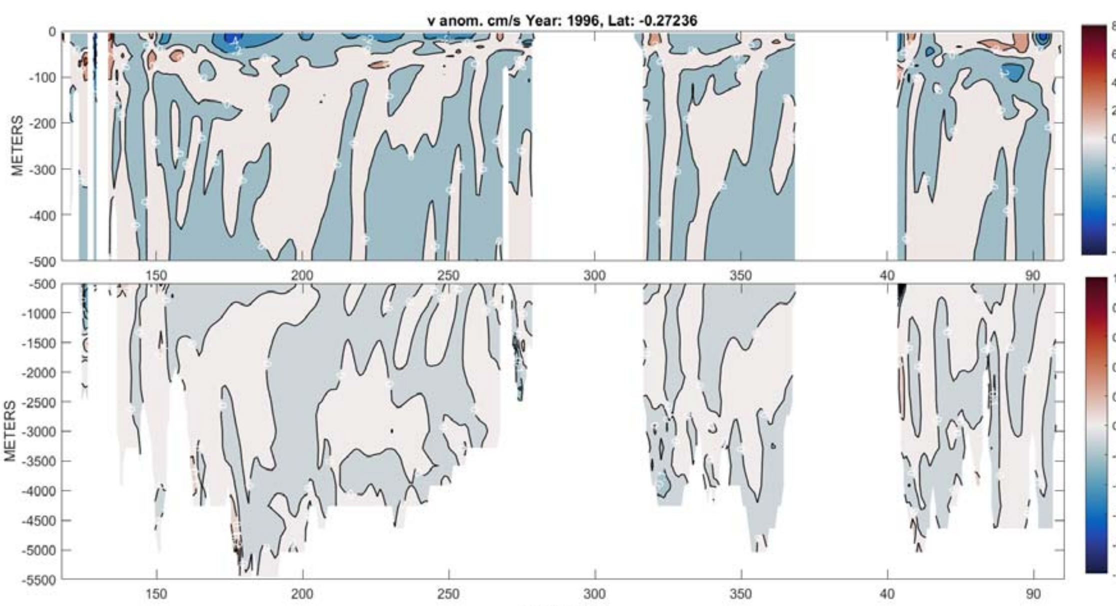

Figure 16: Anomaly of meridional flow across the equator in 1996 (cm/s). {vanom_1996_la

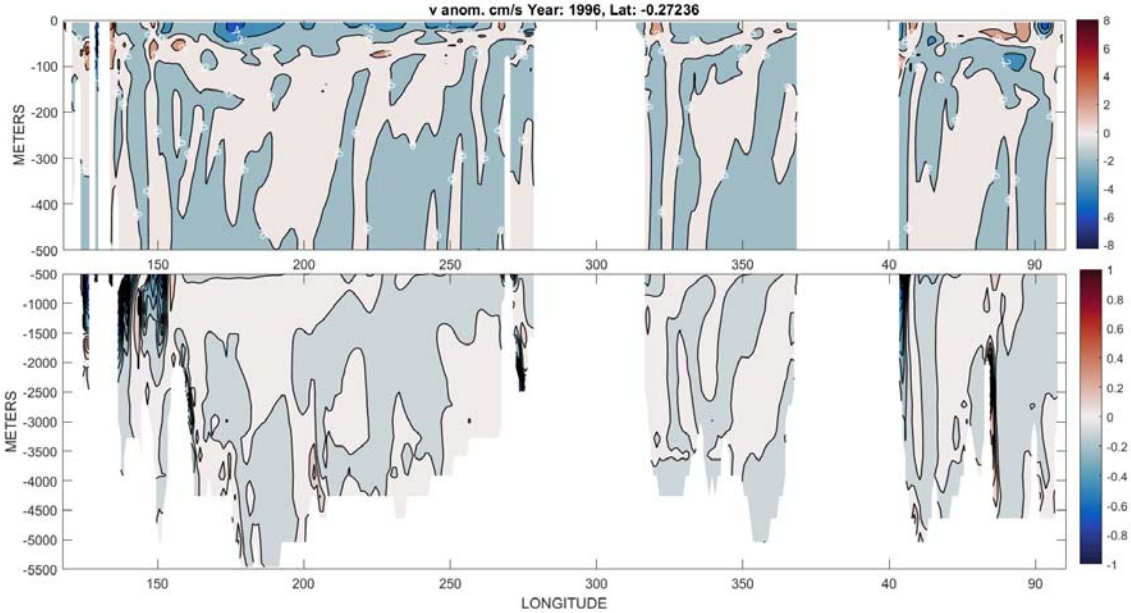

Figure 17: Anomaly of meridional flow across the equator in 1998 (cm/s)—an El Niño year. {vanom_1998_la

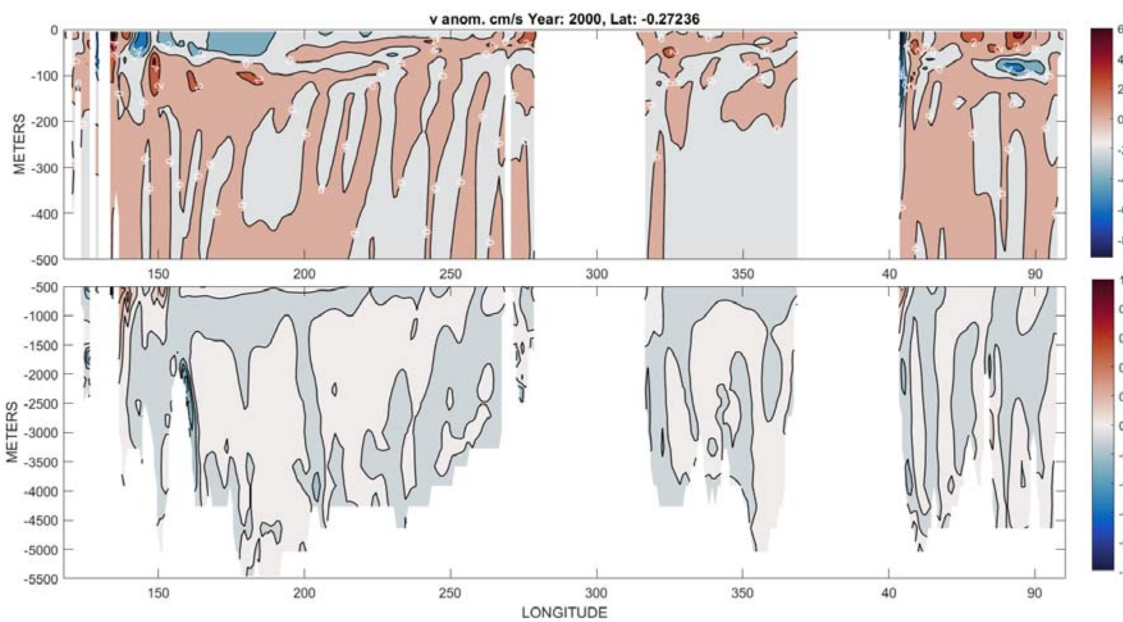

Figure 18: Anomaly of meridional velocity, v, (cm/s) at the equator in 2000. {vanom_2000_la

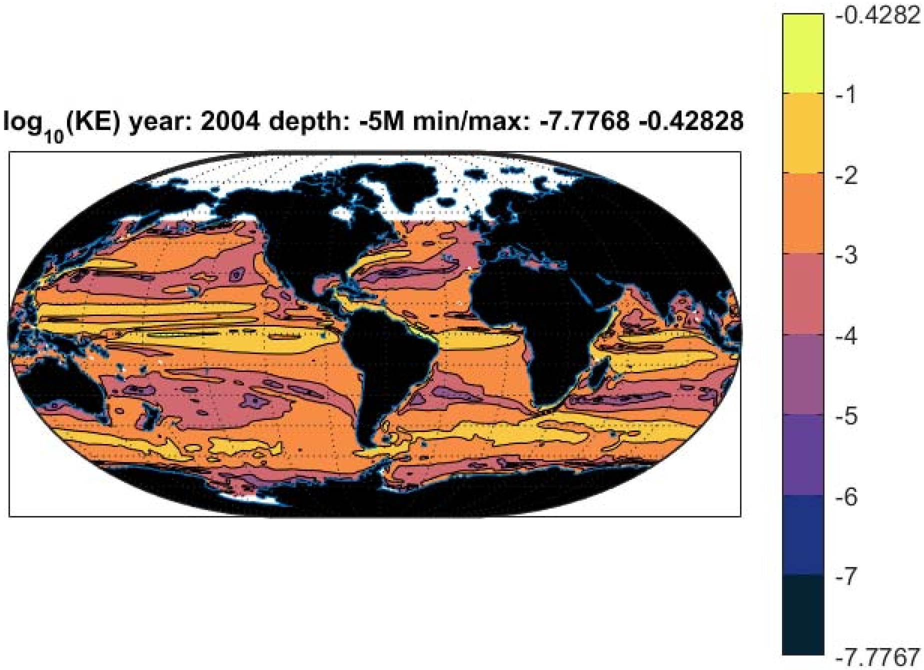

Figure 19: Logarithm of the Eulerian horizontal kinetic energy/unit mass at 5m averaged over 2004. Other years are visually similar, differing in details. {ke_5m_2004.ti

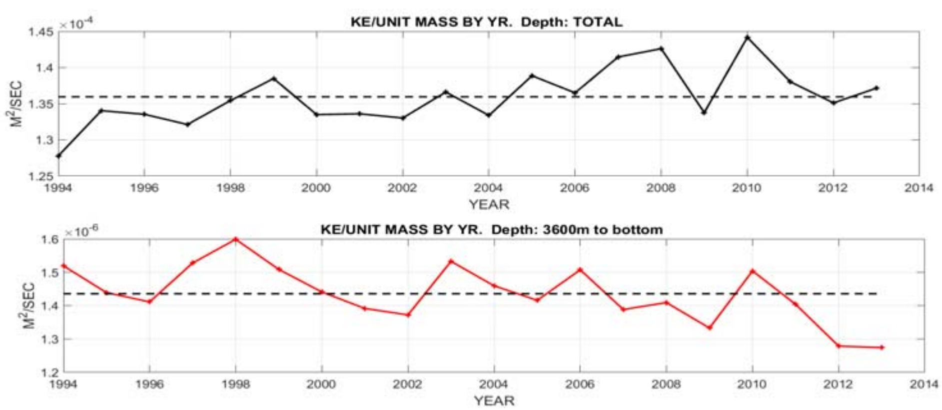

Figure 20: (Upper panel) Total (top-to-bottom) but excluding the northern high latitudes, kinetic energy/kg by year. El Niño year 1998-99 is prominent early in the record. A weak upward trend might be real. (Lower panel) Kinetic energy/unit mass by year in the layer 3600m to the bottom. Note the scale change from the upper panel. {ke_total&3600

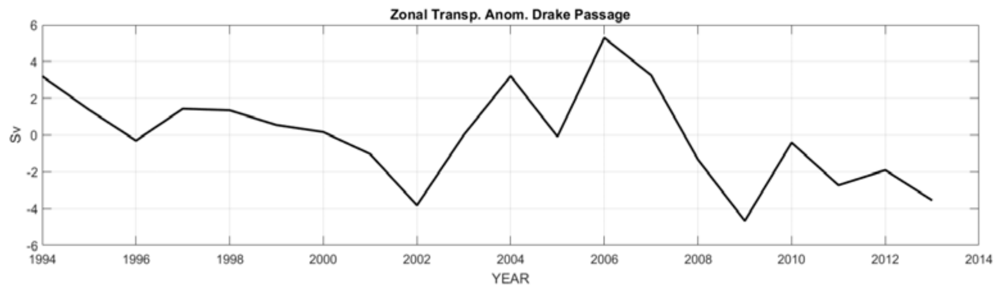

Figure 21: Anomaly (Sv) of transport integrated across the Drake Passage for each year. {yearly_trans_

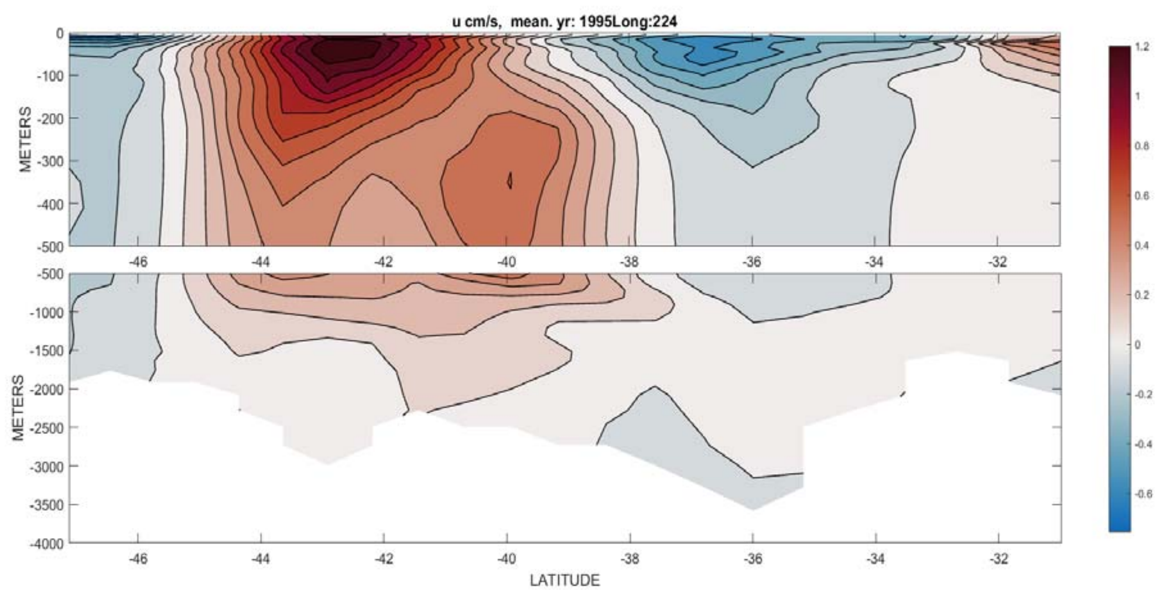

Figure 22: Anomaly of the zonal flow in the Drake Passage in 1995 (cm/s). {u_drakepassag

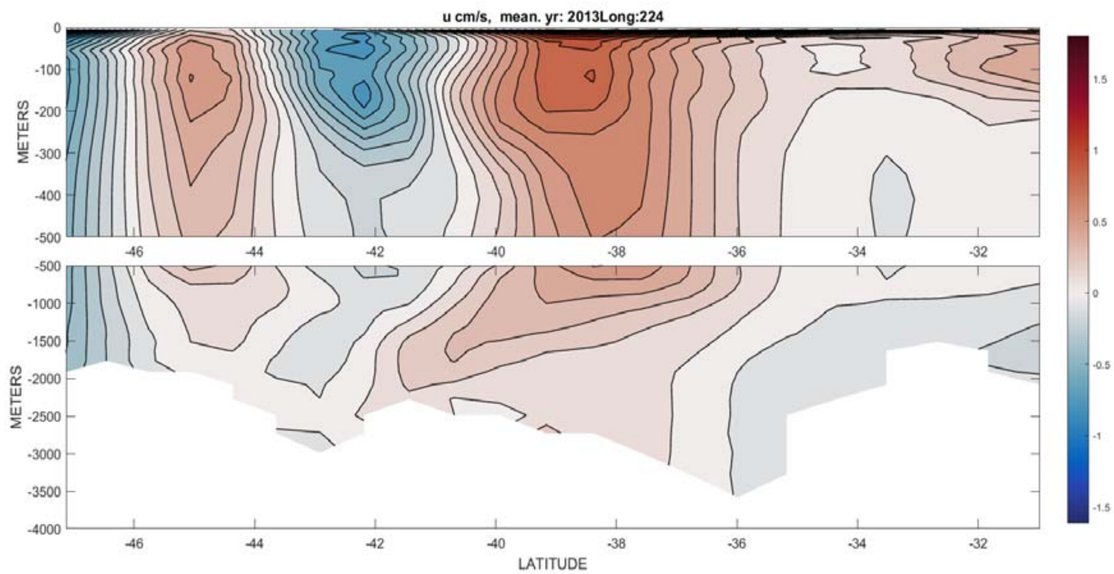

Figure 23: Anomaly of the zonal flow (cm/s) through Drake Passage in 2013. {u_drakepassag

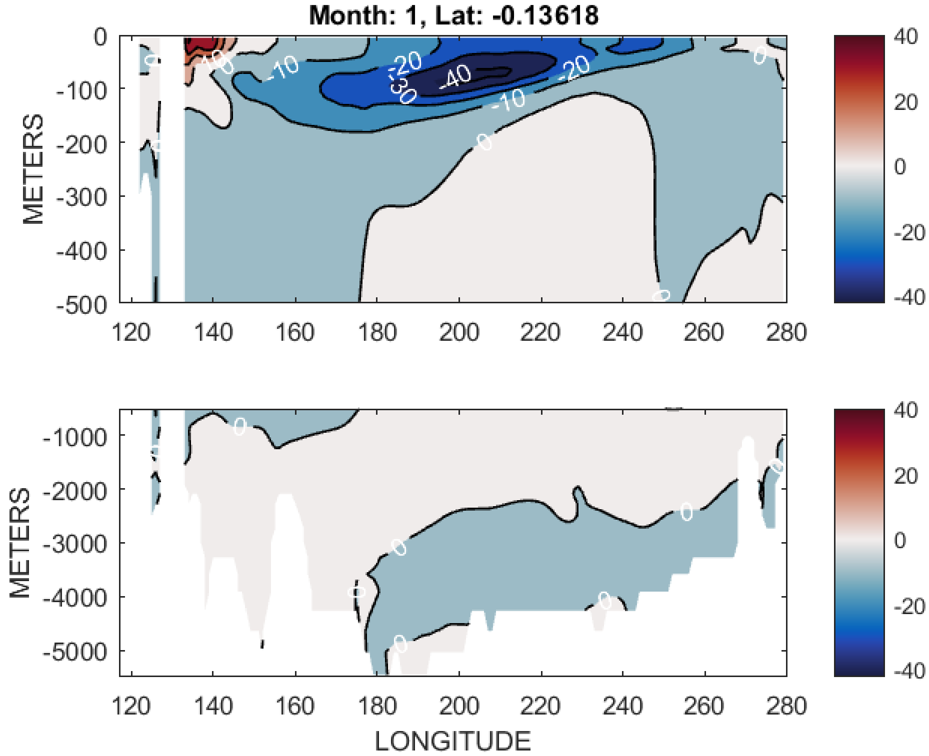

Figure 24: Twenty-year mean zonal flow anomaly (cm/s) on the equator in January in the Pacific Ocean. {equator_jan_s

3.1 Annual Cycle

The annual cycle dominates the atmospheric climate system, with a similar strong response in the very upper levels of the ocean. Simple Rossby wave theory (e.g., Gill and Niiler, 1973; Wunsch, 2015) shows that the vertical penetration of the baroclinic response to annual forcing at the surface is very restricted, but a bit deeper on the equator. An example of the mean annual cycle, shown as the 20-year average of the monthly anomaly of u, along the equatorial section in the Pacific Ocean is displayed in Figs. 24-27 for a few months.. Although the response in the upper 100 m is far larger than at depth, a detectable annual cycle in u exists to the sea floor. Note that interpretation of the upper ocean structures requires use of the mean flow in Fig. 9, as a positive anomaly will weaken the westward-going near-surface South Equatorial Current, and amplify the eastward moving Undercurrent.

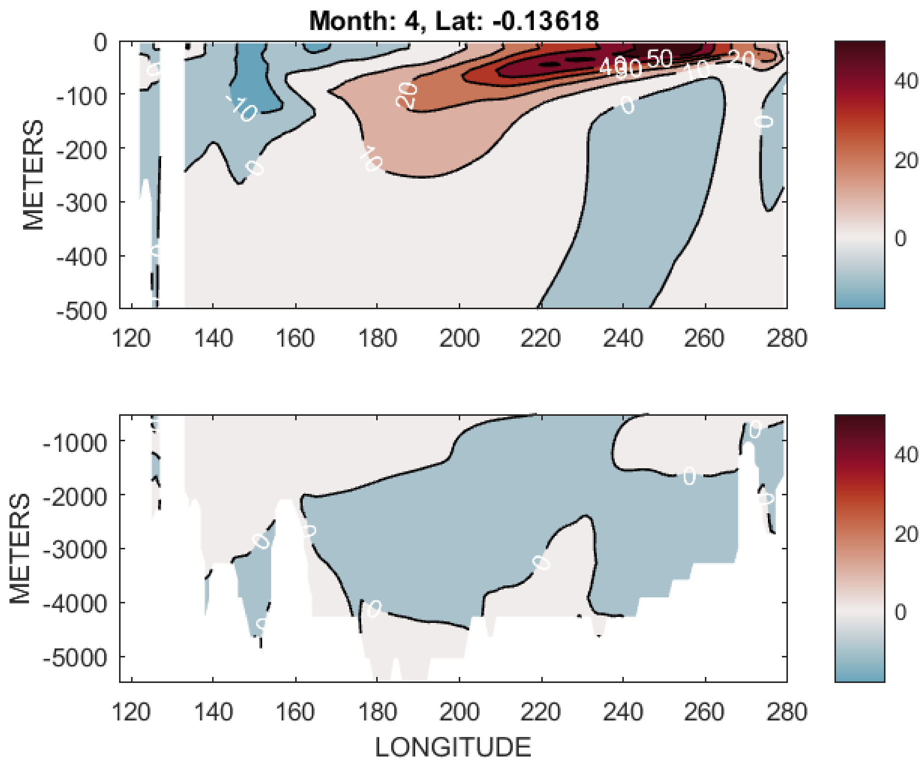

Figure 25: Zonal flow anomaly (cm/s) on the equator, mean April.

{equator_apr_s

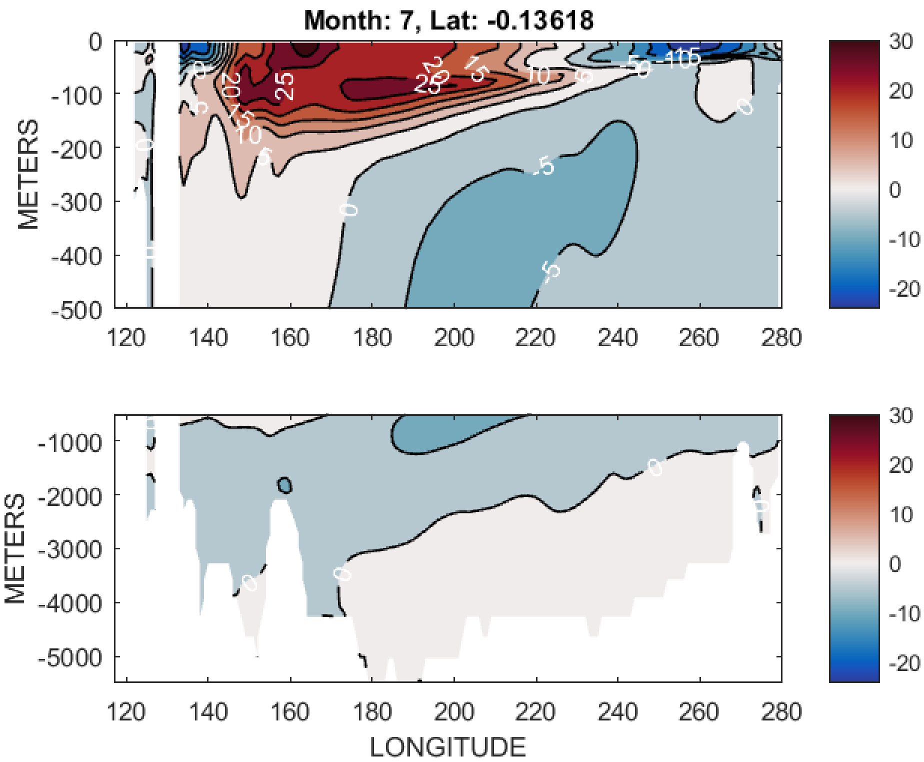

Figure 26: Zonal flow anomaly (cm/s) on the equator, mean July.

{equator_jul_s

3.2 Meridional Transports

One example of a 20-year time mean flow is shown in Fig. 28 at 30°S in the Pacific Ocean. These are readily computed monthly, seasonally etc. for any location.

When integrated through the entire longitude range of 360°, time-average oceanic mass conservation requires that the top-to-bottom meridional transports must vanish up to the divergence contained in net average evaporation plus runoff minus precipitation. The resulting global mean, accumulating integral is shown in Fig. 29. Residual imbalance, an estimate of the average evaporation minus precipitation appears in Fig. 30, but whose properties will be discussed elsewhere. An earlier result is by Stammer et al. (2004).

3.3 Property Transports

The state estimate provides a comprehensive set of output fields on the native grid which permit accurate property transport calculations, consistent with Griffies et al. (2016). As noted already, transport properties involving time mean products such as $\langle vT \rangle$ are expected to be different from values computed from the time means of each, $\langle v \rangle \langle T \rangle$. Thus Fig. 31 displays the depth,

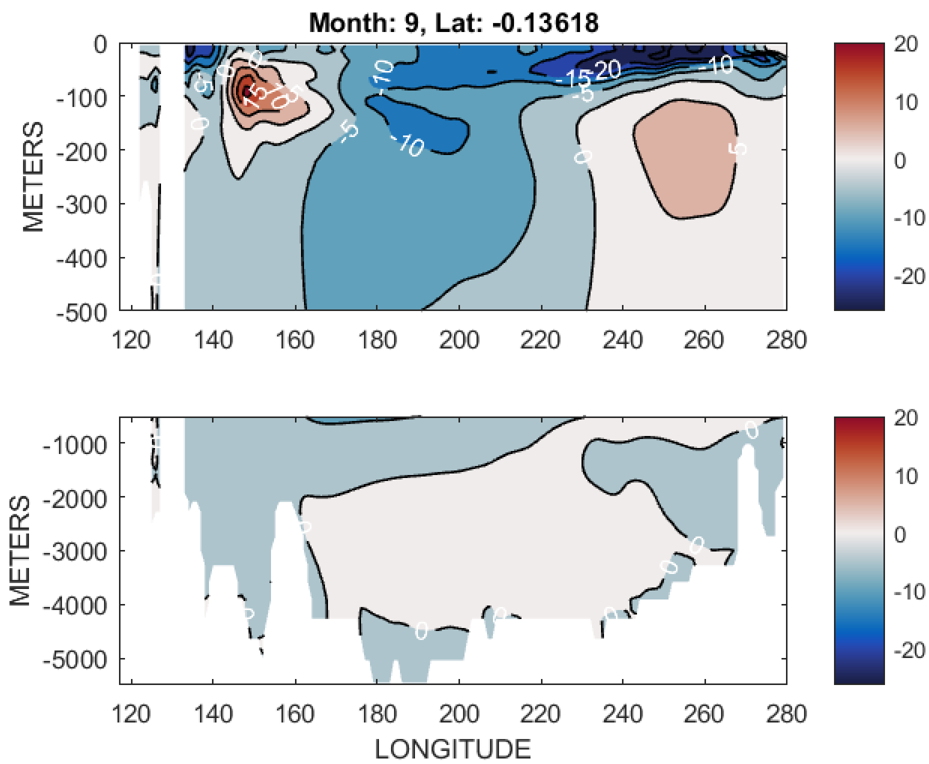

Figure 27: Zonal flow on the equator, mean September. {equator_sep_s

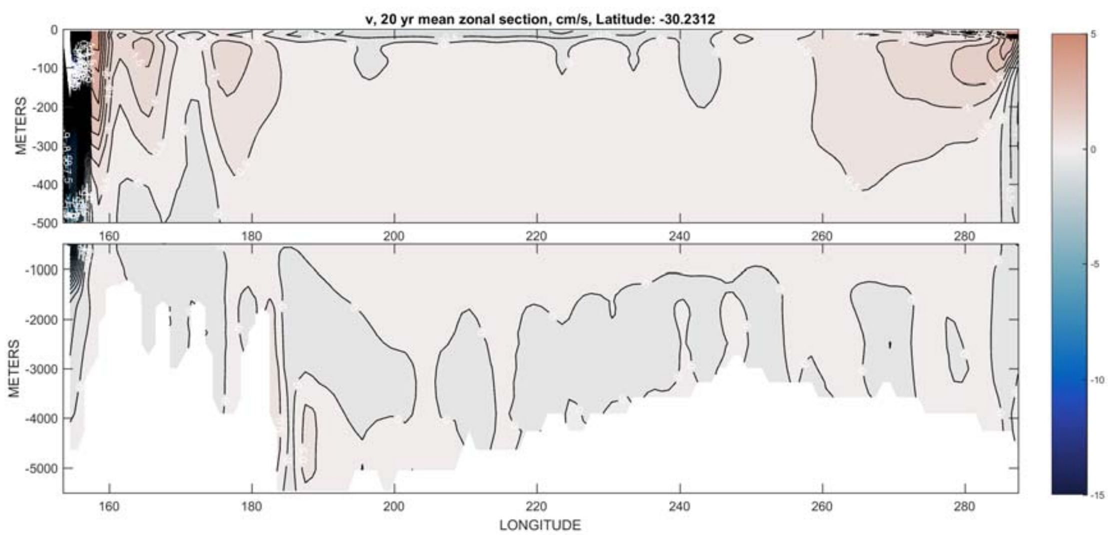

Figure 28: Twenty-year average meridional flow at 30°S in the Pacific Ocean. Intense flow in the East Australia Current and a flow reversing with depth along the coast of South America are visible. As in many such sections, weak deep flow reversals occur throughout. {vn_20yrmean_3

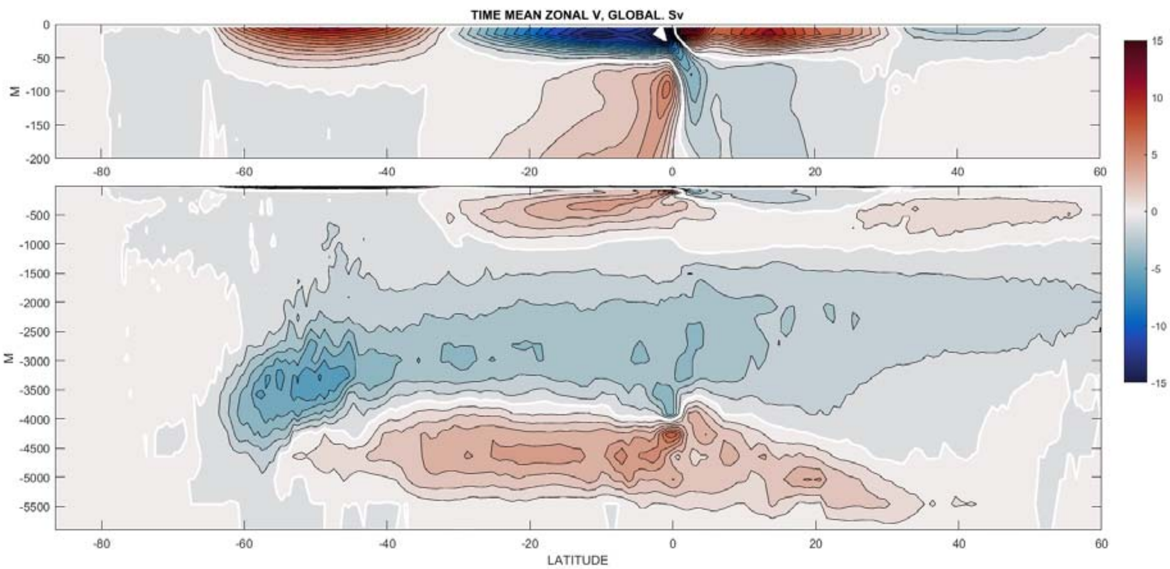

Figure 29: Zonal integral of vertically accumulating meridional transport in Sverdrups. (Not a stream function.) The values at the bottom necessarily almost vanish. See Fig. 30.

{zonal_integra

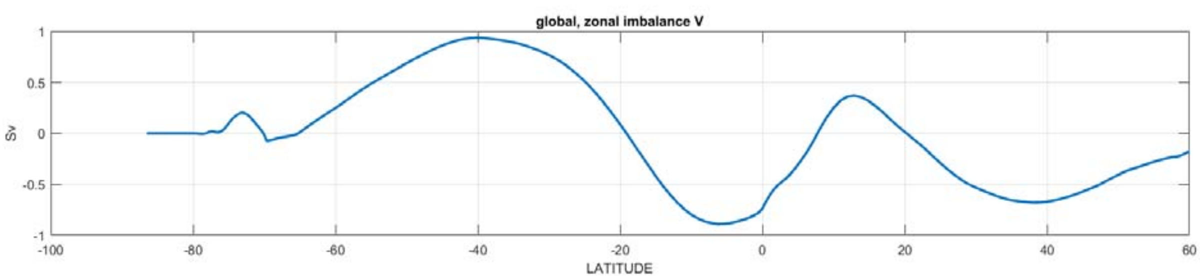

Figure 30: Integral, top-to-bottom, of the meridional transport as a 20-year mean. Bottom value of Fig. 29. Divergence is an estimate of the average evaporation minus precipitation.

{global_imbala

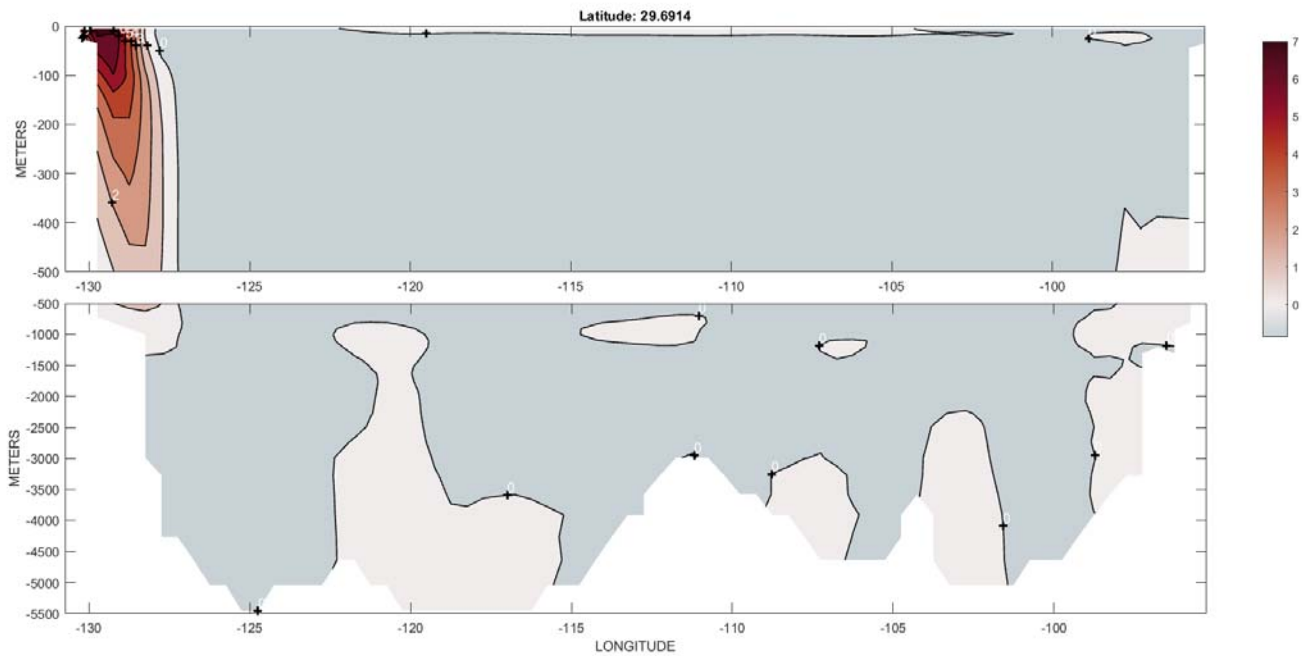

Figure 31: Product of the twenty-year means $\langle \bar{v} \rangle \langle \bar{T} \rangle$ at 30°N in the North Atlantic (m/s °C) with a reference temperature of 0°C. Corresponding heat transport is 0.6PW in contrast to values computed from quasi-synoptic sections of about 1.3PW (e.g., Bryden and Imawaki, 2003). Southward transport in the weak flowing interior is non-negligible.

{vn_theta_sect

longitude contributions of $\langle v \rangle \langle T \rangle$ 30°N in the North Atlantic, producing an equivalent heat transport of 0.6 PW, smaller than estimates based e.g., on monthly or single section data (e.g., Bryden and Imawaki, 2001; Piecuch and Ponte, 2012, Table 2). As with many of the multi-decadal results, these values are best interpreted as quantitatively descriptive, and as serving as tests of unconstrained results from different models.

The corresponding values in the Pacific Ocean at 30°N are negligible (not shown) with a northward temperature transport mainly in the Kuroshio nearly cancelled by the interior return flow.

4 Vertical Velocities

Eulerian Means

Vertical velocities in the ocean are almost never measured directly, but must be computed diagnostically from the horizontal flow divergences. The result for the 20-year average at 105m can be seen in Fig. 32 and is a useful surrogate for the Ekman pumping. (See Roquet et al.,

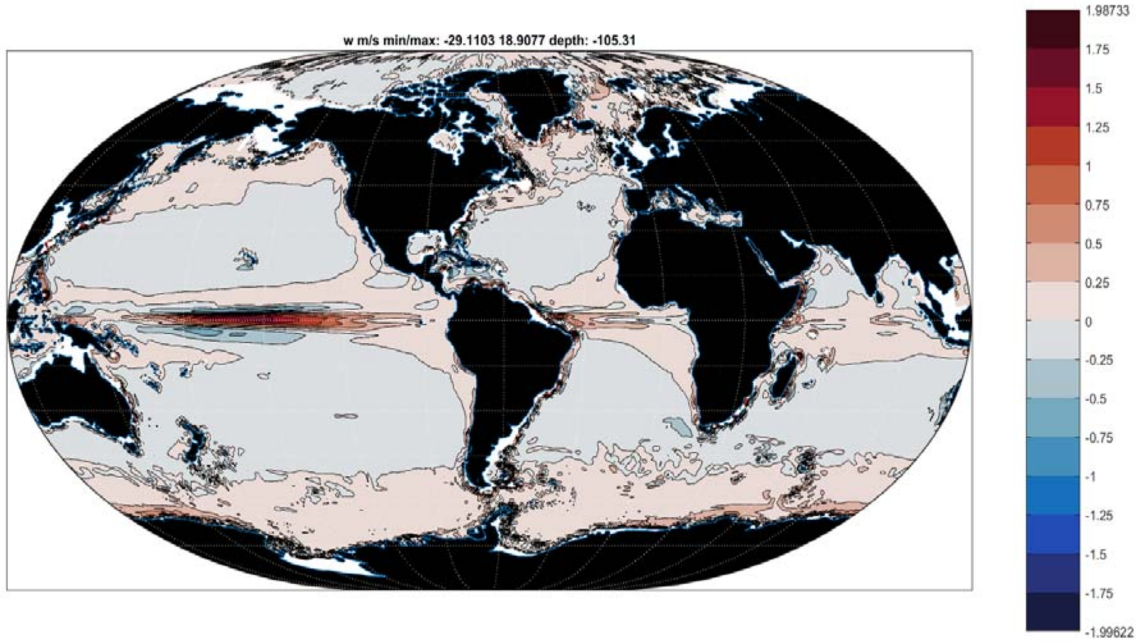

Figure 32: Twenty-year average Eulerian vertical velocity, w, (m/s) at 105m depth. Intense upwelling is appparent on the equator in all oceans, at high latitudes, and in traditional coastal upwelling regions. {map_w_105m_20

2011 for an explicit discussion of the latter.) Main features are the subtropical and subpolar gyres as well as the powerful upwelling on the equator and the upwelling zones on the eastern margins. Fig. 33 shows the same result, but at 720m. At greater depths, e.g. 2000m (Fig. 34), the influence of bottom topography has begun to dominate and the complexity of w defies simple description. Liang et al. (2017) provide a fuller discussion.

The mean annual cycle of w at 105m is shown in Figs. 35-38 and can be regarded as a quantitative estimate of the cycle in Ekman pumping.

5 Meteorological Variables

Meteorological forcing at the sea surface is part of the state estimate control vector—that is, the a priori windstress, surface air temperatures, specific humidity, shortwave downwelling radiation, and precipitation are modified along with other elements of the control vector so that the model is as consistent as possible with the oceanographic data. Comparatively small adjustments are made to the values obtained from the Dee et al. (2014) ERA-Interim atmospheric "reanalysis."

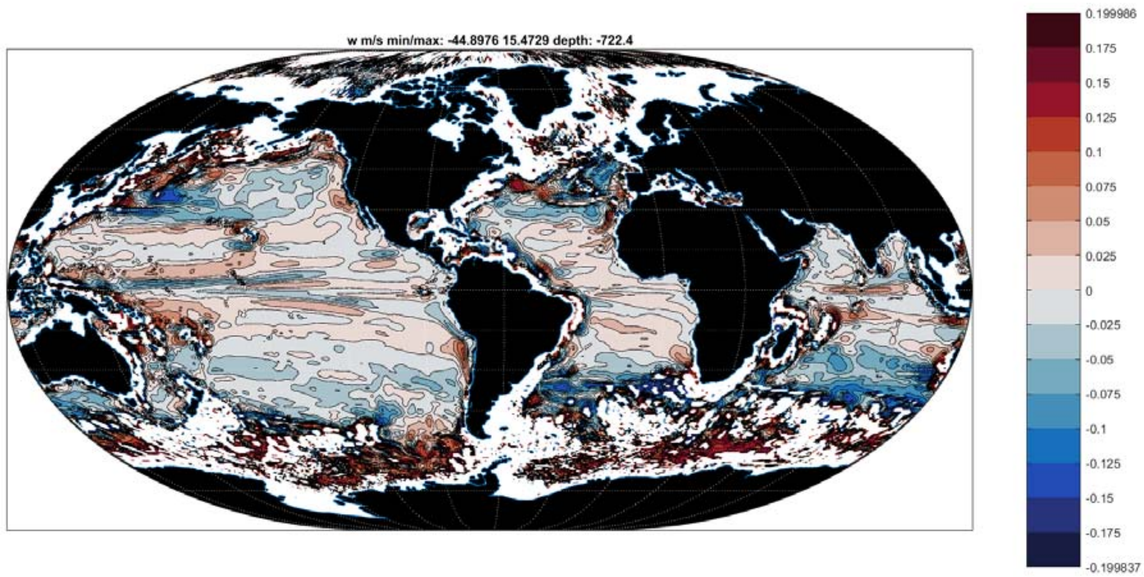

Figure 33: Twenty-year average vertical velocity, w, (10^5m/s) at 720m. The most conspicuous mid-latitude feature is the zonal banding, with a small residual of the large-scale surface gyres still visible. The Southern Ocean stands out as a region of extremely intense values of w of both signs (extreme values have been truncated there). {map_w_720m_20

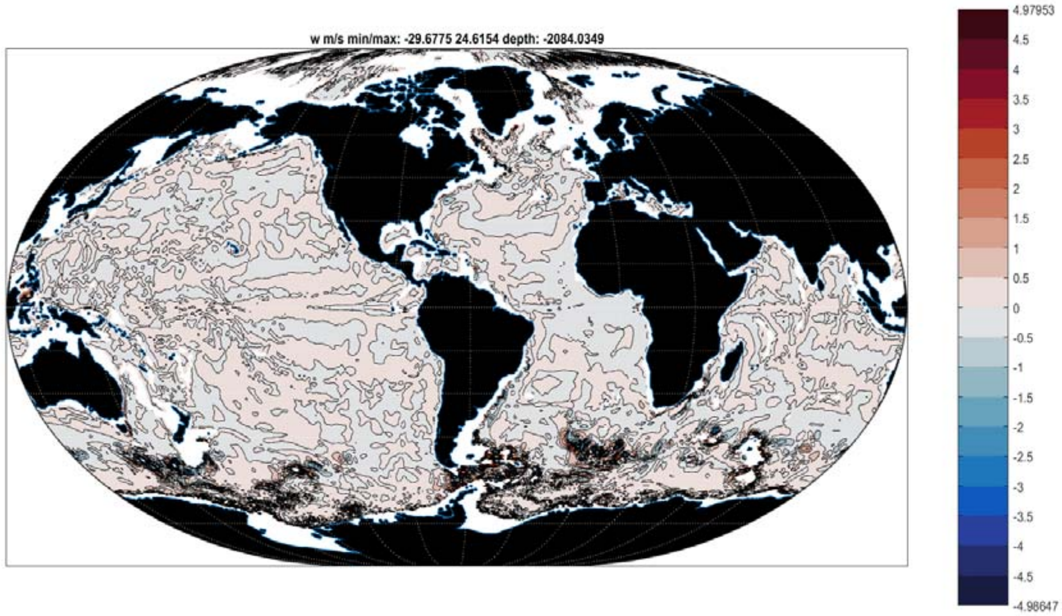

Figure 34: Twenty-year mean Eulerian w at 2100m (10^5m/s). At this depth, the complex structures induced by topography come to dominate the patterns. Some extreme values near topographic features have been omitted. See Liang et al. (2017).

{map_w_2084m_2

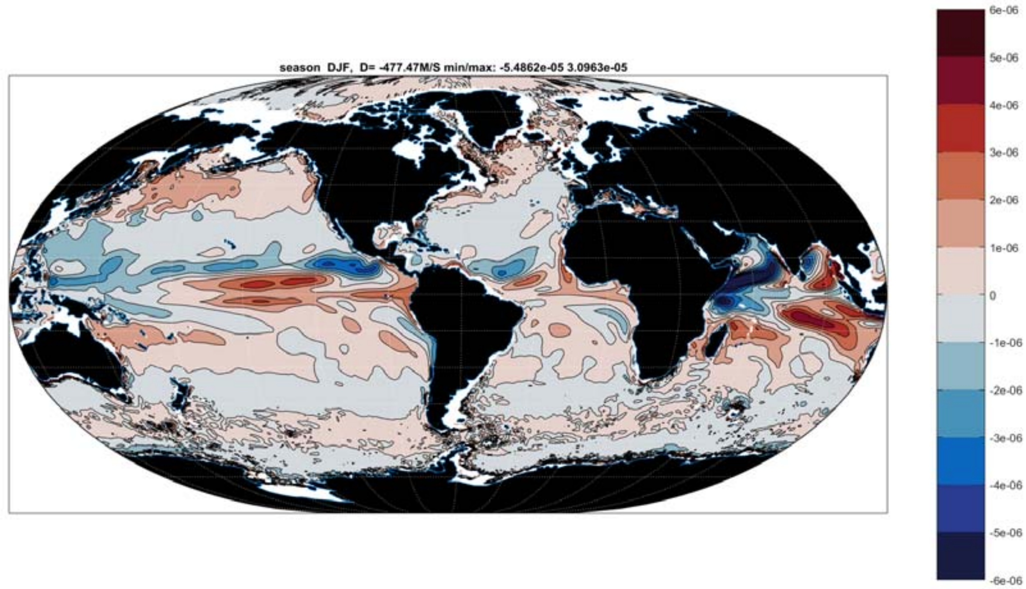

Figure 35: Twenty-year seasonal anomaly of w at 105m DJF.

{mapw_105m_sea

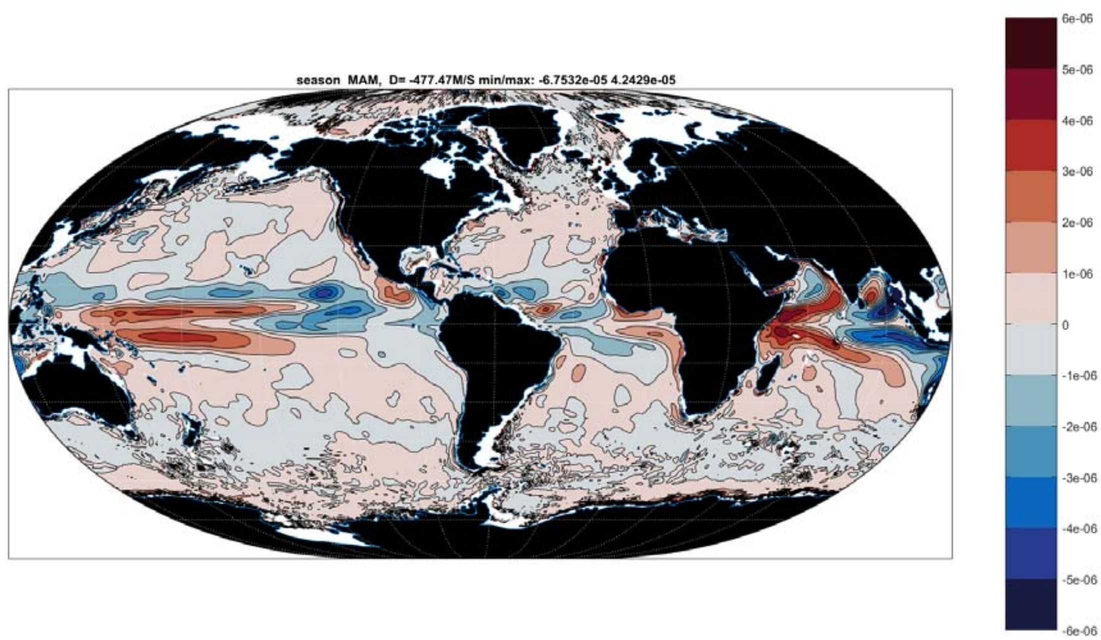

Figure 36: Anomaly of w, 105m March, April, May. (m/s, not multiplied by 10^5)

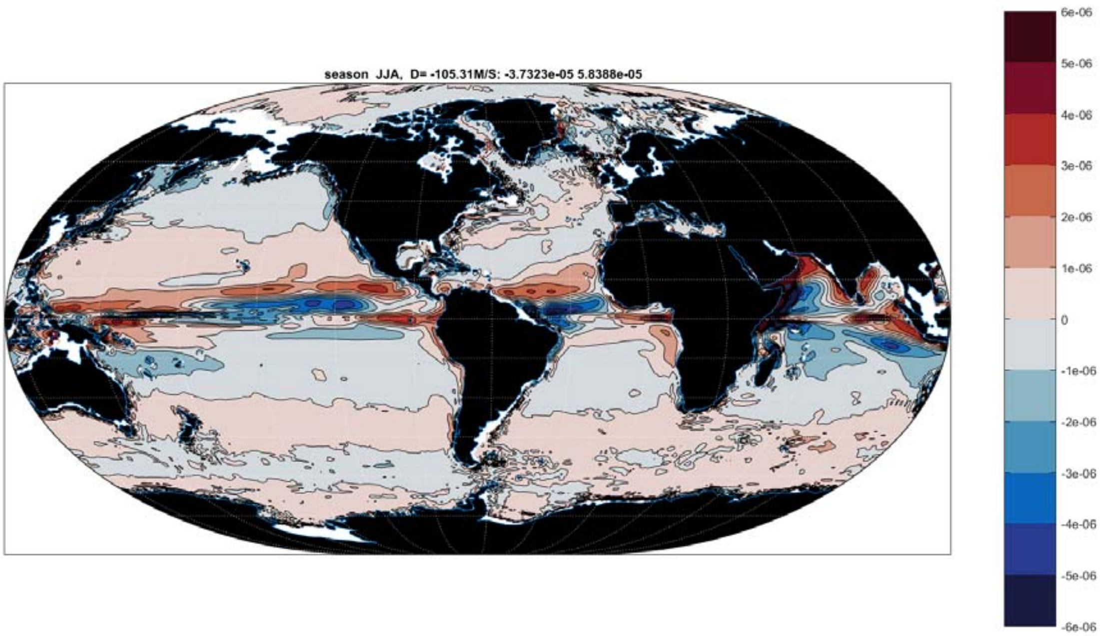

Figure 37: Anomaly of w (m/s) at 105m, June, July, August. {mapw_105m_sea

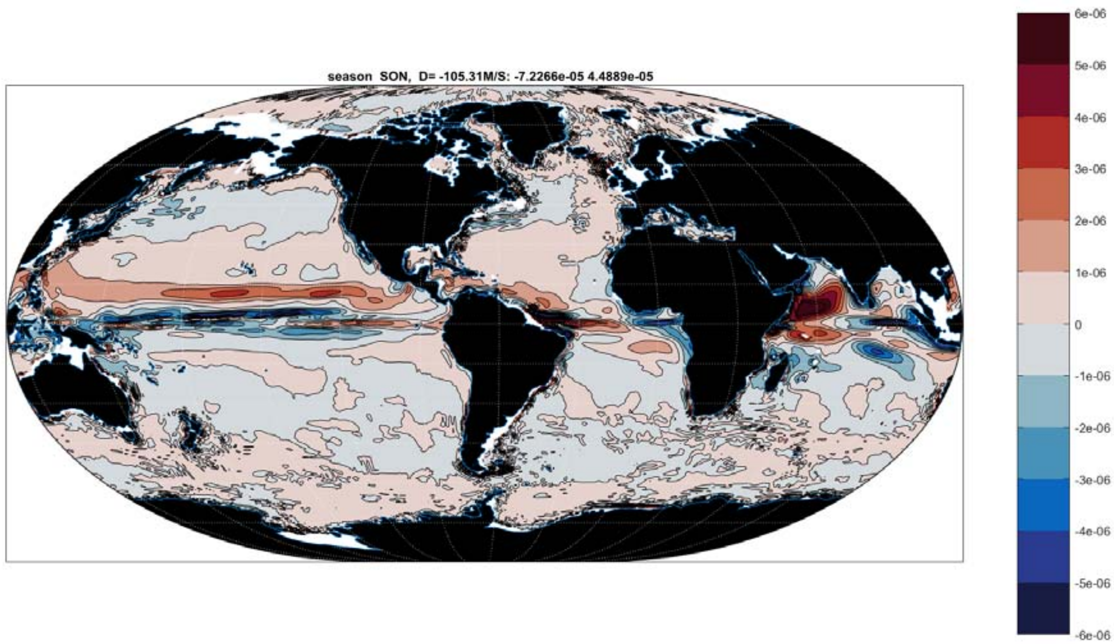

Figure 38: SON anomaly of w,105 m (m/s). {mapw_105m_sea

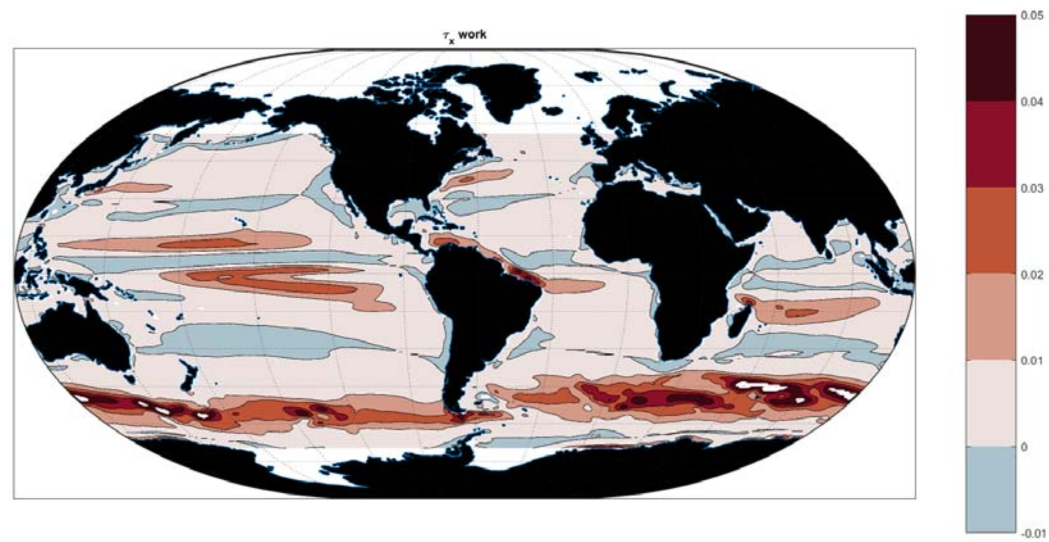

Figure 39: Twenty-year average misfit (here the inferred *correction*) to the time-mean τ_x (N/m^2).The state estimate is obtained by correcting the time-dependent Dee et al. (2014) estimates by a time-varying version of this correction when the model is run forward.

{misfit_taux_m

That reanalysis is not provided with explicit uncertainty estimates, but these have been discussed by Chaudhuri et al. (2014, 2016).

The adjustment (the "misfit" to the reanalysis) to the separate zonal and meridional estimates (τ_x, τ_y) are displayed in Figs. 39, **??** for the 20-year average. A generalization is that fitting to oceanic data strengthens both components of $\boldsymbol{\tau}$ at high latitudes, and tends to weaken them in the subtropics and tropics. The global realism of these adjustments remains to be tested. Similar charts can be made for monthly, annual, or seasonal, etc. misfits.

The 20-year average wind-stress as adjusted by the state estimate calculation is shown in Fig. 41. On the large-scale the conventional easterly and westerly wind bands are all prominent. Its curl is shown in Fig. 42 and can be compared to Fig. 32, keeping in mind that the Ekman pumping, $w_E = \nabla \times (\boldsymbol{\tau}/\bar{\rho} f)$.

The rate of wind working on the surface flow (not just the geostrophic component) is readily computed from the products $W_x^{(1)} = \langle \tau_x \rangle \langle u\,(z=5) \rangle, W_y^{(1)} \langle \tau_y \rangle \langle v\,(z=5) \rangle$ in Figs. 43, 44 although as discussed earlier, these are only a part of the respective second order products $\langle \tau_x u \rangle$, $\langle \tau_y v \rangle$, and can only be interpreted as the work done by the mean wind on the mean surface flow. Omitting high ice-covered latitudes, thus the spatial average value is $W_x^{(1)} = 0.0043 \mathrm{W/m^2}$ and $W_y^{(1)} = -0.00025$ W/m^2 which integrate to a total rate of working of about 1.6 TW. Monthly or

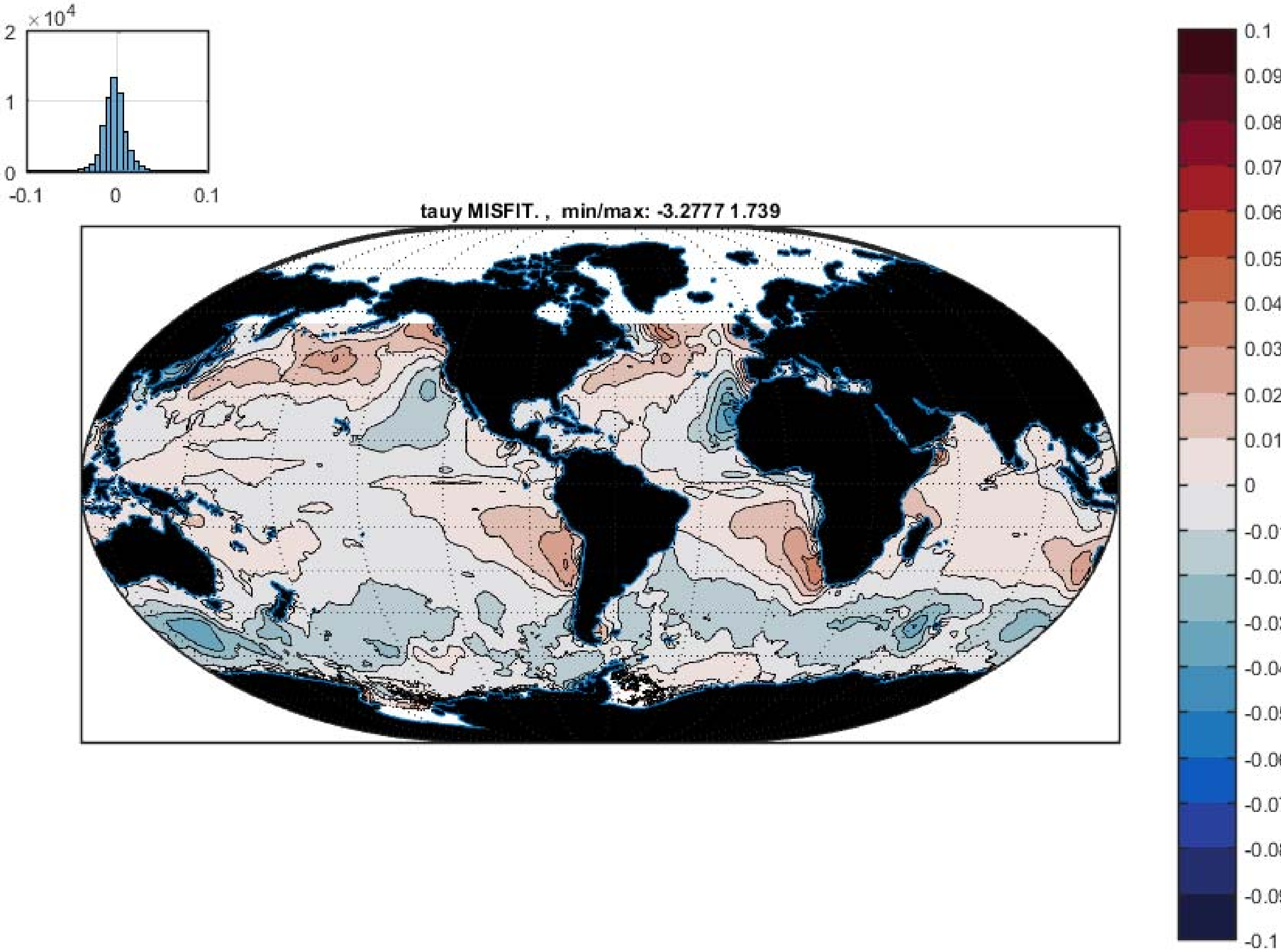

Figure 40: Twenty-year average "misfit" or correction to the time-mean τ_y (N/m^2). {misfit_tauy_2

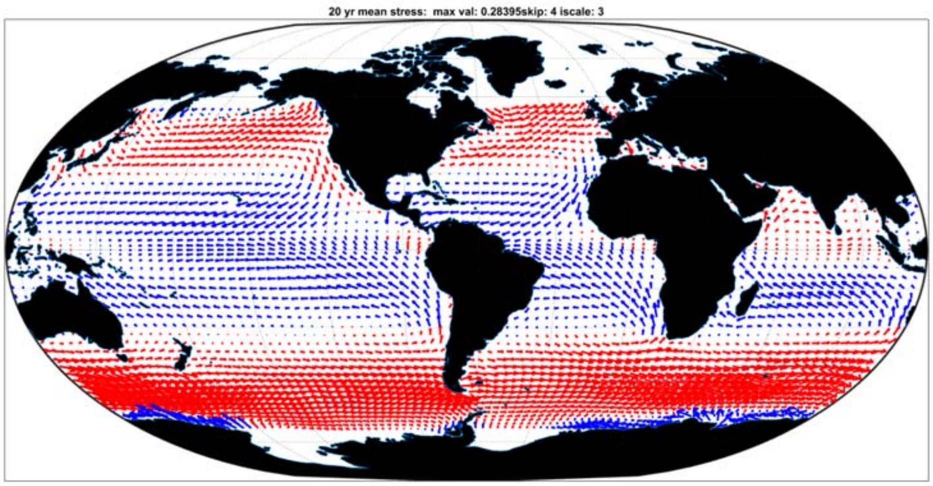

Figure 41: The 20-year average wind stress vectors (N/m^2) after adjustment by the state estimate calculation.

{quiver_tau_ar

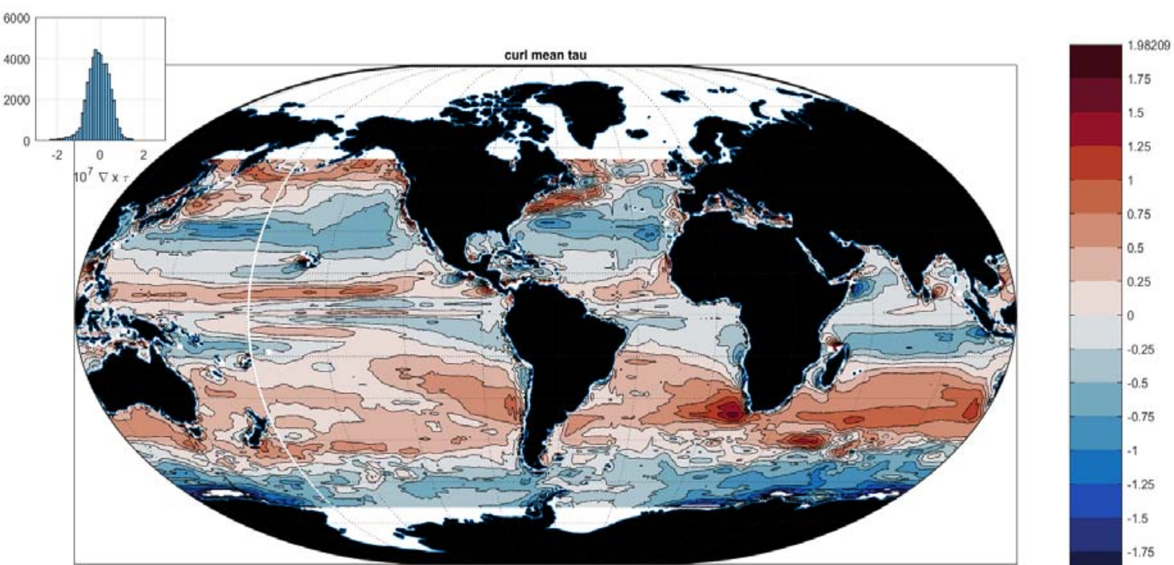

Figure 42: Vertical component of the curl of the 20-year average wind stress in Fig. 41.

{curl_20yearme

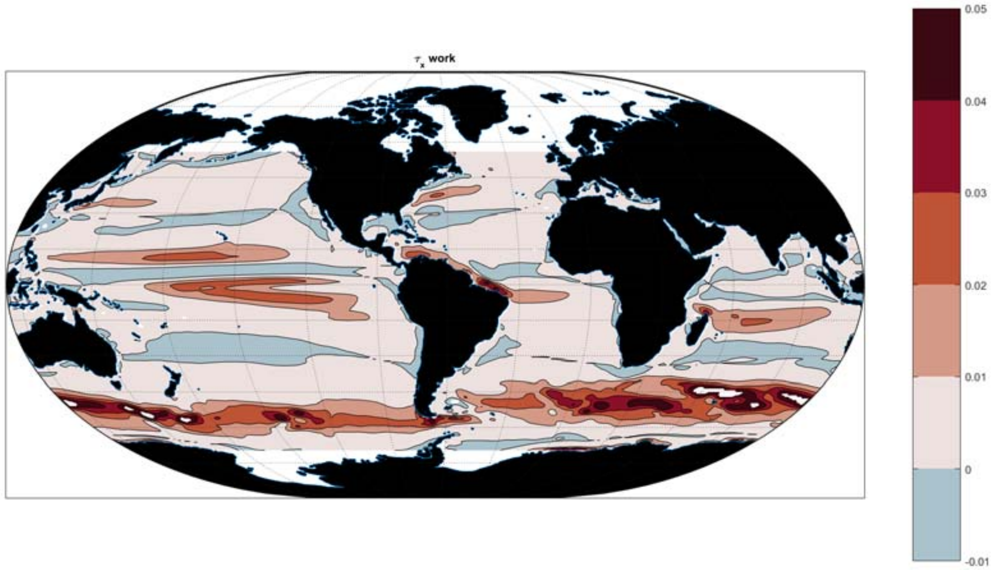

Figure 43: Wind work by the 20-year zonal average wind on the 20-year average surface velocity. (W/m^2) {taux_work_map

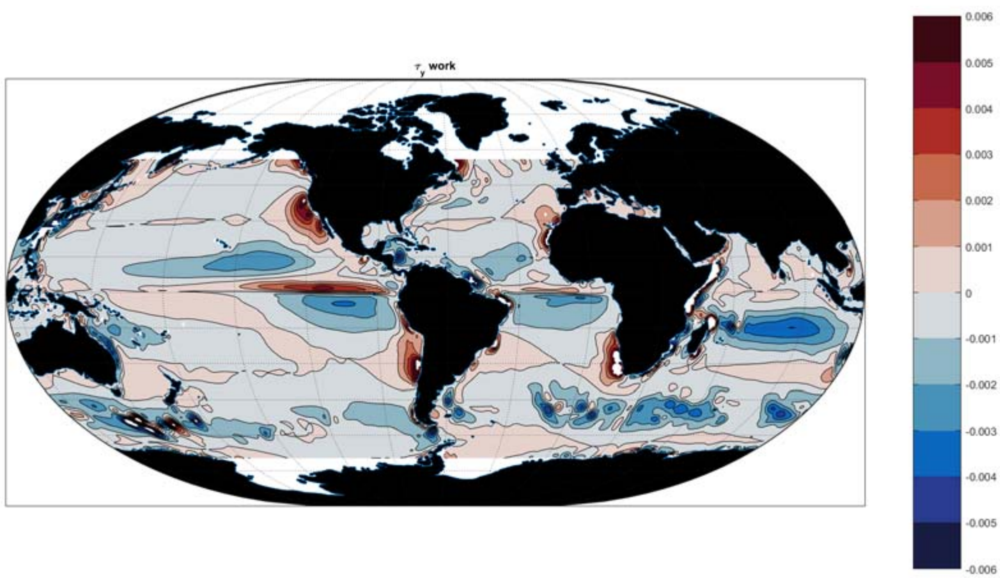

Figure 44: Rate of work on the time-mean sea surface velocity (W/m^2) of the meridional component of the wind stress. Note the change in scale from Fig. 43. Coastal upwelling regions tend to dominate. {tauy_work_map

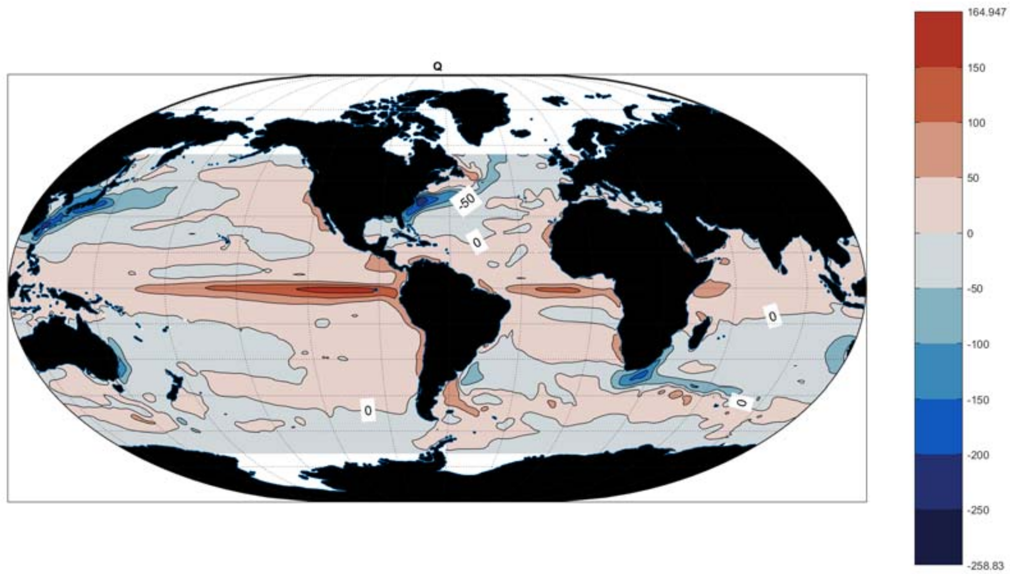

Figure 45: Twenty-year average estimated net heat exchange with the atmosphere (W/m^2) with positive values indicating a flux into the ocean. {q_20yearmean.

seasonal or annual values of the rate of working can readily be computed from the climatology, but pursuit of this subject is left for elsewhere (see Zhai et al., 2012).

Heat Exchange

The 20 year average heat exchange, Q, with the atmosphere is depicted in Fig. 45 and its 20-year average seasonal anomalies in Fig. 46. Qualitatively, these are all conventional, with heat gain in the tropics and major heat loss over the western boundary currents. Liang and Yu (2016) have compared these and related fields to reanalyses and OAFlux/CERES, showing a greater consistency with observations than do other estimates.

6 Eddy Contributions

As described by Forget et al. (2015), the model contains a variety of parameterizations intended to mimic the influence of eddies, waves and a variety of physical processes not properly resolved by the present model grid. Most of these formulas include empirical parameters varying horizontally, with depth, and in some cases, time. A full depiction of all of them would be overwhelming in the present context. As one example of what is now possible, Fig. 47 depicts the so-called bolus velocity at 722m derived from the Gent and McWilliams (1990) parameterization (cf. Ferrari

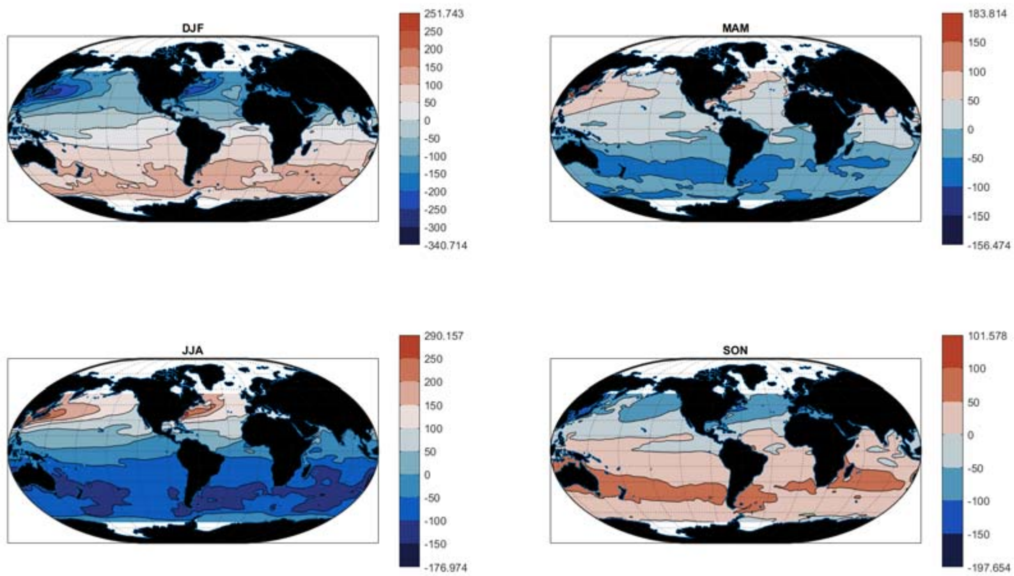

Figure 46: Anomaly of Q ($\mathrm{W/m^2}$) by season. Note changes in color scales. {q_anom_4seaso

and Plumb, 2003; Ferreira et al., 2005; Young 2012). As expected, a complex pattern results, one dependent upon the stability properties of the parameterized eddy field. On average, as compared to the Eulerian mean velocities, the relative kinetic energy in the bolus velocities is very small (about 0.5%) of the total. These results too, vary with year, month etc., but are not further displayed here.

Acknowledgments. Supported by NASA through the ECCO Consortium through contracts with MIT, AER and JPL.

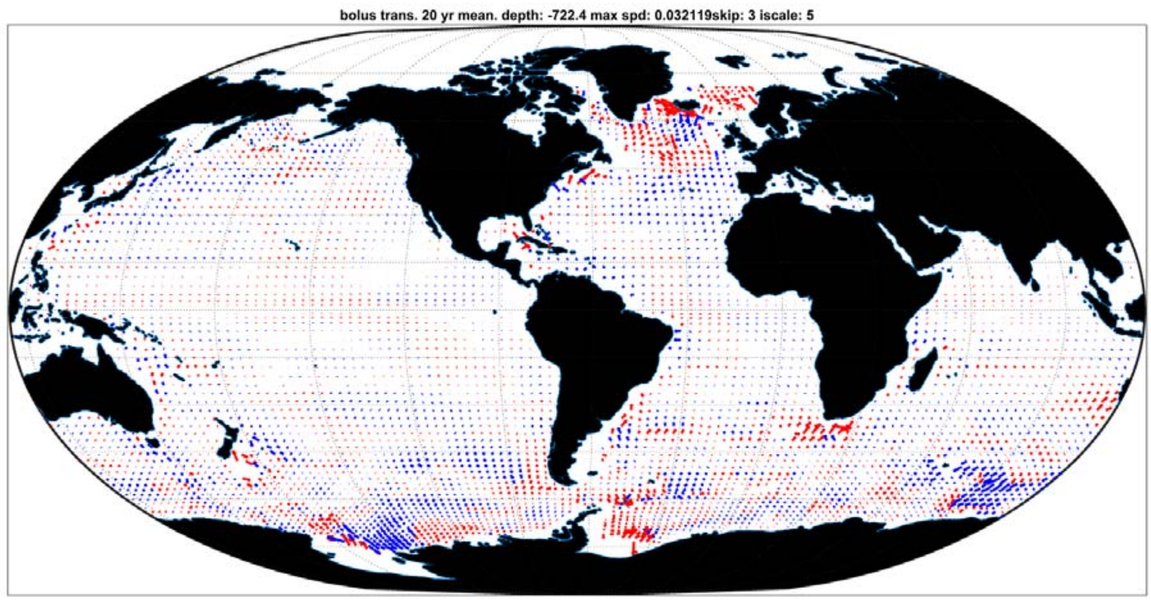

Figure 47: The time mean bolus velocities (u_{bolus},v_{bolus}) at 722m (m/s). {quiver_bolus_

7 References (Including those from Part 1)

A full bibliographic list of ECCO publications can be seen at http://ecco-group.org

Abraham, J. P., Baringer, M., Bindoff, N. L., Boyer, T., Cheng, L. J., Church, J. A.,... Willis, J. K. (2013). A review of global ocean temperature observations" implications for ocean heat content estimates and climate change. Reviews of Geophysics, 51(3), 450-483. doi:10.1002/rog.20022

AchutaRao, K. M., Ishii, M., Santer, B. D., Gleckler, P. J., Taylor, K. E., Barnett, T. P.,... Wigley, T. M. L. (2007). Simulated and observed variability in ocean temperature and heat content. Proceedings of the National Academy of Sciences of the United States of America, 104(26), 10768-10773. doi:10.1073/pnas.0611375104

Adcroft, A., Hill, C., Campin, J. M., Marshall, J., & Heimbach, P. (2004). Overview of the formulation and numerics of the MIT GCM. http://gfdl.noaa.gov/∼aja/papers/ECMWF–2004-Adcroft.pdf

Boyer, T., Domingues, C. M., Good, S. A., Johnson, G. C., Lyman, J. M., Ishii, M.,... Bindoff, N. L. (2016). Sensitivity of global upper-ocean heat content estimates to mapping methods, xbt bias corrections, and baseline climatologies. Journal of Climate, 29(13), 4817-4842. doi:10.1175/JCLI-D-15-0801.1

Bryden, H. L., & Imawaki, S. (2001). Ocean heat transport in, Ocean Circulation and Climate (pp. 455-474): Academic Press, San Diego.

Buckley, M. W., Ponte, R. M., Forget, G., & Heimbach, P. (2014). Low-frequency SST and upper-ocean heat content variability in the North Atlantic. Journal of Climate, 27(13), 4996-5018.

Buckley, M. W., Ponte, R. M., Forget, G., & Heimbach, P. (2015). Determining the origins of advective heat transport convergence variability in the North Atlantic. Journal of Climate, 28(10), 3943-3956.

Chaudhuri, A. H., Ponte, R. M., & Forget, G. (2016). Impact of uncertainties in atmospheric boundary conditions on ocean model solutions. Ocean Modelling, 100, 96-108. doi:10.1016/j.ocemod.2016.02.003

Chaudhuri, A. H., Ponte, R. M., & Nguyen, A. T. (2014). A comparison of atmospheric reanalysis products for the arctic ocean and implications for uncertainties in air-sea fluxes. Journal of Climate, 27(14), 5411-5421. doi:10.1175/jcli-d-13-00424.1

Chelton, D. B., & Schlax, M. G. (1996). Global observations of oceanic Rossby waves. Science, 272(5259), 234-238. doi:10.1126/science.272.5259.234

Colin de Verdière, A., & Ollitrault, M. (2016). A direct determination of the world ocean barotropic circulation. Journal of Physical Oceanography, 46(1), 255-273. doi:10.1175/jpo-d-15-0046.1

Dee, D. P., Balmaseda, M., Balsamo, G., Engelen, R., Simmons, A. J., & Thépaut, J. N. (2014). Toward a Consistent Reanalysis of the Climate System. Bulletin of the American Meteorological Society, 95(8), 1235-1248, doi:10.1175/bams-d-13-00043.1

Dee, D. P., Uppala, S. M. Simmons, A. J., Berrisford, P. et al. (2016) The ERA-Interim reanalysis: configuration and performance of the data assimilation system. Quarterly J. of the Royal Met. Society, 137, 553-597.

Donohue, K. A., Tracey, K. L., Watts, D. R., Chidichimo, M. P., & Chereskin, T. K. (2016). Mean Antarctic Circumpolar Current transport measured in Drake Passage. Geophysical Research Letters, 43(22), 11,760-711,767. doi:10.1002/2016gl070319

Durack, P. J., Wijffels, S. E., & Matear, R. J. (2012). Ocean salinities reveal strong global water cycle intensification during 1950 to 2000. Science, 336(6080), 455-458. doi:10.1126/science.1212222

Elipot, S., Lumpkin, R., Perez, R. C., Lilly, J. M., Early, J. J., & Sykulski, A. M. (2016). A global surface drifter data set at hourly resolution. Journal of Geophysical Research: Oceans.

Evans, D. G., Toole, J., Forget, G., Zika, J. D., Naveira-Garabato, A. C., Nurser, A. J.

G., & Yu, L. Recent wind-driven variability in Atlantic water mass distribution and meridional overturning circulation. Journal of Physical Oceanography, doi:10.1175/jpo-d-16-0089.1

Ferrari, R., & Plumb, R. (2003). Residual circulation in the ocean. Paper presented at the Near-Boundary Processes and Their Parameterization: Proc.'Aha Huliko'a Hawaiian Winter Workshop.

Ferreira, D., Marshall, J., & Heimbach, P. (2005). Estimating eddy stresses by fitting dynamics to observations using a residual-mean ocean circulation model and its adjoint. Journal of Physical Oceanography, 35(10), 1891-1910. doi:10.1175/jpo2785.1

Forget, G. (2010). Mapping ocean observations in a dynamical framework: A 2004-06 ocean atlas. Journal of Physical Oceanography, 40(6), 1201-1221. doi:Doi 10.1175/2009jpo4043.1

Forget, G., Campin, J.-M., Heimbach, P., Hill, C., Ponte, R., & Wunsch, C. (2015). ECCO version 4: an integrated framework for non-linear inverse modeling and global ocean state estimation. Geosci. Model Dev., 8, 3071–3104.

Forget, G., Ferreira, D., & Liang, X. (2015). On the observability of turbulent transport rates by Argo: supporting evidence from an inversion experiment. Ocean Science, 11(5), 839.

Forget, G., & Ponte, R. M. (2015). The partition of regional sea level variability. Progress in Oceanography, 137, 173-195. doi:10.1016/j.pocean.2015.06.002

Forget, G. & Wunsch, C. (2007). Estimated global hydrographic variability. Journal of Physical Oceanography 37, 1997-2008.

Fu, L. L., & Haines, B. J. (2013). The challenges in long-term altimetry calibration for addressing the problem of global sea level change. Advances in Space Research, 51(8), 1284-1300. doi:10.1016/j.asr.2012.06.005

Fuglister, F. C. (1960). Atlantic Ocean Atlas of Temperature and Salinity Profiles and Data from the International Geophysical Year of 1957-1958. Woods Hole Oceanographic Institution.

Fukumori, I., Wang, O., Fenty, I., Forget, G., Heimbach, P.,Ponte, R. (2017) ECCO Version 4 Release 3. Unpublished document. See http://ECCO-group.com

Gebbie, G., Heimbach, P., Wunsch, C. (2006). Strategies for nested and eddy-permitting state estimation. Journal of Geophysical Research-Oceans, 111(C10), Artn C10073. doi 10.1029/2005jc003094

Gent, P. R. & McWilliams, J. C. (1990). Isopycnal mixing in ocean circulation models. Journal of Physical Oceanography, 20, 150-155.

Gill, A. E., & Niiler, P. P. (1973). The theory of the seasonal variability in the ocean. Deep-Sea Res., 20, 141-177.

Gouretski, V. V.,. Koltermann, K. P. (2004). WOCE Global Hydrographic Climatology. Berichte des Bundesamtes für Seeschifffahrt und Hydrographie Nr. 35/2004, Hamburg and Rostock, 50pp.

Griffies, S. M. Danabasoglu, G., Durack, P. J., Adcroft, A. J., et al. (2016). OMIP contribution to CMIP6: Experimental and diagnostic protocol for the physical component of the Ocean Model Intercomparison Project. Geoscientific Model Development, 9, 3231-3296.

Häkkinen, S., Rhines, P. B., & Worthen, D. L. (2013). Northern North Atlantic sea surface height and ocean heat content variability. Journal of Geophysical Research: Oceans, 118(7), 3670-3678. doi:10.1002/jgrc.20268

Hayes, S. P., Mangum, L. J., Picaut, J., Sumi, A., & Takeuchi, K. (1991). TOGA-TAO - a moored array for real-time measurements in the tropical pacific-ocean. Bulletin of the American Meteorological Society, 72(3), 339-347. doi:10.1175/1520-0477(1991)072<0339:ttamaf>2.0.co;2

Ishii, M. Shouji, A., Sugimoto, S., Matsumoto, T. (2005). Objective analyses of sea-surface temperature and marine meteorological variables for the 20th Century using ICOADS and the Kobe Collection. Int'l., J. of Climatology, 25, 865-879.

Kara, A. B., Rochford, P. A., & Hurlburt, H. E. (2003). Mixed layer depth variability over the global ocean. J. Geophys. Res., 108(C3), 3079. doi:10.1029/2000jc000736

Kennedy, J. J., Rayner, N. A., Smith, R. O., Parker, D. E., & Saunby, M. (2011). Reassessing biases and other uncertainties in sea surface temperature observations measured in situ since 1850: 2. Biases and homogenization. Journal of Geophysical Research-Atmospheres, 116. doi:D1410410.1029/2010jd015220

Knudsen, P., & Bingham, R., Andersen, O., Rio, M. H. (2011). A global mean dynamic topography and ocean circulation estimation using a preliminary GOCE gravity model. Journal of Geodesy, 85(11), 861-879. doi:10.1007/s00190-011-0485-8

Koltermann, K. P., Gouretski, V. V., & Jancke, K. (Eds.). (2011). Hydrographic Atlas of the World Ocean Circulation Experiment (WOCE). Volume 3: Atlantic Ocean International WOCE Project Office, Southampton, UK, ISBN 090417557X.

Levitus, S. (1982). Climatological Atlas of the World Ocean. NOAA Professional Paper 13

Liang, X., Piecuch, C. G., Ponte, R. M., Forget, G., Wunsch, C., & Heimbach, P. (2017). Change of the global ocean vertical heat transport over 1993-2010. Submitted for publication.

Liang, X., Wunsch, C., Heimbach, P., & Forget, G. (2015). Vertical redistribution of oceanic heat content. J. Clim., 28, 3821-3833.

Liang, X. F., & Yu, L. (2016). Variations of the global net air-sea heat flux during the "hiatus" period (2001-10). Journal of Climate, 29(10), 3647-3660. doi:10.1175/jcli-d-15-0626.1

Marshall, J., A. Adcroft, C. Hill, L. Perelman, & Heisey, C. (1997). A finite-volume, incompressible Navier Stokes model for studies of the ocean on parallel computers. J. Geophys. Res., 102, 5753-5766.

Maximenko, N., Niiler, P., Rio, M. H., Melnichenko, O., Centurioni, L., Chambers, D.,...

Galperin, B. (2009). Mean dynamic topography of the ocean derived from satellite and drifting buoy data using three different techniques. Journal of Atmospheric and Oceanic Technology, 26(9), 1910-1919. doi:10.1175/2009jtecho672.1

Mazloff, M. R., & Heimbach, P., Wunsch, C. (2010). An eddy-permitting Southern Ocean state estimate. Journal of Physical Oceanography, 40(5), 880-899. doi:Doi 10.1175/2009jpo4236.1

Meredith, M. P., Woodworth, P. L., Chereskin, T. K., Marshall D. P. et al. (2011). Sustained monitoring of the Southern Ocean at Drake Passage: Past achievements and future priorities. Reviews of Geophysics, 49(4), http://doi.org.10.1029/2010RG000348.

Ollitrault, M., & Verdière, A. C. d. (2014). The ocean general circulation near 1000-m depth. Journal of Physical Oceanography, 44(1), 384-409. doi:10.1175/jpo-d-13-030.1

Pavlis, N. K., Holmes, S. A., Kenyon, S. C., & Factor, J. K. (2012). The development and evaluation of the Earth Gravitational Model 2008 (EGM2008). Journal of Geophysical Research-Solid Earth, 117. doi:B04406 10.1029/2011jb008916

Piecuch, C. G., Heimbach, P. Ponte R. M. and Forget, G. L. (2015) Sensitivity of contemporary sea level trends in a global ocean state estimate to effects of geothermal fluxes. Ocean Modelling, 96, 214-220.

Piecuch, C. G., & Ponte, R. M. (2012). Importance of circulation changes to Atlantic heat storage rates on seasonal and interannual time scales. Journal of Climate, 25(1), 350-362. doi:10.1175/jcli-d-11-00123.1

Pillar, H. R., Heimbach, P., Johnson, H. L., & Marshall, D. P. (2016). Dynamical attribution of recent variability in atlantic overturning. Journal of Climate, 29(9), 3339-3352. doi:10.1175/jcli-d-15-0727.1

Ponte, R. M., C. Wunsch, & Stammer, D. (2007). Spatial mapping of time-variable errors in TOPEX/POSEIDON and Jason-1 seasurface height mesurements. J. Atm. Oc. Tech„ 24, 1078-1085.

Purkey, S. G., & Johnson, G. C. (2010). Warming of global abyssal and deep southern ocean waters between the 1990s and 2000s: contributions to global heat and sea level rise budgets. Journal of Climate, 23(23), 6336-6351. doi:10.1175/2010jcli3682.1

Quinn, K. J., & Ponte, R. M. (2008). Estimating weights for the use of time-dependent gravity recovery and climate experiment data in constraining ocean models. Journal of Geophysical Research-Oceans, 113(C12). doi:C12013 10.1029/2008jc004903

Rio, M. H., & Hernandez, F. (2004). A mean dynamic topography computed over the world ocean from altimetry, in situ measurements, and a geoid model. Journal of Geophysical Research-Oceans, 109(C12). doi:C12032

10.1029/2003jc002226

Roquet, F., Wunsch, C., Forget, G., Heimbach, P., Guinet, C., Reverdin, G.,... Fedak, M. A. (2013). Estimates of the Southern Ocean general circulation improved by animal-borne instruments. Geophysical Research Letters, 40(23), 6176-6180. doi:10.1002/2013gl058304

Roquet, F., Wunsch, C., Madec, G. (2011). On the patterns of wind-power input to the ocean circulation. J. of Physical Oceangraphy, 41, 2328-2342.

Schlitzer, R. (2017). Ocean Data View, odv.awi.de.

Speer, K., & Forget, G. (2013). Global distribution and formation of mode waters. Ocean Circulation and Climate: a 21st Century Perspective, Ocean Circulation and Climate: a 21st Century Perspective,

pp. 211–226, doi:210.1016/B1978-1010-1012-391851- 391852.300009-X

Stammer, D., Balmaseda, M., Heimbach, P., Köhl, A., & Weaver, A. (2016). Ocean data assimilation in support of climate applications: status and perspectives. Annual Review of Marine Science, 8(1), 491-518. doi:10.1146/annurev-marine-122414-034113

Stammer, D., Ueyoshi, K., Kohl, A., Large, W. G., Josey, S. A., & Wunsch, C. (2004). Estimating air-sea fluxes of heat, freshwater, and momentum through global ocean data assimilation. Journal of Geophysical Research-Oceans, 109(C5). doi:C05023 10.1029/2003jc002082

Stammer, D., Wunsch, C., Giering, R., Eckert, C., Heimbach, P., Marotzke, J.,... Marshall, J. (2002). Global ocean circulation during 1992-1997, estimated from ocean observations and a general circulation model. Journal of Geophysical Research-Oceans, 107(C9), Artn 3118, doi 10.1029/2001jc000888

Stommel, H., & Arons, A. B. (1960). On the abyssal circulation of the world ocean-I. Stationary planetary flow patterns on a sphere. Deep-Sea Res., 6, 140-154.

Talley, L. D., Feely, R. A., Sloyan, B. M., Wanninkhof, R., Baringer, M. O., Bullister, J. L.,... Zhang, J. Z. (2016). Changes in ocean heat, carbon content, and ventilation: a review of the first decade of GO-ship Global Repeat Hydrography. In C. A. Carlson & S. J. Giovannoni (Eds.), Annual Review of Marine Science, 8, 185-215

Thyng, K. M., Greene, C. A., Hetland, R. D., Zimmerle, H. M., DiMarco, S. F. (2016). True colors of oceanography. Guidelines for effective and accurate colormap selectioni. Oceanography, 29(3), 9-13

Vinogradov, S. V., Ponte, R. M., Heimbach, P., & Wunsch, C. (2008). The mean seasonal cycle in sea level estimated from a data-constrained general circulation model. Journal of Geophysical Research-Oceans, 113(C3). doi:C03032

10.1029/2007jc004496

Vinogradova, N. T., & Ponte, R. M. (2016). In search for fingerprints of the recent intensification of the ocean water cycle. J. Clim., in press.

Vinogradova, N. T., Ponte, R. M., Fukumori, I., & Wang, O. (2014). Estimating satellite salinity errors for assimilation of Aquarius and SMOS data into climate models. Journal of Geophysical Research-Oceans, 119(8), 4732-4744, doi:10.1002/2014jc009906

Wunsch, C. (2011). The decadal mean ocean circulation and Sverdrup balance. J. Mar. Res., 69, 417-434.

Wunsch, C. (2015). Modern Observational Physical Oceanography: Princeton Un. Press.

Wunsch, C. (2016). Global Ocean Integrals and Means, with Trend Implications. In C. A. Carlson & S. J. Giovannoni (Eds.), Annual Review of Marine Science, Vol 8 (Vol. 8, pp. 1-+).

Wunsch, C., & Heimbach, P. (2013). Dynamically and kinematically consistent global ocean circulation state estimates with land and sea ice. In J. C. G. Siedler, W. J. Gould, S. M. Griffies, Eds. (Ed.), Ocean Circulation and Climate, 2nd Edition (pp. 553-579): Elsevier.

Wunsch, C., & Heimbach, P. (2014). Bidecadal thermal changes in the abyssal ocean and the observational challenge. J. Phys. Oc., 44, 2013-2030.

Young, W. R. (2012). An exact thickness-weighted average formulation of the Boussinesq equations. Journal of Physical Oceanography, 42(5), 692-707. doi:10.1175/jpo-d-11-0102.1

Zhai, X. M., & Johnson, H. L., Marshall, D. P., Wunsch, C. (2012). On the wind power input to the ocean general circulation. Journal of Physical Oceanography, 42(8), 1357-1365. doi:10.1175/jpo-d-12-09.1